Montanuniversität Leoben

Dissertation

Bulk metallic glass composites fabricated via high pressure torsion

Dipl.-Ing. Lisa Krämer

Leoben, May 2018

Affidavit

I declare in lieu of oath, that I wrote this thesis and performed the associated research myself, using only literature cited in this volume.

Date	Lisa Krämer

Danke!

Bei meinem Betreuer Reinhard Pippan möchte ich mich bedanken, dass er mir die Möglichkeit gegeben hat mich persönlich und fachlich weiter zu entwickeln. Die Freiheit zu haben eigene Ideen auszuprobieren, aber zu wissen, dass stets die Türe offen steht um Hilfe zu bekommen, möchte ich nicht missen.

I want to say thank you to Prof. Raj, who invited me to Boulder and gave me the possibility to dip into another research field and lab.

Un grand merci à Yannick Champion, qui a effectivement contributé à cette thèse en nous fournissant les poudres amorphes. En plus je le remercie d'avoir toujours trouvé le temps pour des discussions très productives.

Ohne die Hilfe unzähliger Hände am ESI wäre meine Arbeit nicht so schön, aber auch die Arbeitszeit nicht so interessant und nett gewesen. Ich möchte mich bei der Nanoindentationsmeisterin Verena einerseits für die schönen Ergebnisse, aber besonders für ihren Einsatz und ihre Motivation bedanken. Alexander möchte ich für die Berechnung unzähliger c-Werte danken. Danke auch an das Mikromechanik/FIB Team – Reinhard, Ruth, Markus und Marlene –, die mich in die Geheimnisse des Pillarschneidens einwies und unzählige letzte Pillars für mich drückte. Besonderen Dank dabei an Marlene und Markus. Vielen Dank an Karoline und Christoph, die mich mit TEM-Untersuchungen regelmäßig begeisterten und viel dunkle Stunden im Keller mit mir verbrachten. Danke Silke und Gabi für die Hilfe bei der Probenpräparation und Danke an Franz und Robin für die Nachbearbeitung unzähliger HPT-Stempel. Doris, Daniela und Sabine möchte ich vielen Dank für die Unterstützung bei organisatorischen Angelegenheiten sagen. Und schließlich möchte ich mich bei meinen Kollegen für die vielen fachlichen Diskussionen und ihre Hilfe bedanken - insbesondere bei Daniel, Anton, Karoline, Oliver, Markus, Verena, Christoph, Alexander, Timo, Alice, Inas, Juraj, Baran, Oleksandr, Stefan, Andrea, Barbara, Benjamin und Katharina.

Ohne die neuen und alten Freunde, die mich motivierten, ablenkten oder einfach im richtigen Moment ein offenes Ohr für mich hatten, wären die letzten Jahre nicht so im Flug vergangen. Besonderen Dank dabei an meine jahrelange Mitbewohnerin Katharina, die mir auch die vielen abgesagten Abendessen verziehen hat.

Große Unterstützung und Rückhalt hat mir stets meine Familie gegeben, die sich immer über Erfolge mit freuten und mir bei Problemen das Gefühl gaben, dass ich es schon schaffen würde. Ein riesiges Danke an meine Mama Andrea und meine Geschwister, Lena und Sebastian, die auch kurzfristig als Lektoren auftraten, sowie meinem Papa Olaf, der nicht zuletzt immer für einen inspirierenden kulinarischen Rahmen sorgt. Danke Clemens, dass du mit mir gemeinsam auch das Schöne in stressigen Zeiten findest und für den richtigen Ton in meinem Leben sorgst.

Abstract

For this thesis high pressure torsion (HPT) was used to fabricate bulk metallic glasses (BMGs) and bulk metallic glass composites (BMGCs) starting from powders. The powders (amorphous and crystalline) were mixed by hand and the subsequent HPT-process leads to consolidation of the particles and refinement of the microstructure. Using this technique gives a high flexibility regarding combination of different materials and their ratios. The evolution of the microstructures was investigated by means of scanning electron microscopy (SEM), X-ray diffraction (XRD), hardness measurements and transmission electron microscopy (TEM). BMGs generated from powders via HPT require a certain amount of applied shear strain to enforce welding of the particles, and a dense and homogenous microstructure can be obtained. This required strain depends on the used amorphous powder. The obtained microstructure of the BMGCs is lamellar and the phase spacing can be varied from micrometers to nanometers by increasing the applied shear strain. Very high deformation led to the formation of a saturation microstructure, which contained for most compositions only one amorphous phase generated by mixing of the initial materials. For one composite containing 80 wt% of Cu, a nanocrystalline supersaturated solid solution of Cu with elongated MG-nanolamellae was formed instead.

Mechanical properties were investigated by means of nanoindentation, micropillar compression tests and tensile tests. To determine the onset of plastic deformation, a new method of analysis for strain rate jump tests was developed. Thereby, activation energy and volume can be calculated. The main parameter controlling the onset of shear bands is the testing temperature, while composition, energy state, fabrication method and even the second phase in composites have a minor effect. However, the second phase has a great influence on the propagation of the shear bands, which is shown by micropillar compression tests. The shear bands are affected by the material of the second phase (crystalline or amorphous),

by the structural size of the phases and also by the orientation of the lamellar structure regarding the loading direction.

In conclusion, BMGs and BMGCs were fabricated via HPT and the microstructural evolution was investigated. Changes in deformation behavior were studied and it was shown that the nucleation of shear bands depends mainly on the homologous temperature of the MG, while their propagation can be influenced by adding a second phase.

Kurzfassung

Ziel der vorliegenden Arbeit war die Synthese metallischer Massivgläser (englisch: bulk metallic glass - BMG) und Komposite mit amorphen Phasenanteilen (englisch: bulk metallic glass composite - BMGC) mittels Hochdrucktorsion (englisch: high pressure torsion - HPT). Dafür wurden verschiedene Pulver (kristalline sowie amorphe) per Hand gemischt und anschließend direkt im HPT Werkzeug konsolidiert. Vorteile dieser Methode sind ihre hohe Flexibilität, die es erlaubt, die unterschiedlichsten Materialien in einem beliebigen Verhältnis zu mischen, und die Möglichkeit die aufgebrachte Dehnung und damit die Mikrostruktur einfach über die Anzahl der aufgebrachten Umdrehungen zu regulieren. Die mikrostrukturelle Entwicklung wurde mittels Rasterelektronenmikroskopie, Röntgenbeugung, Härtemessung und Transmissionselektronenmikroskopie untersucht. Für metallische Massivgläser ist ein kritischer Verformungsgrad notwendig, um die amorphen Pulverpartikel zu verschweißen und so ein dichtes Festmaterial zu erzeugen, wobei die notwendige Verformung auch von der verwendeten Legierung abhängt. Bei den Kompositen verursacht die Scherverformung des HPT-Prozesses eine lamellare Struktur, die mit ansteigender Verformung immer mehr verfeinert. Dadurch können Lamellendicken im Bereich von Mikro- bis Nanometer eingestellt werden. Sehr hohe Verformung führt zur Bildung einer Sättigungsstruktur, die bei den meisten untersuchten Kompositen aus einer einzigen amorphen Phase besteht. Diese wird durch Mischung der beiden Anfangsphasen gebildet. Die einzige Ausnahme war ein Komposit mit 80 m% Cu, hierbei bildete sich ein nanokristalliner übersättigter Mischkristall, in dem längliche amorphe Bänder eingebettet sind.

Die mechanischen Eigenschaften wurden mit Nanoindentation, Mikropillardruckversuchen und Zugversuchen ermittelt. Das Einsetzen plastischer Verformung wurde anhand des Aktivierungsvolumens und der Aktivierungsenergie charakterisiert. Dafür wurde eine neue Analysemethode von Dehnratenwechselversuchen

bei Nanoindentierung entwickelt, weil herkömmliche Methoden nur für kristalline Materialien gültig sind. Der Haupteinfluss auf die Scherbandbildung ist die Versuchstemperatur, während Herstellungsverfahren, Zusammensetzung, energetischer Zustand und selbst eine zweite Phase kaum Auswirkungen haben. Im Gegensatz dazu zeigen die Druckversuchen, dass eine zweite Phase die Scherbandausbreitung stark beeinflusst. Die Art des Materials, sowie seine Phasenabmessungen und Orientierung spielen nun entscheidende Rollen.

Im Zuge dieser Arbeit wurden die Möglichkeiten der Herstellung von metallischen Massivgläsern und deren Kompositen mittels HPT untersucht und die mikrostrukturelle Entwicklung analysiert. Untersuchungen der mechanischen Eigenschaften zeigten, dass die Scherbandentstehung hauptsächlich von der homologen Temperatur abhängt, während die Scherbandausbreitung durch eine zweite Phase beeinflusst werden kann.

Contents

List of Abbreviations

N	numbers of turns during the HPT-process
T_g	glass transition temperature
ΔG	activation energy
δ	reflection angle
$\dot{\gamma}$	strain rate
γ	shear strain
γ_0	shear strain
λ	wavelength
τ	shear stress
c	constraint factor
k	Boltzmann's constant
k_a	jump frequency
n	concentration of flow defects
q	scattering vector
r	radius
t	thickness of the HPT disk
t_{cr}	critical layer thickness
v_0	activation volume
ASMEC	advanced surface mechanics GmbH
at%	atomic percentage
BMG	bulk metallic glass
BMGC	bulk metallic glass composite
DSC	Differential Scanning Calorimetry
EDX	energy dispersive X-ray spectroscopy
Fe-MG	Fe-based metallic glass
FIB	focused ion beam
h	indentation depth
HNO_3	nitric acid
HPT	high pressure torsion

HV	Vicker's hardness
m%	Massenprozent
MG	metallic glass
nc	nanocrystalline
Ni-MG	Ni-based metallic glass
OPS	oxide polishing suspension
SB	shear band
SEM	scanning electron microscope
SPD	severe plastic deformation
TEM	transmission electron microscopy
ufg	ultra fine grained
vol%	volume percentage
wt%	weigh percentage
XRD	X-ray diffraction
Zr-MG	Zr-based metallic glass

1. Introduction

A main attribute of modern society is its highly specialized usage of materials for different applications. Even animals use a variations of materials found in nature as tools. Chimpanzees were observed to use stones to crack nuts and then switch to wood sticks for extracting the remaining kernel [1]. However, humans are producing and adjusting materials for particular applications instead of just using what can be found.
An important role for materials design plays the inner structure as it equally determines all their properties, for example the mechanical, thermal, magnetic and electrical ones. In 1960, Duwez et al. showed that metal alloys with amorphous structures can be produced by using very high cooling rates [2]. Amorphous alloys have in contrary to crystals only a short-range and no long-range order. The first metallic glass (MG) composed of Si and Au could only be produced with small geometric dimensions and was not stable at room temperature, because it crystallized. Over the last decades, stable compositions, which could also be casted with larger dimensions, have been developed with different base elements such as Pd, Zr, Fe, Mg, Cu and rare earth elements. Diameters up to 72 mm could be achieved and additional production routes for amorphization were found such as mechanical alloying, ion beam mixing, inverse melting, diffusion induced amorphization and hydrogen absorption [3, 4]. A solution to overcome the dimension limitations during casting is to use an additional technique such as severe plastic deformation (SPD), powder metallurgy or extrusion [5–9]. For the first two methods, it is possible to start with amorphous powders, which are easier to produce and are then consolidated by mechanical deformation or sintering. Among different SPD methods, high-pressure torsion (HPT) offers some advantages which makes it interesting for producing bulk metallic glasses (BMGs). The high, nearly hydrostatic pressure allows to deform even brittle materials and the applied strain is easily controlled by changing the number of turns. The number of turns is only limited by the available time of the HPT and

the patience of the PhD student. One sample with a strain of $\gamma = 500,000,000$ could have been produced during this thesis with our standard deformation conditions of a sole usage of the HPT, if no thinning of the sample and no wear of the anvils are assumed. Since at large strains a saturation in the structure evolution takes pace, the applied turns were limited to 500 turns. Interesting effects such as mixing of immiscible phases, the deformation-induced phase formation and amorphization of crystalline materials can be studied in detail [10–14]. MGs show a low ductility as the main deformation mechanism below the glass transition temperature (T_g) are shear bands (SBs), in which nearly the whole deformation is concentrated. This means that MGs show nearly no deformation globally, but very high strains can occur locally in SBs leading normally to failure. An idea to increase the ductility is to hinder the propagation of shear bands to facilitate initiation of additional shear bands and to lengthen their extension. This can be accomplished by introducing phase boundaries as in composites or by increasing the number of possible initiation sites via an inhomogeneous structure. One possible way for the latter is rejuvenation, which is seen as counterpart of annealing in metallic glasses. This rearrangement of atoms causes higher free volumes or higher energetic ordering and leads to local softening [15]. A common way for rejuvenation is thermal cycling, but also HPT can be used and for some MG compositions, a decrease in hardness and increase in ductility are observed [16–19].

The fundamental idea of this thesis was to investigate the capability to produce BMGs starting from different amorphous powders using HPT and to investigate the influence of the applied high strains on the microstructure. The next logical step was to blend different powders and, thereby fabricate bulk metallic glass composites (BMGCs) containing an amorphous and crystalline phase or even two different amorphous phases.
The evolution of the microstructure was investigated as a function of HPT-turns and different powders (three amorphous and five crystalline) were combined. The combination of different materials and varying the ratio of the phases influences the microstructural evolution. Besides the fabrication of BMGs and BMGCs, also changes in mechanical properties were investigated. Nanoindentation strain rate jump tests at ambient and elevated temperatures were used to determine activation volumes and activation energies. Due to the lack of analysis methods for non-crystalline materials, a novel evaluation procedure for amorphous ma-

terials was developed. Additional in-situ microcompression tests were used to correlate the properties of the second phase including its structure (amorphous or crystalline), its thickness, and its orientation to the mechanical properties of BMGCs.

2. Technical comments on high pressure torsion

The used HPT and the schematic for the quasi-hydrostatic setup can be found in Figure 2.1 a and b. Anvils with cylindrical cavities with a diameter of 6 mm and a depth of 0.2 mm are used. To enhance the stability of the HPT process, the anvils were flattened around the cavities for 1 mm. Excess material will fill the volume between the flatten areas and experiences high amounts of frictions. This leads to a back stress and thereby the nearly hydrostatic pressure in the disk is obtained. For powder consolidation, a 3 mm high Cu-ring with a diameter slightly larger than 6 mm is glued on one anvil in which the powder is filled. Thereby, the required volume of material is ensured for the subsequent deformation between the anvils. The ring is removed after applying 4 GPa and rotation by about10°. Normally, the further HPT process is conducted with 8 GPa and a rotation speed of 0.6 min^{-1}. The applied strain γ is varied by changing the number of turns, which can be calculated by

$$\gamma = \frac{2\pi N r}{t} \tag{2.1}$$

with the radius, r, number of turns, N, and the sample thickness, t. As HPT is a well-used process, general information and a discussion of important parameters can be found elsewhere [20]. Here only some common problems which were encountered during HPT-process of consolidating and deforming powders are described. Possibilities to prevent or at least diminish these are pointed out.

One problem arises from the fact that amorphous powders and not bulk materials were used. Therefore, impurities, crystallization of the powder particles and oxidation cannot be avoided. In Figure 2.2, examples for contamination of the undeformed powder (a) and in a deformed HPT disk (b) are shown. Impurities harder than the matrix material tend to swim undeformed until break down

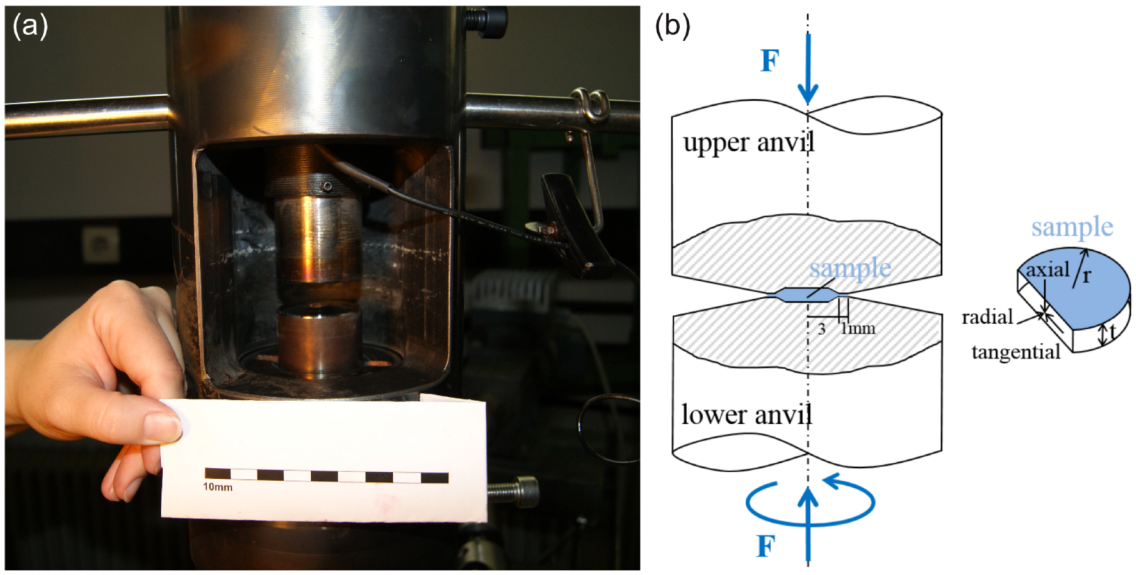

Figure 2.1.: (a) Photo of the used HPT set-up and (b) the schematic of the anvils and a specimen.

and mixing occurs. Smaller and softer particles, as well as probably oxide layers covering the powder, are refined much earlier and will be dissolved partly. Contamination of the received powder cannot be avoided, but using regularly cleaned tools for handling is necessary for minimizing this problem.
Partly crystallized powder particles can be found in the deformed HPT disks at small deformation. High amounts of applied shear strain lead to dissolving of the small crystals and again fully amorphous samples are obtained. As crystallization is a problem of the initial powder, it is unclear if it occurs during powder fabrication or processing. In the latter case, using more stable compositions or shorter and cooler storage could probably prevent this problem.

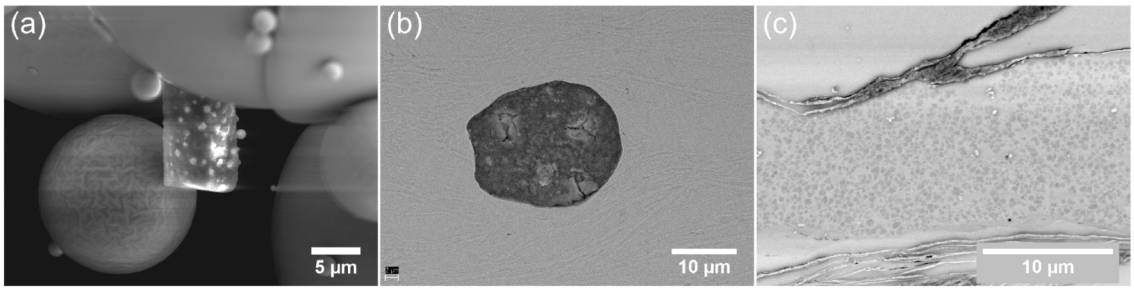

Figure 2.2.: SEM micrographs of impurities in (a) the undeformed powder and (b) in a deformed sample. Rarely, crystallized particles can be found (c). It is unclear if they are formed during the initial powder fabrication or if crystallization occurs due to long storage time and temperature effects.

During the HPT process several aspects for successful deformation must be regarded. One of the most serious one is the possibility of explosion during the HPT-process. This phenomenon occurs occasionally for other materials such as Mg and during deformation of a variety of powders. It happens frequently for most of the usual compositions of metallic glasses and explosions are not limited to deforming powders, but are also common during HPT-deformation of BMGs. The real cause of this effect is not fully understood, but the explosions during the deformation process of powders occur more frequently during humid and warm days. A heat treatment at 100 °C for 30 min to reduce the water content in the powder reduces the probability of explosions. Mostly, only one explosion occurs per HPT-process and sample, but it can happen during loading, rotating or unloading. The number of explosions increases drastically for some compositions and elevated temperatures can worsen this problem. Most likely, only the outer, thinner part of the sample explodes as the microstructure is not affect and no crystallization occurs. Therefore, samples which showed an explosion during HPT could still be used without compromising the results. By changing the composition of the MG, the colors of the explosions can be varied. In Figure 2.3, an explosion of a Zr-based MG is shown. The explosions cannot be fully prevented, but deforming dry powders on cool, dry days decreases their number. Encapsulating the HPT with acrylic glass and using protective gear such as laboratory coat, safety glasses and ear protections makes it possible to work safely nonetheless.

Well-machined anvils are a basic requirement for a successful HPT-process. A larger area surrounding the cavities is flattened compared to anvils used for ductile materials, because this increases the stability of the material. This material is essential for the nearly hydrostatic pressure and prevents thinning of the specimens. Excessive thinning causes contact of the two anvils, which can be heard during the HPT-process as crackling and causes large wear of the anvils and unsuccessful deformation of the samples.
Additionally, it is important to have no misalignment of the anvils, which leads in the best case to an undefined distribution of deformation in the sample and in the worst case to cracking of the specimens. In Figure 2.4, the misalignment of the anvils led to a shift of the upper part against the lower part of the HPT disk. This problem can be minimized by checking the guidance of the two anvils regularly. Partial deformation of the sample can also be caused by slipping of the sample due to a lack of friction between sample and anvils. Therefore, the

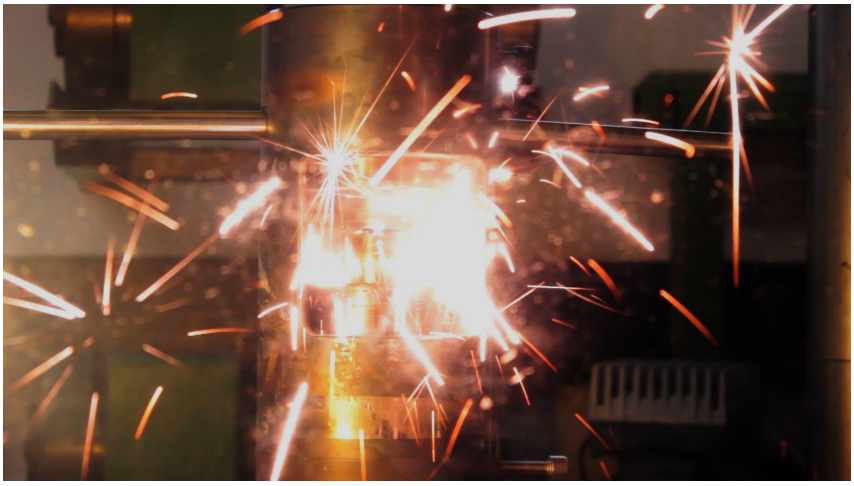

Figure 2.3.: Photo of an explosion during the HPT process. No changes of the microstructure are detectable compared to specimens which did not explode. Drying the used powders prior to deformation could reduce the probability of explosions.

cavities are sandblasted before each sample.

One problem occurring only for HPT of powders stems from the use of a Cu-ring to ensure sufficient material for the deformation. If the Cu-ring has a too small diameter or is not removed soon enough, it can be sucked into the specimen and contaminates the specimen. An example is shown in Figure 2.4 a, where Cu (red) can be seen on both edges of the specimen. On the right side, indicated by an arrow, the Cu reaches nearly 1 mm in the direction of the center and a crack proceeds along it. Therefore, it is important to use Cu-rings with diameter larger than the final diameter of the sample and to remove the remaining Cu after only rotating by a few degrees.

Even if all the above recommendations are followed and a nice looking specimen was extracted from the anvils, it is crucial to check if the deformation is homogenous. In Figure 2.5 a and b, two samples with an inhomogeneous distribution of deformation are compared to a representative cross section of a homogeneously deformed sample, which was used for further investigations within this thesis (c).

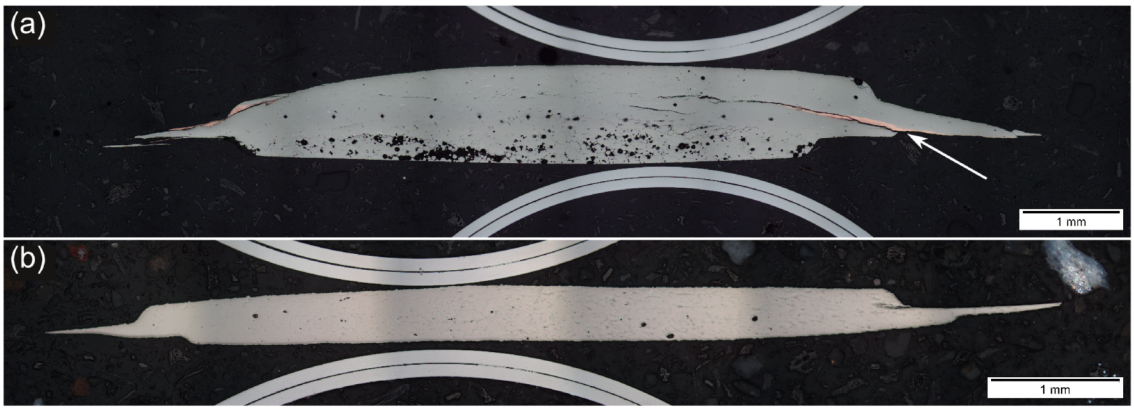

Figure 2.4.: Optical micrographs of the cross section of two HPT-processed samples exhibiting two critical errors hindering successful deformation. The Cu ring was not fully removed after the first consolidation step (a) and thereby, Cu contaminates the sample and acts as crack initiation, which is indicated by an arrow. A misalignment of the two anvils leads to a shift of the upper and lower half sample (b), which causes a undefined distribution of the applied strain and can cause crack formation in brittle specimens.

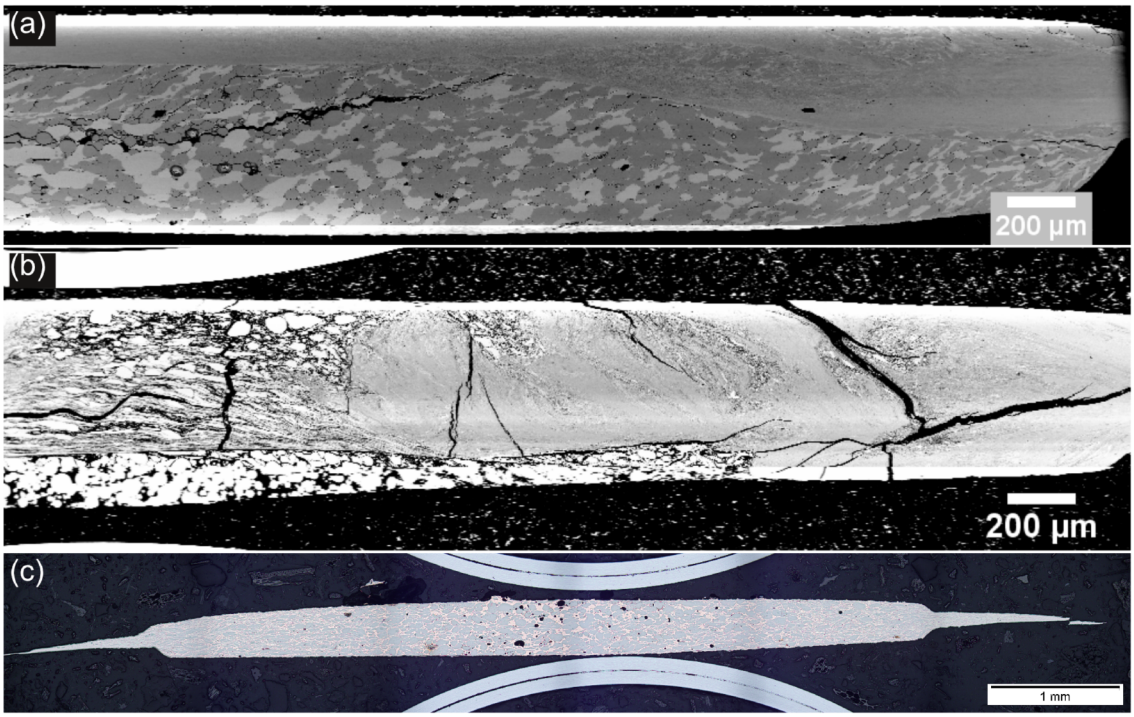

Figure 2.5.: SEM and light micrographs of three HPT-discs. (a) and (b) show samples, which exhibit localized deformation during the HPT-process, whereas in (c) a specimen with homogeneous strain distribution over the sample thickness is shown, which was further investigated within this thesis. Also, the larger refinement at higher radii due to higher applied strains can be observed.

3. Experimental results

Single phased bulk metallic glasses were produced by consolidation and deformation of amorphous powders for this thesis. This technique was used on three different MG powders: a Zr-based ($Zr_{57}Cu_{20}Al_{10}Ni_8Ti_5$), a Ni-based ($Ni_{53}Nb_{20}Ti_{10}Zr_8Co_6Cu_3$) and an Fe-based ($Fe_{50}Co_{35}Nb_8B_4Si_3$) generated via high pressure gas atomization [21] and impulse atomization [22]. Mechanical properties such as hardness differ strongly for these compositions and therefore large differences in the deformation behavior are observed during the HPT process.

Different bulk metallic glass composites were fabricated via HPT using amorphous and crystalline powders as starting materials. Prior to HPT individual powders were mixed to achieve different combinations and fraction of the phases. The main focus was on Zr-MG + crystalline Cu, whereby, chemical composition and applied strain were varied over a large range. The two phases were chosen as model materials, because Zr-MG is one of the most investigated class of MGs and Cu is known for its high ductility. Additional composites as Zr-MG + Cu + Ni, Zr-MG + Al, Ni-MG + Cu, Fe-MG + Fe, and Fe-MG + Co have been fabricated.

In table 3.1, a summary of the fabricated BMGCs is shown and the wt% of the second phase is given. Composites used for further characterization are emphasized. Empty fields mean that these combinations were not investigated in this thesis.

Table 3.1.: The fabricated BMGCs are shown and the compositions are in wt%. The compositions, which were used for further characterization are emphasized.

	Zr-MG	Ni-MG	Fe-MG
Cu	***20, 40, 60, 80***	20, 40	
Al	40	10, 20	
Fe			75
Co			20, 40
Zr-MG		***30, 50***	

3.1. Single phased bulk metallic glasses

HPT is commonly used to refine and investigate the evolution of the microstructure as a function of deformation, but MGs have an amorphous microstructure and therefore exhibit no grains, boundaries or dislocations. Subjecting a homogenous material without internal structure to HPT-deformation seems at first glance pointless, but it is used for two main reasons: Rejuvenation and fabrication from powders. The idea behind rejuvenation of MGs is that not only one single amorphous structure exists, but that the state of the MG can be changed gradually [15]. This can happen by changing the cooling rate during casting or annealing, but also by elastic loading. BMGs subjected to HPT show changes including in their hardness and structure [15–18, 23]. However, other studies indicate that deformation induced changes in the MG are not homogenous distributed, but are concentrated in SBs [24]. Fabrication of BMG specimens can be achieved by mixing and amorphization of crystalline composites [25] or by consolidation and deformation of initial amorphous powders, flakes or sheets [5, 26–29].

3.1.1. Microstructural evolution

Zr-based metallic glass

The powder consolidation depends strongly on the applied strain as the mechanical welding of the powder particles requires high deformation. In Figure 3.1, the cross sections of two Zr-MG samples with different numbers of turns during the HPT-process are shown. In the sample with only three turns (a) most of the particles are deformed, but still many gaps are visible and even removal of individual particles during cutting and polishing occurs frequently. At the edge of this sample, where the applied strain is higher, the welding progresses already further and denser material is observed. Complete densification was observed in the sample with 30 turns at room temperature (b). Sporadic defects can still be found at the cross section, but overall a fully dense and homogenous microstructure can be observed. Additional SEM micrographs of the initial powder (c) and at different strains are added. At lower strains (d), cracks corresponding to the initial powder particles are visible, but at higher strains (e) no defects are visible.

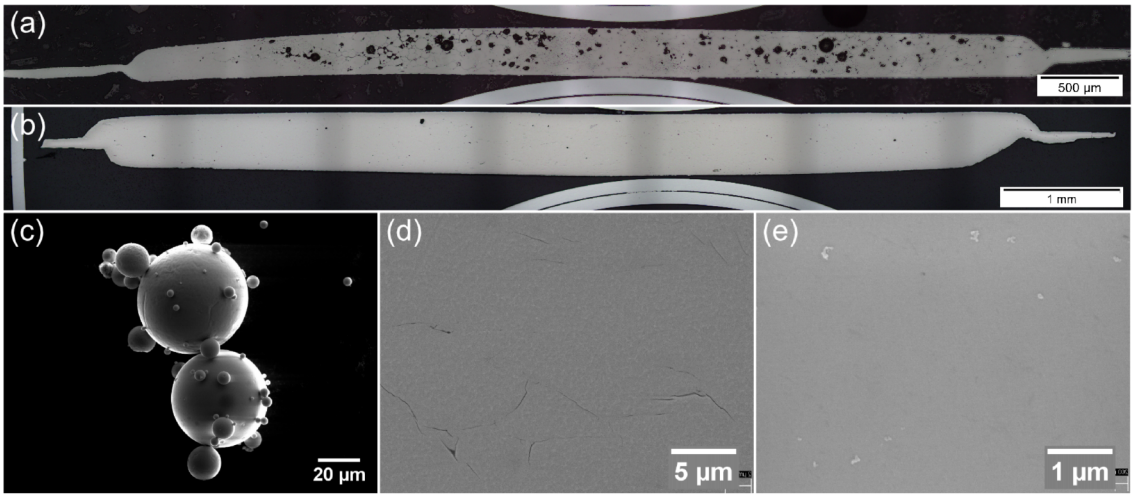

Figure 3.1.: Illustration of the evolution of the microstructure of Zr-MG. Optical micrographs of the cross sections show a lower density for (a) a sample with two turns compared to (b) a sample with 30 turns. SEM micrographs of (c) undeformed powder, (d) partly welded particles at lower strains and (e) a defect free microstructure at higher strains can be seen.

The brighter structure in (d) and oxide polishing suspension (OPS) particles in (e) are caused by insufficient cleaning.

Ni-based metallic glass

Ni-MG has a higher hardness than Zr-MG, but shows the same microstructural evolution leading to fully dense, single phased bulk materials. In Figure 3.2, SEM micrograph of the initial powder (a) and of the cross section are shown. At (b) a shear strain $\gamma \approx 100$, crack-like features can be seen. The distances between

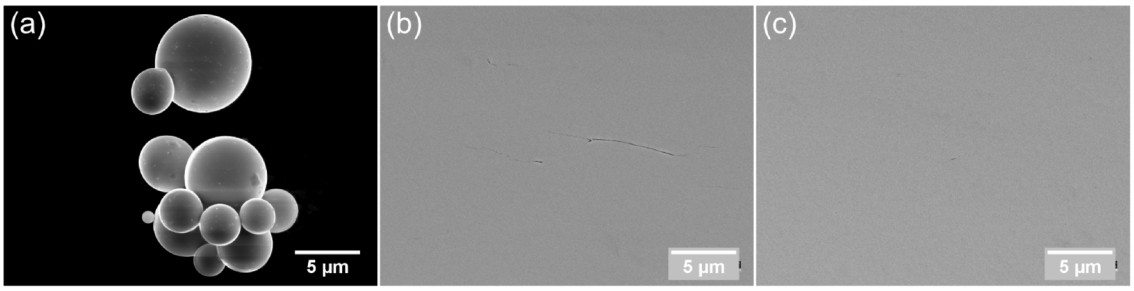

Figure 3.2.: SEM micrographs of the microstructural evolution of Ni-MG. (a) shows the undeformed powder and in (b) the distance between the crack-like feature correlate to initial particle size. Higher applied strains lead to a full welding of the particles and a nice, homogeneous microstructure is obtained (c).

the defects correlates with the diameters of the used powder indicating that the remaining boundaries from the initial particles are still visible as they are not fully welded. By increasing the applied shear strain to $\gamma \approx 760$, a nearly flawless microstructure is obtained (c).

Fe-based metallic glass

The investigated Fe-MG powder particles have an initial hardness of more than 1000 HV and are difficult to consolidate and deform, because the anvils' hardness are 300 HV lower. In addition to the high hardness, the Fe-MG sample and the HPT anvils tend to weld together and therefore, no specimens with high numbers of turns could be produced. In Figure 3.2 (a), a SEM micrograph of the cross section of a Fe-MG sample, which was deformed at room temperature for approximately $\gamma \approx 37$, is shown. Even though the powder particles are deformed and do not have their characteristic round shape anymore, the particles are not welded together and gaps along the initial boundaries can be found over the whole sample. The cross section of a sample deformed for 5 turns at 500 °C is shown in the other two micrographs (b and c). The applied strain at this radius is approximately $\gamma \approx 160$ and this is sufficient to obtain a consolidation of the particles and a promising homogeneous structure. The crack coming from the edge of the specimen is probably induced during the unloading process and does not run along the initial boundaries of the particles. In (c) a micrograph at higher magnification shows a good welding of the Fe-MG particles. Unfortunately, no

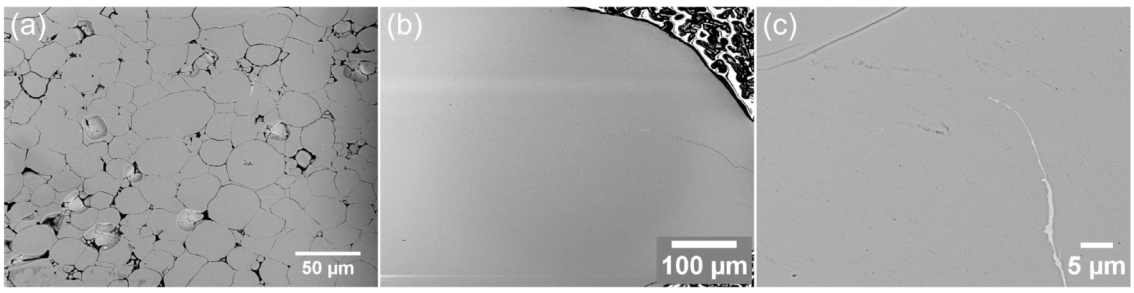

Figure 3.3.: SEM micrographs of Fe-MG. Due to its high hardness and welding of the MG with the steel anvils, no fully dense samples could be fabricated at room temperature at $\gamma \approx 37$ (a). After 5 turns at 500 °C, the applied strain of $\gamma \approx 160$ at the edge of the specimen is high enough to weld the particles together (b). Higher magnification (c) show inhomogeneities as cracks (from unloading initiated at the edge of the specimen), impurities and boundaries, which are not fully welded yet.

fully dense specimens without unloading cracks could be fabricated from the Fe-MG powder.

3.1.2. Evolution of the hardness

A similar trend of powder consolidation controls the evolution of hardness as it is depicted in Figure 3.4 for Zr-MG and Ni-MG. The high scattering and lower hardness values at lower strains are caused by incomplete welding. At higher strains, the scattering reduces and a saturation hardness of 460 HV and 640 HV are obtained for Zr-MG and Ni-MG, respectively. Although, both MGs show a hardness saturation at high strains, Zr-MG initial shows an increase in hardness due to densification and reduction of cracks, whereas, Ni-MG shows a slight decreasing in hardness. In literature other MGs show similar behavior, sometimes even more pronounced, which is explained by rejuvenation [16, 17]. Rejuvenation is commonly seen as a counterpart to annealing and leads to changes in the amorphous structure towards higher energy levels [30]. During plastic deformation, these higher energetic areas will deform first to reduce their energy by shifting the atoms to more favorable positions and thereby, causing a softening of the material. Rejuvenation is not seen for Zr-MG, which was verified via nanoindentation of undeformed powder and for a sample with 30 turns. Both conditions show the same hardness with 6.12 ± 0.33 GPa and 6.11 ± 0.07 GPa for the powder and the deformed specimen, respectively. The evolution of hardness could not be measured for the Fe-MG, because of the lack of consolidation and high amount of cracks in all samples.

3.1.3. Phase analysis via X-ray diffraction

XRD and synchrotron measurements are used for phase investigations to analyze if a fully amorphous microstructure remains during the HPT-process. Figure 3.5 shows diffraction results for (a) Zr-MG, (b) Ni-MG and (c) Fe-MG in the form of intensities as a function of the scattering vector q

$$q = \frac{4\pi \sin \delta}{\lambda}, \tag{3.1}$$

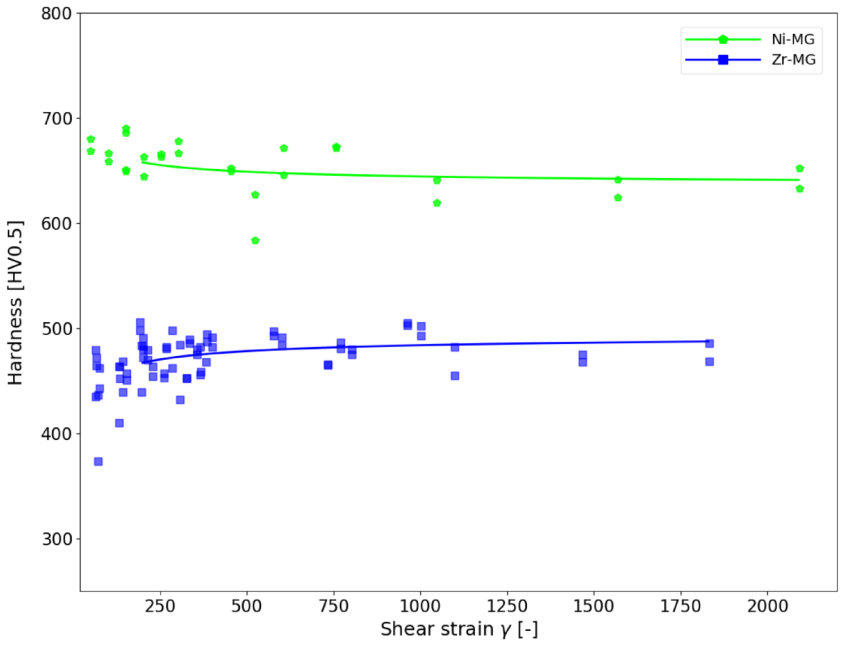

Figure 3.4.: Illustration of the hardness evolution as a function of the applied strain. Both MGs show a reduction in data scatter as the shear strain is increased, because the welding of the particles leads to a densification. Zr-MG has a lower hardness than Ni-MG and the former shows an increase in hardness, whereas lower hardness values are measured at higher strains for the latter. Redrawn from Paper C.

where δ is the reflection angle and λ is the wavelength of the X-rays. This conversion allows plotting data from the synchrotron and lab diffractometer measurement with different wave lengths in one figure. Amorphous materials show commonly broad peaks, whereas the first one at smaller q exhibits higher intensities. Zr-MG shows such amorphous peaks at $q \approx 2.6$ and $q \approx 4.4$ for the two measurements of the undeformed powder and three measurements of samples with 30 turns at room temperature. One of the undeformed powder and one deformed sample show a deviation from the fully amorphous structure. The first peak is of a more angular shape, which is indicated by arrows. Partly crystallization or contamination of the Zr-MG powder could explain this behavior. Comparing the undeformed to the deformed sample, it looks as if the crystalline phase has decreased. This can be explained by amorphization of the crystals due to the high plastic deformation during the HPT-process or a lower fraction of crystalline particles in the beginning. In contrast, other measurements of the same powder show a fully amorphous initial material and also no crystalline peak after deformation. Again, this might be a coincident depending on the contamination of the used powder, or it can be explained by a shorter storage time, which leads

to the conclusion that this Zr-based MG is not stable at room temperature. Ni-MG (b) does not show any crystalline peaks, neither for the undeformed powder nor for the deformed specimens leading to the conclusion that the deformation process does not influence the overall structure of the MG and less impurities are in the used powder. In Figure 3.5 c, two Fe-MG specimens are shown and while after one turn at room temperature the typical broad amorphous peaks are measured, the specimen which was deformed for 5 turns at 500 °C shows partial crystallization leading to a pointed shape of the first peak (indicated with an arrow). The number and size of the crystals may still be small as the intensities are similar to the amorphous peak, but can explain the better deformability at higher temperatures as seen in the SEM micrographs.

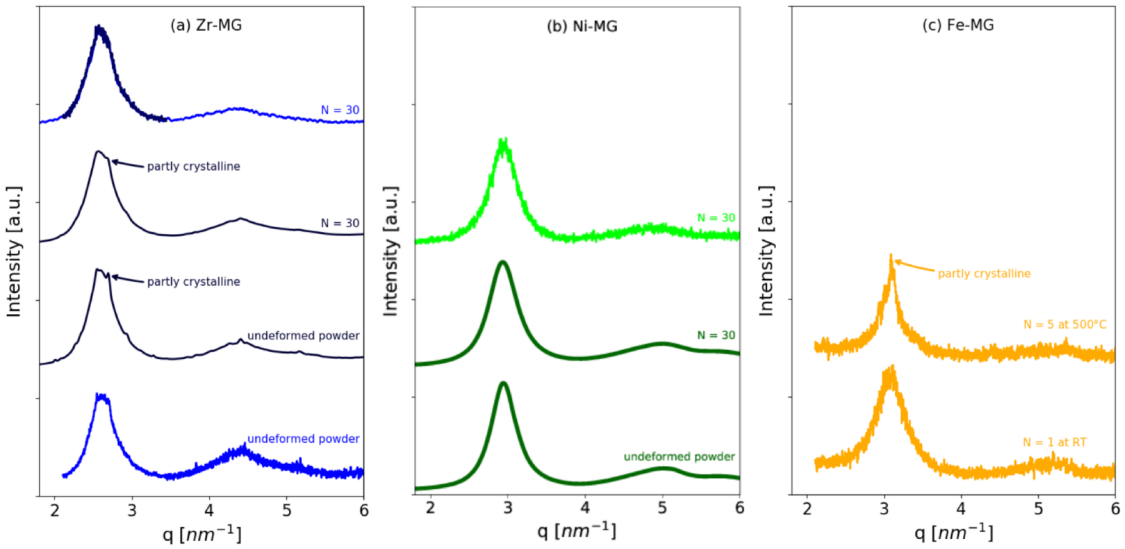

Figure 3.5.: XRD measurements of (a) Zr-MG, (b) Ni-MG and (c) Fe-MG for deformed samples and undeformed powders. No crystallization occurs during the HPT-process at room temperature, but for Zr-MG a crystalline contamination can be seen for the undeformed powder and the deformed specimen measured in the Synchrotron (second and third curve). XRD measurements for Fe-MG deformed at 500 °C shows a partial crystallization.

3.2. Bulk metallic glass composites

BMGs are mainly controlled by their compositions and in smaller parts by their history (annealing and rejuvenation) [17, 23, 30–34], but to effectively adjust their properties often a second phase is added. Different combinations are possible such as amorphous/crystalline, amorphous/quasicrystalline and amorphous/amorphous [35]. Partial crystallization by choosing a lower cooling rate or an additional annealing step at temperatures higher than the crystallization temperature can be used to obtain amorphous/crystalline composites [36–41]. It is also possible to add a second phase in the form of springs, tubes, wires or particles during casting [42–47]. However, both routes often lead to very inhomogeneous microstructures and the formation of a brittle crystalline phase [48, 49]. Adapting powder metallurgy and sintering processes for amorphous composites shows good results with the main problem of achieving full densification of the specimens. Amorphous/amorphous composites can be produced by exploiting chemical demixing in the melt or prior to crystallization caused by a high positive energy of mixing [35]. Another technique to produce a composite containing two MGs is inert gas condensation of two targets with different compositions combined with in-situ compaction to produce bulk specimens [50]. HPT offers the possibility to produce amorphous/crystalline as well as amorphous/amorphous BMGCs. As powders are used as starting material a high flexibility in possible amorphous compositions (dimensions of powders are small compared to conventional casting) and variations of powder mixtures are guaranteed. The high nearly-hydrostatic pressure during the HPT-process enables also the deformation of commonly brittle materials and the microstructure is easily adjustable over a wide range by changing the applied strain.

3.2.1. Amorphous/crystalline composites

Zr-MG and crystalline Cu

Similar to the microstructural evolution of a single phased MG, the microstructure of the composites shows a strong dependence on the applied strain. Additionally, microstructural evolution of these BMGCs is a function of the Cu-content. Both phases have different mechanical properties such as hardness and therefore the

ratio of the amorphous and crystalline powder has a high influence. In Figure 3.6, the obtained microstructure of three composites (Zr-MG 20wt% Cu, Zr-MG 40wt% Cu, and Zr-MG 60wt% Cu) is shown as a function of the applied strain. The two composites with less than 50wt% Cu show a similar evolution: In the beginning, mainly the softer Cu is deformed and acts as a glue between the nearly undeformed Zr-MG particles. As the strain increases, the MG starts to deform more pronouncedly and co-deformation of the two phases is observed leading to a lamellar structure. These lamellae refine mainly in the thickness direction until the microstructure becomes more and more blurry and in the end, only a single phased material is observed in SEM. This can be explained by intermixing of the two phases or a refinement of the two phases below the resolution of the SEM. The major difference between the two compositions is the maximum strain required to obtain the homogenous saturation microstructure. A higher fraction of Cu doubles this value from $\gamma \approx 390$ to $\gamma \approx 850$ for Zr-MG 20wt% Cu and Zr-MG 40wt% Cu, respectively. For Zr-MG 60wt% Cu the microstructural evolution looks similar in the beginning, as Cu sustains most of the deformation at lower strains until a lamellar structure is formed. However, the refinement of the lamellae differs as mainly a shearing-off instead of homogenous thinning is observed. A single phased saturation microstructure is obtained in the end and the required saturation strain increases to about $\gamma \approx 11000$. The Cu content was further increased to 80wt% and the effect on the microstructure can be seen in Figure 3.7. Again a lamellar structure is formed, which breaks down until a saturation microstructure is obtained. In contrast to lower Cu contents, the saturation microstructure consists of a Cu-rich nanocrystalline matrix in which elongated Zr-MG bands with a length of several micrometers are embedded. The applied strain was increased up to $\gamma \approx 18900$ by deforming a sample for 500 turns, but no significant changes can be observed.

The evolution of the microstructure is reflected in the hardness and XRD measurements. The hardness as a function of the applied strain is shown in Figure 3.8, for all four compositions and Zr-MG. The composition with lower contents of Cu (20wt%, 40wt%, and 60wt%) show similar hardness evolutions. At low strains, a strong increase is observed starting well below the hardness of the single phased MG. With increasing strain the slopes decreases and the curves levels off until a hardness higher than the single phased Zr-MG is reached. For Zr-MG 20wt% Cu and Zr-MG 40wt% Cu the saturation is not fully reached yet. The main difference is the required shear strain to reach saturation, which increases with

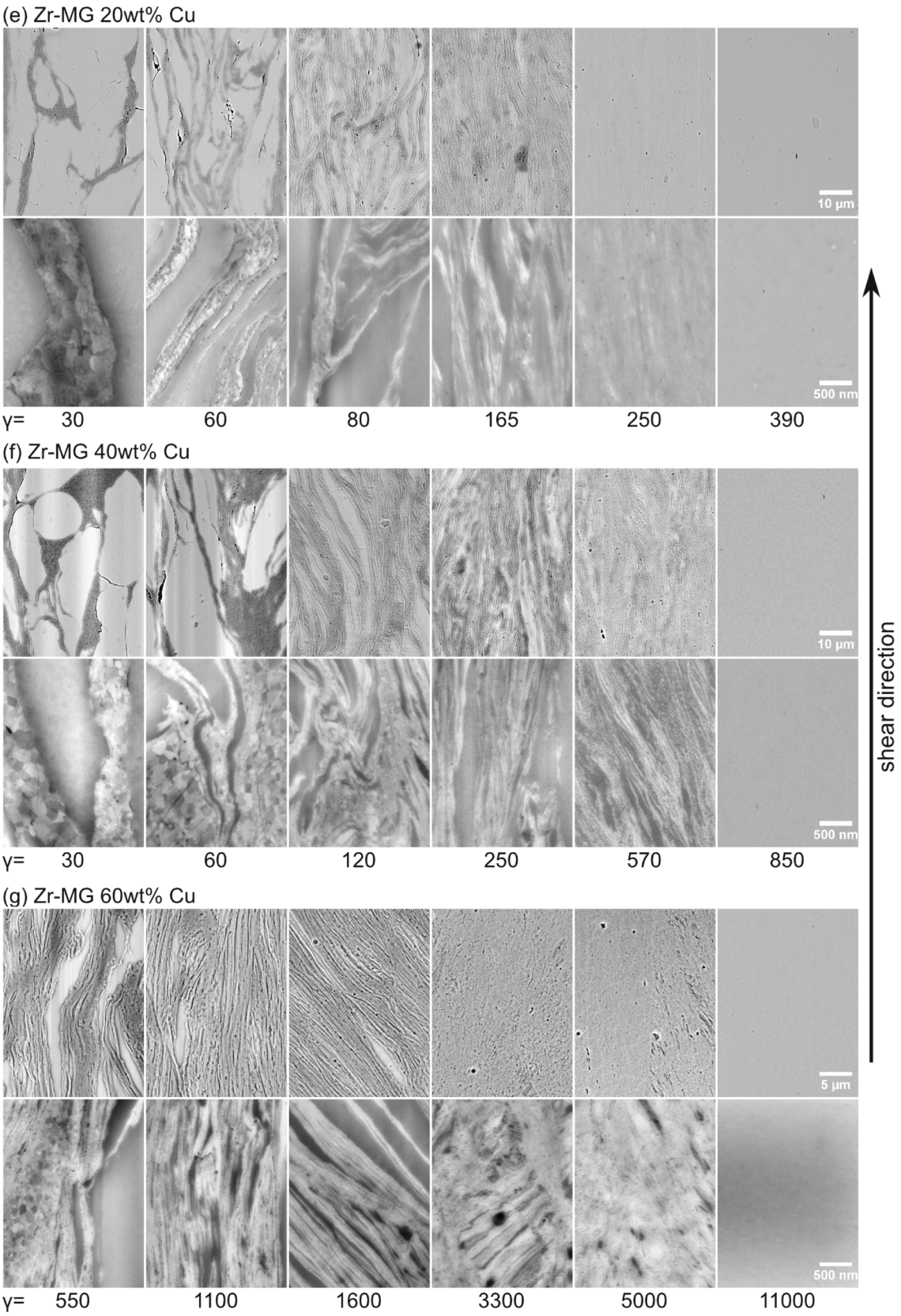

Figure 3.6.: Illustration of the microstructural evolution depending on the applied strain for (a) Zr-MG 20wt% Cu, (b) Zr-MG 40wt% Cu, (c) Zr-MG 60wt% Cu. The shear direction is indicated with a black arrow and the applied shear strain γ is added below the two micrographs with different magnifications. Redrawn from Paper B.

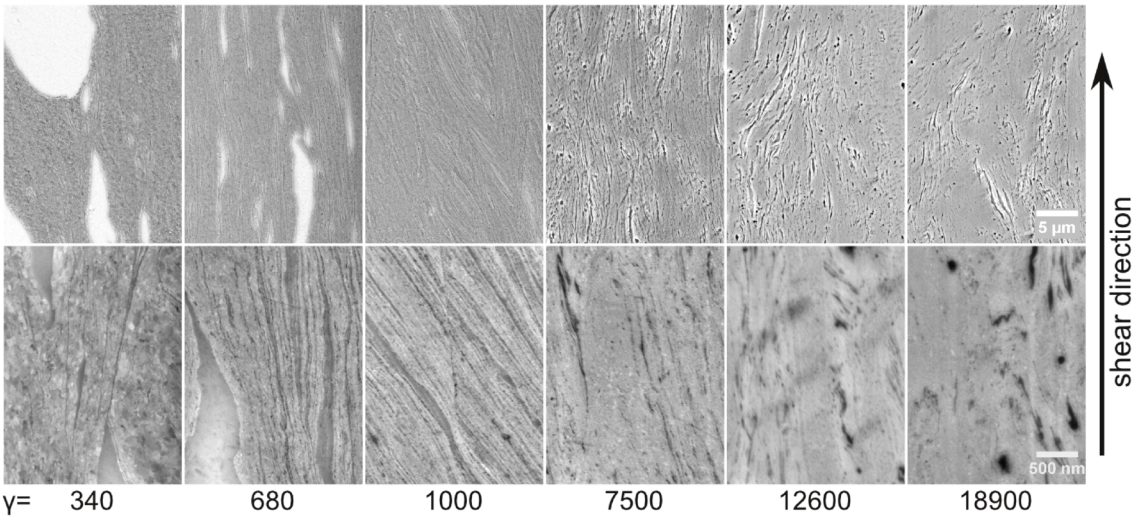

Figure 3.7.: Illustration of the microstructural evolution depending on the applied strain for Zr-MG 80wt% Cu. No full mixing of the two phases could be obtained even after $\gamma \approx 18900$. The microstructure still contains a crystalline matrix and elongated Ni-MG particles. Redrawn from Paper B.

increasing Cu-content. Zr-MG 80wt% Cu also shows hardening at low strains, but the saturation hardness lies below Zr-MG.

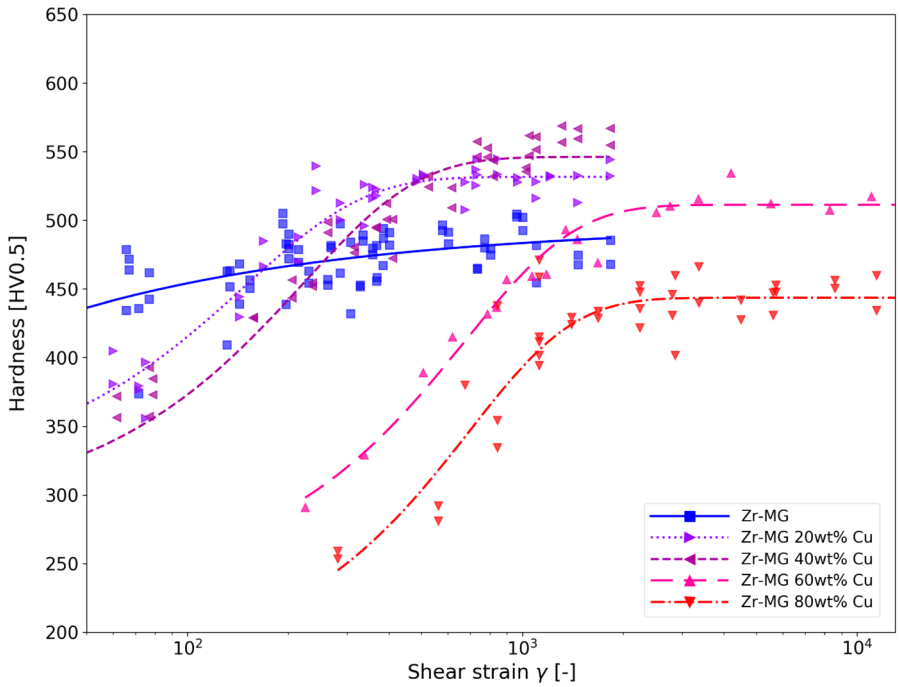

Figure 3.8.: Illustration of the Vickers microhardness as a function of the applied shear strain of Zr-MG and four composites (Zr-MG Xwt% Cu, X=20, 40, 60, 80). The hardness depends strongly on the applied strain until saturation is reached. The required strain for saturation depends on the Cu-fraction. Redrawn from Paper B.

In Figure 3.9 a, XRD measurements for all four compositions plus Zr-MG and deformed Cu powder are shown. For Zr-MG 60wt% Cu, measurements of three specimens with increasing numbers of turns are shown. The crystalline Cu peak is clearly visible after 50 turns, but as the number of turns is increased, this peak shrinks until only the amorphous peak is left after 500 turns. Zr-MG 20wt% Cu and Zr-MG 40wt% Cu, show both a typical amorphous peak and only a small hump (indicated with arrows) of the crystalline Cu is still detectable. A linear correlation between the position of the amorphous peak and the at% of Zr can be seen in Figure 3.9 b. For Zr-MG 80wt% Cu, the amorphous peak is nearly invisible as the intensity of the crystalline Cu is much higher. Even after 500 turns, the Cu shows a pronounced crystalline peak, even though its position is shifted and broadening occurs compared to pure Cu powder. The shifting can be explained by dissolving small fractions of the MG into the Cu and the strong refinement of the Cu grains into the nanometer regime leads to a peak broadening.

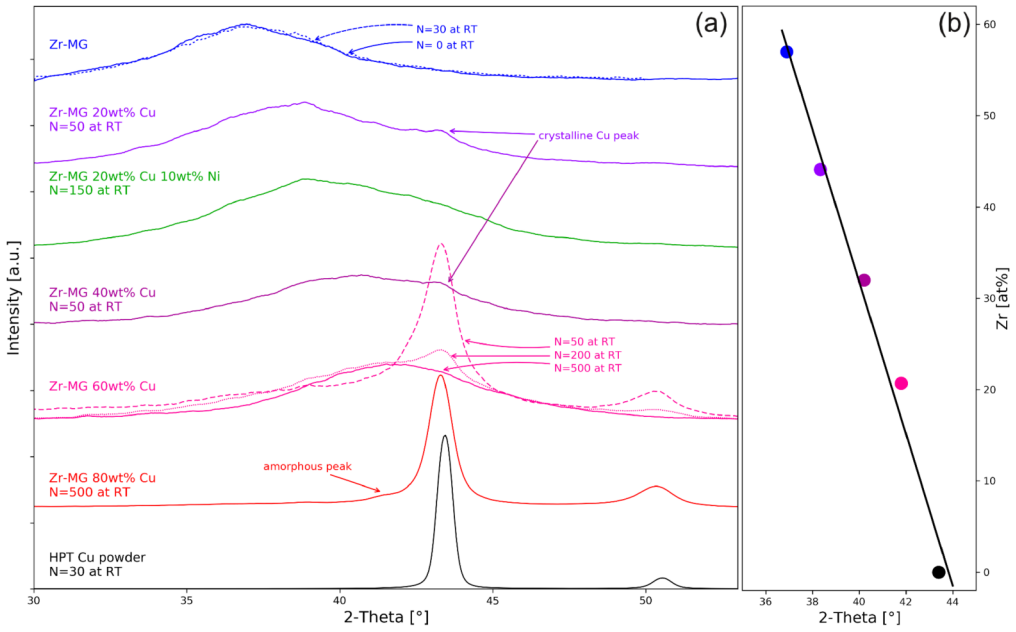

Figure 3.9.: (a) XRD results for different Zr-MG composites. All composites but Zr-MG 80wt% Cu show only one amorphous peak after sufficient deformation. For Zr-MG 60wt% Cu, the influence of the applied strain is shown, as three samples with different numbers of turns were measured. The large crystalline Cu peak decreases as the number of turns increases until only the broad amorphous peak remains. (b) The peak position depends linearly on the Zr-content. Redrawn from Paper B..

Ni-MG and crystalline Cu

SEM micrographs in Figure 3.10 show the microstructure for three different composites containing Ni-MG and crystalline Cu. Ni-MG 20wt% Cu (a) and Ni-MG 40wt% Cu (b) show both an elongated microstructure, whereas, increasing the amount of the softer phase to 70wt% leads to an Cu matrix with elongated, but still very large, Ni-MG particles (c). Correlations seen for Zr-MG + Cu are relevant for these composites too. Achieving full welding of composites with lower fraction of the softer Cu-phase requires higher amounts of applied strain, but on the other hand, high fractions of Cu delay a deformation and refinement of the harder amorphous phase. Due to the higher initial hardness of Ni-MG (640 HV), the HPT process was more difficult.

Fe-MG and crystalline Fe or Co

A benefit of BMGCs is that adding of a softer phase can help to deform harder MGs such as Fe-MG. It was shown for single phased Fe-MG that no fully dense and amorphous specimen could be produced due the high hardness of the MG compared to the anvils. A softer phase acts as a glue and therefore, consolidation is reached fast and additionally, the deformation of the MG particles is supported. In Figure 3.11, micrographs of three BMGCs with Fe-MG and crystalline Fe or Co are shown. In Figure 3.11 a, a SEM micrographs Fe-MG 20wt% Fe with 3 turns at room temperature can be seen. The applied shear strain is high enough to obtain a consolidated composite, but the refinement of the microstructure is limited

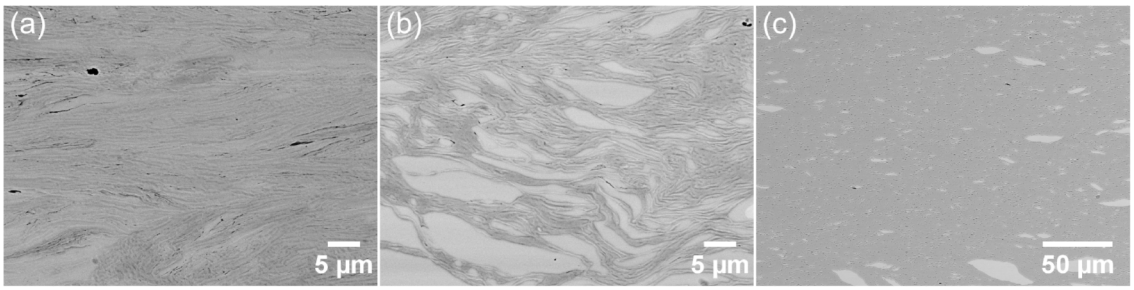

Figure 3.10.: SEM micrographs of three different composites, (a) Ni-MG 20wt% Cu, (b) Ni-MG 40wt% Cu and (c) Ni-MG 60wt% Cu. All composition show an elongated microstructure. Lower fraction of the soft Cu enhances the co-deformation and refinement of the Ni-MG particles, but more defects in the form of cracks along phase boundaries due to incomplete welding are detectable.

due to welding of specimen and anvils. Moreover, cracks are still visible. In Figure 3.11 b and c, SEM micrographs of Fe-MG 40wt% Fe, which was deformed for 5 turns at 500 °C are shown at two different magnifications. A crack free and dense microstructure can be seen, but again only limited refinement is possible due to welding of the sample and the tool. The black spots in the Fe-MG (c) are caused by etching during the polishing step. Adding crystalline Co instead of Fe decreases the problem of welding and samples with 50 turns could be fabricated, of which one optical micrograph of Fe-MG 75wt% Co is shown (Figure 3.11 d). The high fraction of the softer phase leads to a concentration of the deformation in Co and most of the Fe-MG particles still show a round shape as they are nearly undeformed. Therefore, the right fraction of the two phases has to be found. Higher contents of the softer phases simplifies the HPT process, but the softer phase will sustain the majority of the strain leading to nearly undeformed Fe-MG particles. If the content of the crystalline phase is reduced, Fe-MG particles are more deformed, but also higher hardening is observed. This causes problems during the HPT-process and reduces the number of the possible turns drastically.

Zr-MG or Ni-MG and crystalline Al

Micrographs of Ni-MG 10wt% Al(a), Ni-MG 20wt% Al (b), and Zr-MG 40wt% Al (c) are shown in Figure 3.12. Similar to Cu, the soft and ductile Al acts as glue and holds the MG-particles together. The shear strain during the HPT-process leads again to an elongated microstructure and with higher strains the thickness of the amorphous and the crystalline lamellae decreases. However, Al leads to pronounced thinning of the disk during the HPT process. Therefore, touching of the anvils is common. This reduces the number of possible turns and additionally, pronounced formation of deformation bands can be detected. Especially Ni-MG 10wt% Al shows such a heterogeneous deformation with cracks, undeformed round Ni-MG particles and regions with a fine lamellar structure positioned next to each other (a). For all composites with crystalline Al, the obtained microstructures were more heterogeneous compared to Zr-MG + Cu or Ni-MG + Cu. No samples have been used for further characterization.

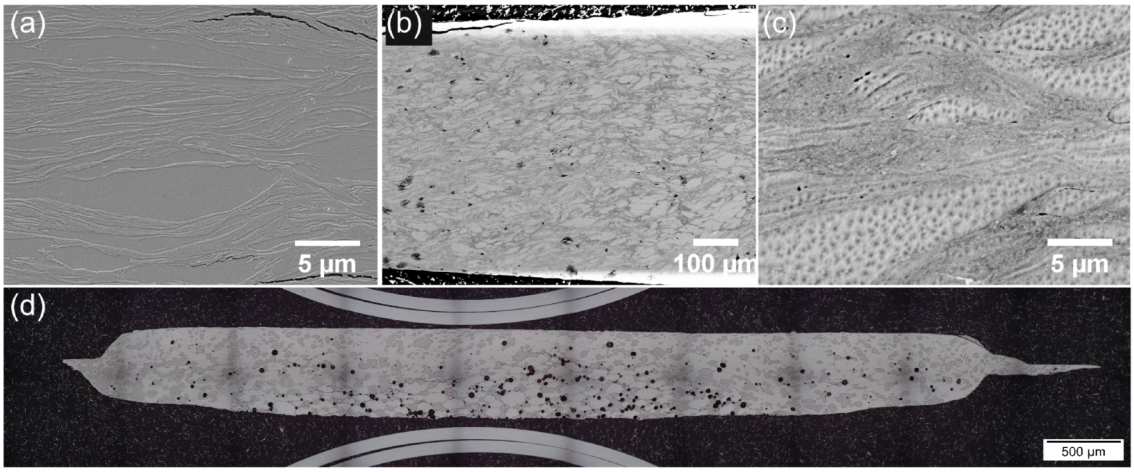

Figure 3.11.: Micrographs of three different Fe-MG composites, (a) SEM micrograph of Fe 20wt% Fe with 3 turns at room temperature, (b) and (c) Fe-MG 40wt% Fe with 5 turns at 500 °C, and (d) optical micrograph of Fe 75wt% Co with 50 turns at room temperature. The addition of the softer crystalline phase enables the fabrication of consolidated specimens.

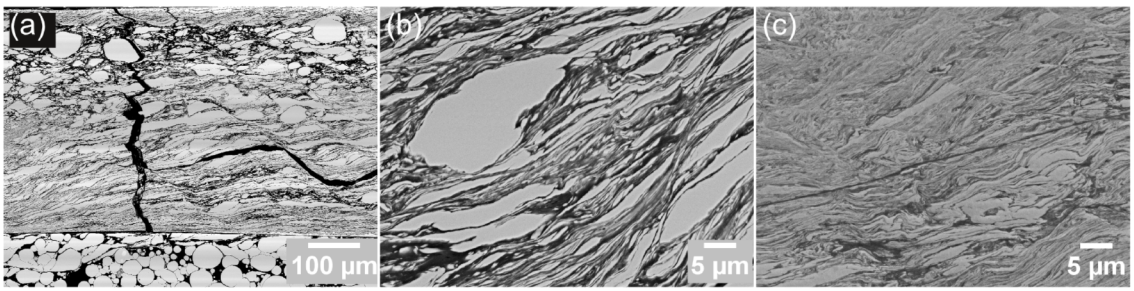

Figure 3.12.: SEM micrographs of (a) Ni-MG 10wt% Al, (b) Ni-MG 20wt% Al and (c) Zr-MG 40wt% Al. All samples show a deformation and refinement of both phases, but also stronger deformation localization compared to the composites containing crystalline Cu. Especially Ni-MG 10wt% Al show strong localization, which leads to nearly undeformed areas and cracks next to strongly refined lamellae.

3.2.2. Amorphous/amorphous composites

Only few techniques exist to produce BMGCs with two different amorphous phases. As powders can be used as starting materials for HPT, it is possible to produce such composites simply by mixing of two different amorphous powders. The concept was proven by producing Ni-MG + Xwt% Zr-MG (X=30,50) and the evolution of the microstructure was investigated by means of SEM, TEM, X-ray diffraction and microhardness.
In Figure 3.13, SEM micrographs show the evolution of the microstructure depending on the applied strain for both compositions. In the beginning, the softer phase - for this combination Zr-MG - sustains most of the deformation and acts as a glue between the harder Ni-MG particles. This behavior is similar to amorphous/crystalline composites, but as Cu has a lower hardness, Zr-MG requires more applied strain until it is distributed evenly between the harder Ni-MG particles. As the strain increases, the deformation is more evenly distributed and a lamellar structure is formed. The lamellae refine and mixing of the two phases occurs until only one phase can be detected in the SEM micrographs. Comparing the two compositions, the one with higher contents of Zr-MG shows a faster densification in the beginning as more of the softer phase is available to hold the marginally deformed Ni-MG particles together. Lesser content of Zr-MG enhances co-deformation of the two phases and the saturation containing only one phase is reached at lower applied strains.

The mixing of the two amorphous phases can be seen in the XRD measurements. Figure 3.14 a shows the intensity depending on the scattering value (see equation 3.1) for the two single phased MGs and the two composites. For Ni-MG 50wt% Zr-MG, two measurements at different applied strains are shown. For lower applied strains, two distinct amorphous peaks are measured, but as the deformation increases and complete mixing is reached, only one amorphous peak remains. Alike to the composites starting with amorphous and crystalline powders, Figure 3.14 b shows that the position of the saturation peak depends linearly on the volume fraction of Ni-MG.

Microhardness measurements also show a dependence on the ratio of the two phases (Figure 3.15). The hardness of the two BMGCs lie in between the hardness of the two single phase MG, whereas Zr-MG has the lower and Ni-MG the higher one. The hardness evolution shows again a strong increase at lower strains as

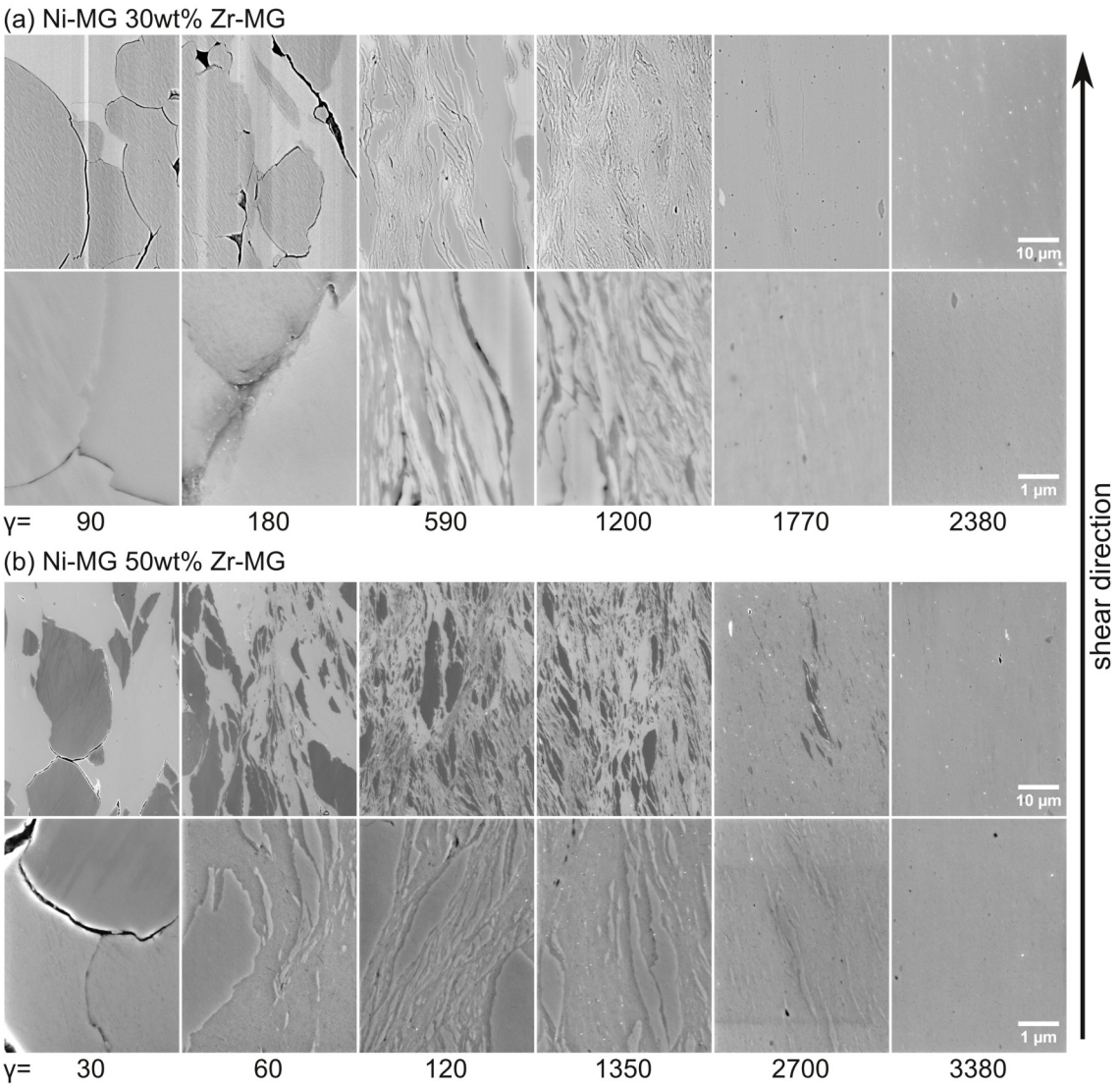

Figure 3.13.: Illustration of the microstructural evolution by means of SEM micrographs of (a) Ni-MG 30wt% Zr-MG and (b) Ni-MG 50wt% Zr-MG. The shear direction is indicated by the black arrow and the applied shear strain increases from left to right. The two micrographs at the same γ are from the same area, but at different magnifications. Redrawn from Paper C.

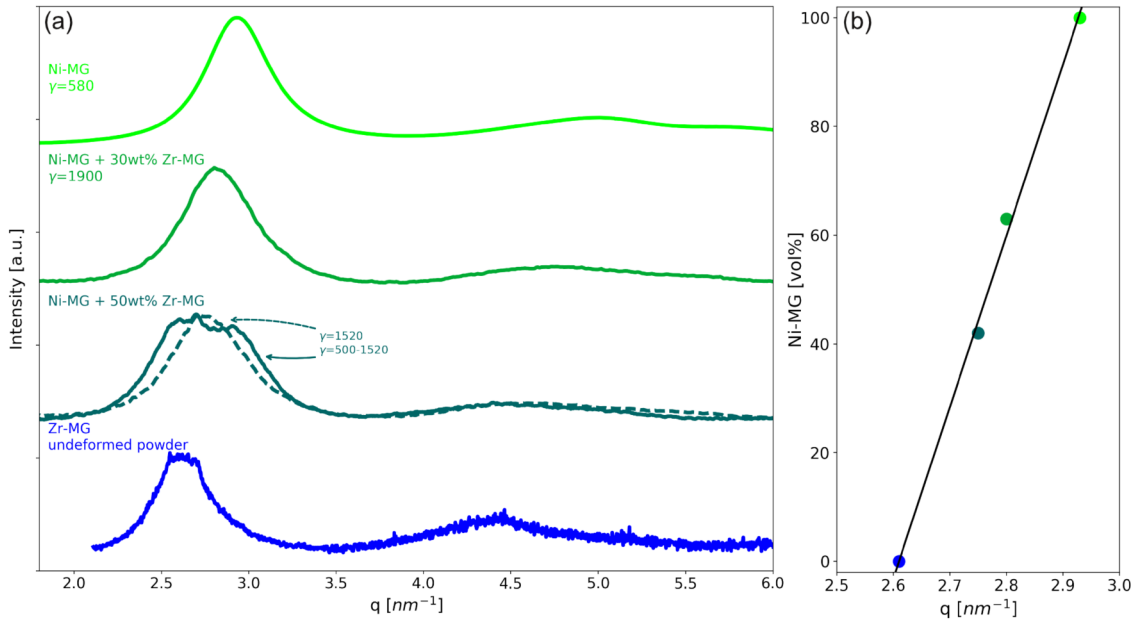

Figure 3.14.: (a) XRD results of the two initial undeformed MG-powders and the two investigated BMGCs. At saturation only one amorphous peak is visible, whereas, two peaks are visible for the transition microstructure (measured for Ni-MG 50wt% Zr-MG). The position of the saturation peak depends on the composition of the BMGCs (b). Redrawn from Paper C.

the consolidation and densification process progresses. With higher strains, the curves show less hardening, which is now caused by mixing of the two phases and maybe the refinement of the lamellar structure. The saturation hardness does not depend linearly on the vol% of Ni-MG and is higher than the rule of mixture predicts. The TEM micrograph in Figure 3.16 shows the refinement of the lamellae below 10 nm, which are wavy due to SBs. Additional to conventional TEM, also nanobeam electron diffraction was performed. Thereby, a nanobeam scans over an area and the resulting diffraction patterns are recorded. The advantages of the small beam is that the probed volume and the averaging are reduced. This allows the investigation of very fine microstructures and boundaries. MGs show usually broad peaks, where the positions are mainly governed by the compositions. Diffraction of a composite in which the phases are not mixed and superposed diffraction patterns of two separate specimens containing each only one of the phases show the same results. However, mixing of phases leads to a change of the peak position and for fully mixing only one peak is left. In Figure 3.16, an overlay of the local diffraction radius on a conventional TEM micrograph can be seen. The radius of the peak position is color coded and thereby, the two MGs are clearly distinguishable. Mixing at the boundaries can be seen as the measured

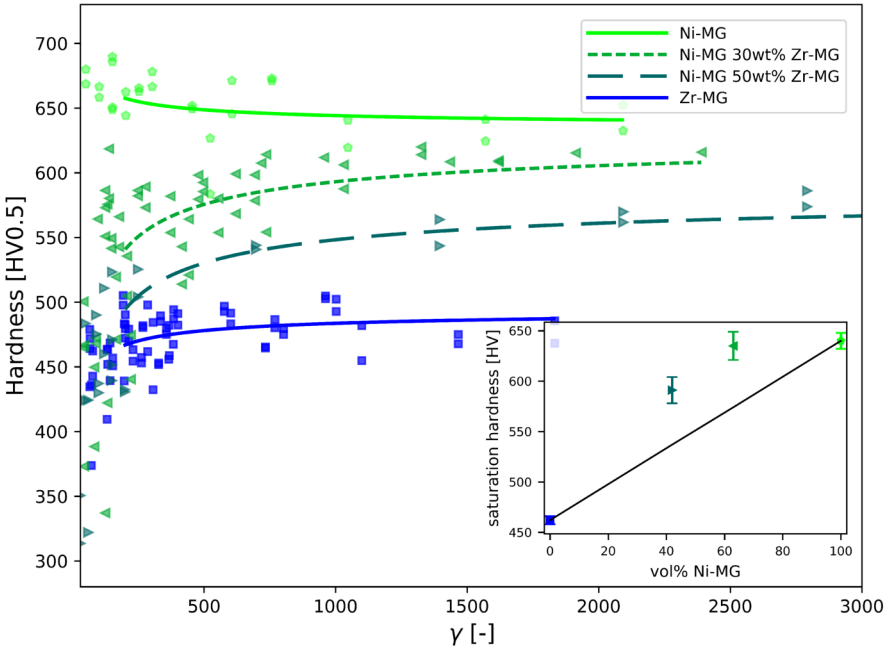

Figure 3.15.: Illustration of the Vickers microhardness evolution of the two single phased BMGs and the two BMGCs as a function of the applied strain. The hardness of the BMGCs lies between the two BMGs and it can be seen that the saturation hardness are higher than the rule of mixture predicts in the inlet. Redrawn from Paper C.

radius changes gradually from one to the other glass.

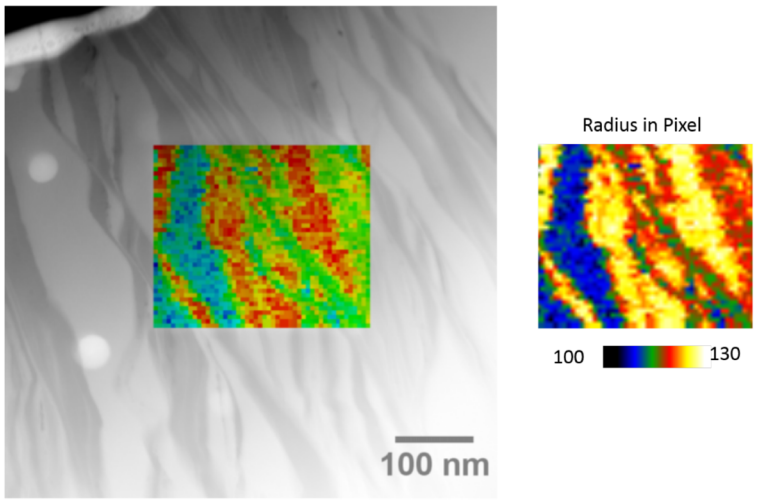

Figure 3.16.: Illustration of the change of the diffraction peak radius during nanobeam diffraction in the TEM. The radius depends on the composition of the mixed phase and by using beam and step size of 1 nm, the mixing of the two phases can be seen between the lamellae.

3.2.3. Possible composition range of mixing

The saturation microstructure for most investigated composites in this thesis contains only one amorphous phase. The high applied shear strain makes mixing of the two phases possible for amorphous/crystalline and for amorphous/amorphous composites. Figure 3.6 and Figure 3.9 show mixing of the amorphous Zr-MG and the crystalline Cu up to at least 60wt% of Cu. An additional sample with Zr-MG 20wt% Cu 10wt% Ni was produced to verify transferability to other metals and composites with three different phases. In Figure 3.9, the diffraction pattern contains only amorphous peaks indicating mixing of all three phases. Also Ni-MG + Zr-MG show a single phase microstructure at saturation in SEM (Figure 3.13) and in X-ray diffraction (Figure 3.14). The possible range in which fully amorphous structures can be obtained for the invested composites in this thesis can be seen in Figure 3.17 (Zr-MG + Cu in red and Ni-MG + Zr-MG Zr-MG in green). Additionally, compositions from literature, which could be generated as BMGs, are added. Compared to conventional methods for BMG fabrication, a wider range of compositions are feasible and this can be used to investigate possible new compositions.

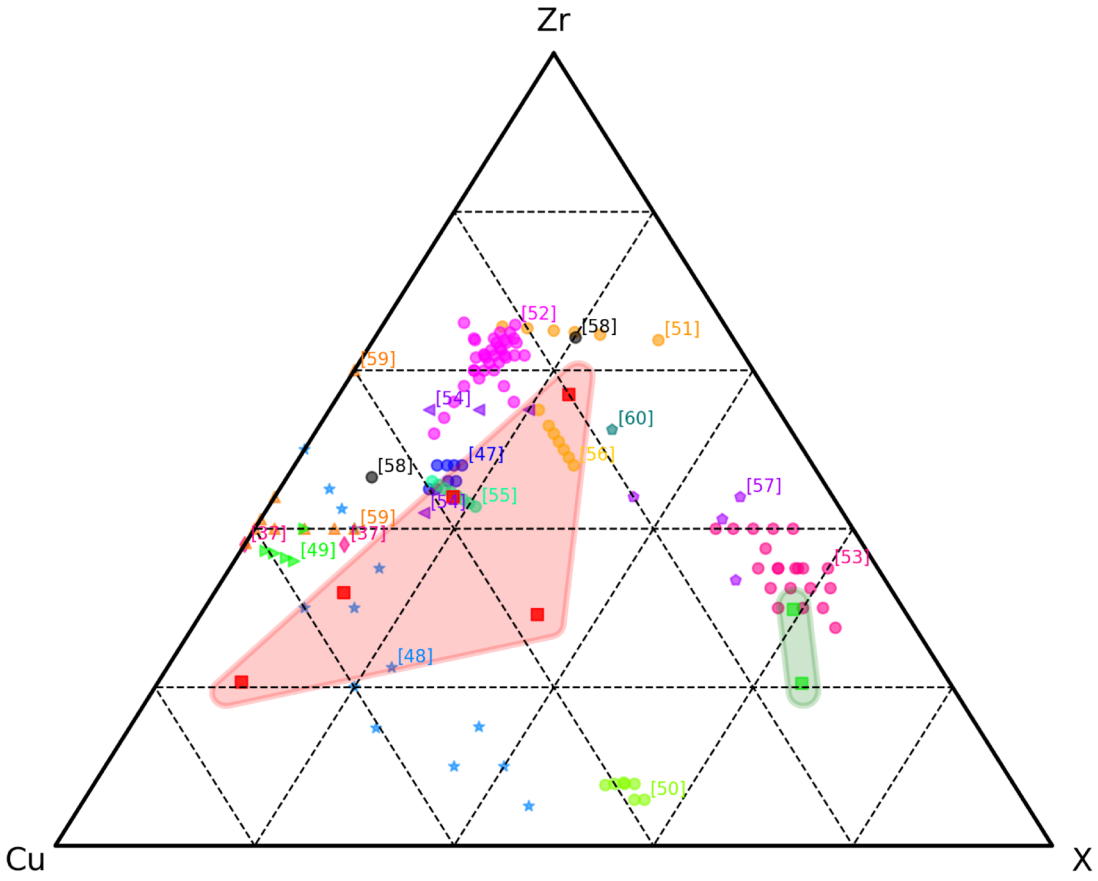

Figure 3.17.: Illustration of the verified range of composition for achieving a fully amorphous structure compared to BMG compositions from literature. All added elements but Zr and Cu are summed up in X to make the complex compositions comparable. Redrawn from Paper B.

3.3. Mechanical properties

Besides showing the possibility of HPT to fabricate BMGCs, the other main focus of this thesis laid on investigating their mechanical properties. The influence of the second phase, its dimension and orientation was studied by means of nanoindentation (including strain rate jump testing and at elevated temperature), in-situ micropillars compression testing, and tensile testing.

3.3.1. Nanoindenation

Nanoindenation can be used to probe the different phases in a composite, but also to investigate their deformation behavior. BMGs show often a serrated flow behavior during nanoindentation, whereas each serration corresponds to the propagation of a SB [51]. The size and number of serration depends on the testing temperature, strain rate [52–55], tip geometry [56], and also on residual stresses [57, 58]. Annealing of BMGs influences the free volume, Young's modulus and the hardness, but the serration behavior does not change. Interestingly, the serration behavior is similar for different BMGs if they are tested at the same homologous temperature [59]. Even though the correlation of the serration and the deformation behavior seems obvious, the analytical evaluation is not straightforward. Different techniques were developed to link the serrations to activation volumes and energies such as using a cooperative shear model to link the first pop-in for different strain rates to the strain rate sensitivity [60], examining the critical strain leading to the first pop-in using a spherical indenter [61], and using a mean field theory to correlate annealing temperatures to slip avalanches [62]. A problem of the first two methods is the dependency of serration length on the indentation depth [63]. At small indentation depth the serrations are smaller than the measurement error. In crystalline materials the activation volume is commonly calculated by determining hardness and strain rate sensitivity [64], but this method is not valid for amorphous materials, because a plasticity caused by dislocation with a corresponding burgers vector is assumed. Spaepen proposed a model, which links a plastic rate of a flow unit with an external stress [65]. The advantage of this method is its universality as there are no specific requirements for what causes the deformation. It can be atoms, dislocations or any other kind of a flow unit, which fits the common idea

of shear transformation zones as main cause of deformation in MGs. The plastic flow rate $\dot{\gamma}$ is linked to a net jump frequency k_a of flow units under the influence of external stress τ:

$$\dot{\gamma} = n\gamma_0 v_0 k_a \sinh\left(\frac{\tau\gamma_0 v_0}{kT}\right) \exp\left(-\frac{\Delta G}{kT}\right), \tag{3.2}$$

where n is the concentration of flow defects, γ the shear strain produced by rearranging of a flow defect, v_0 is the volume of a flow defect, k the Boltzmann constant and ΔG the activation energy. Small scaled strain rate jump tests can be conducted with nanoindentation. By using different strain rates the equation can be simplified to

$$\frac{\dot{\gamma}'}{\dot{\gamma}} = \frac{n'\gamma_0' \sinh\left(\frac{\tau'\gamma_0' v_0}{kT}\right)}{n\gamma_0 \sinh\left(\frac{\tau\gamma_0 v_0}{kT}\right)}, \tag{3.3}$$

where variables with prime and without prime correspond to two different strain rates. Still, several variables have to be determined. The strain rates and temperatures are the ones used in the nanoindentation tests, but the concentration of the defect, the shear strain per defect and the shear stress must be obtained from the tests. In Figure 3.18, indentation jump tests at two different temperatures are shown. For both temperatures, Young's modulus and hardness are plotted as the function of the indentation depth. At room temperature, hardness and Young's modulus show no dependence on the strain rate, but at higher temperature the hardness changes with the variation of the strain rates. The shear stress was calculated for each strain rate and temperature by using the respective hardness and the constraint factor c with $\tau = \frac{H}{c\sqrt{3}}$, where c was calculated according to a method proposed by Leitner *et al.* [66].

The change in strain rate also influences the load-displacement curves in Figure 3.18 b and e, whereas the serration size is more affected at room temperature and at elevated temperature the slope of the curve differs for the three strain rates. The size and concentration of defects were determined by the size and number of serrations, which were identified by plotting the distance of two neighboring data points divided by indentation depth as a function of the indentation depth (Figure 3.18 c and f). As most of the data is equally spaced, the larger distance of the data points at the serration is obvious. This data points were further used to calculate γ_0 with $\gamma_0 = d_s/h$, where the definition of d_s and h can be seen in the inlet of (Figure 3.18 b and e). The linear dependence of the serration size on the

indentation depth was used to calculate the number of the serration n by using

$$h_n = h_0(1+\overline{q})^n \tag{3.4}$$

and

$$\overline{q} = \frac{1}{n}\sum_{i=1}^{m}\frac{h_i - h_{i-1}}{h_i}\,, \tag{3.5}$$

where $\overline{q}$ is the distance between two serrations and can be estimated from Figure 3.18 b and e. This process could be used to evaluate all indents and to determine the activation volume. To calculate also the activation energies, k_a is missing. It can be estimated by approximating each atom as a harmonic oscillator with an energy of $E = 3kT$ and taking the maximal displacement Δx at each temperature via the thermal expansion of the materials ($\Delta x = \alpha r \Delta T$, with r as the atomic radius). The frequency k_a is then calculated with the atomic mass, m, by

$$k_a = \sqrt{\frac{6k}{mT}} * \frac{1}{2\pi\alpha r}\,. \tag{3.6}$$

Different materials (Zr-MG, Zr-MG 20wt% Cu, Zr-MG 60wt% Cu, Ni-MG, Ni-MG 30wt% Zr-MG, and additional a cast ZrBe-based MG) were tested at elevated temperature, which can be found in detail in Paper D. Interestingly, all samples show a similar behavior if the results are shown as a function of the homologous temperature. While hardness and Young's modulus show a decrease as the glass transition temperature T_g is approached, activation energy and volume show more complex curves. The activation energies increase steadily until approximately T_g and decline with further increasing temperature. In contrast, the activation volumes are nearly constant until T_g and then show a strong increase. The increase of the activation energy approaching T_g is surprising. One would assume a decrease of the activation energies, because MGs are known to deform more easily at higher temperature. However, literature showed a change in diffusion mechanism from a solid-like diffusion to viscous liquid-like diffusion at temperatures higher T_g. The increase can be explained by participating of different atoms. At lower temperature the flow units are mainly composed of the most mobile atoms (probably the smallest) and at higher temperature also the other - less mobile - atoms participate, and thereby the activation energy increases. The tested BMGCs show a similar behavior as its dominant amorphous

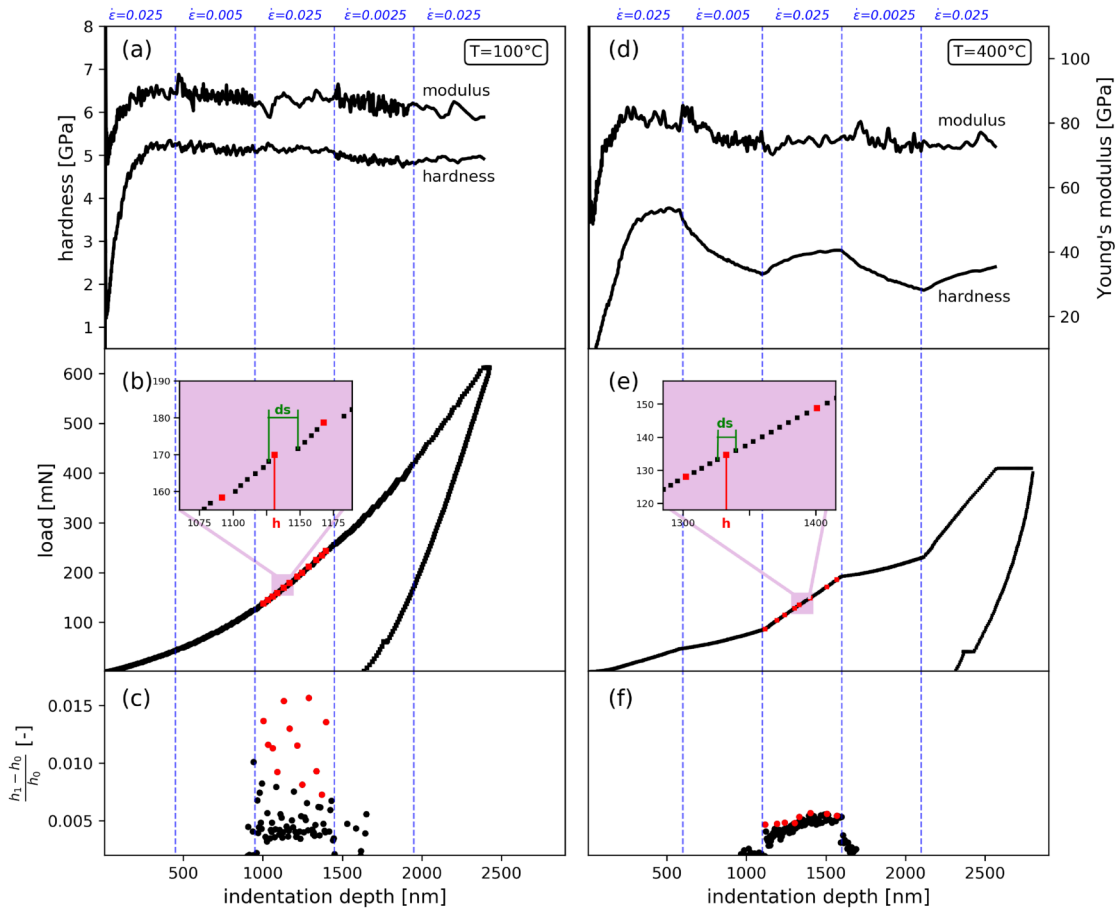

Figure 3.18.: Illustration of a nanoindentation strain rate jump tests of a Zr-MG at 100 °C and 400 °C. The regions of the different strain rates are marked by lines and their values can be found at the top of the diagrams. (a and d) show the hardness and Young's modulus as a function of the indentation depth and in (b and e) load-indentation depth curves can be found. The serrations are identified by higher distance to the neighboring data points and the determination can be seen in (c and f). Redrawn from Paper D.

phase.
Furthermore, the influence of rejuvenation by HPT and thermal cycling was investigated. For both treatments no trend is clearly visible, even though, differences higher than the error are determined between the individual measurements. This can be explained by an inhomogeneous deformation process during the HPT process as micrographs of etched specimens indicate. Therefore, a cast bulk sample (Vit105) was deformed for 10 turns via HPT and the nanoindents were performed along a line on the cross section at a radius 2 mm. The measured and calculated properties show only small differences (Figure 3.19). The sample was etched (HNO_3:Ethanol - 1:3, $-20\,°C$, 7 V for 60 s modified from [67]) after nanoindentation. Thereby, SBs are visualized, showing their fine distribution (Figure 3.20) and it can be seen that each indent probes deformed and undeformed material.

Nanoindentation was also used to investigate changes in hardness and Young's modulus depending on the local microstrostructure in BMGCs. A nanoindentation map for Ni-MG 30wt% Zr-MG is shown in Figure 3.21 a, containing 24 indents. Each impression is colored according to its hardness and for some it is shown how the two phases were marked by hand. An automatic classification of the two phases did not work, because of the height difference due to the indents. The phase fraction was only measured in the indent, whereas for the lamellae thickness the area in the vicinity of the indent was used. ImageJ was used to determine phase fraction and a mean lamellae thickness. In Figure 3.21 b and c, the hardness and Young's modulus are plotted as a function of the phase fraction and the mean lamellae thickness. The former shows a linear dependence of increasing hardness and Young's modulus on the volume fraction of Ni-MG, but the latter shows no dependence. These mechanical properties seem to be mainly governed by the compositions and not the microstructure of the BMGCs. However, important factors as errors in the determination of the two phases (to thin lamellae, only information from the surface) and the formation of a new phase, which is not really detectable in the SEM images impede a clear conclusion.

In summary, the influences of the evolving microstructure on hardness and Young's modulus were investigated via nanoindentation mapping and nanoindentation strain rate jump tests. Concerning microstructure, the local chemical composition had a major influence, whereas a change of the lamellae thickness

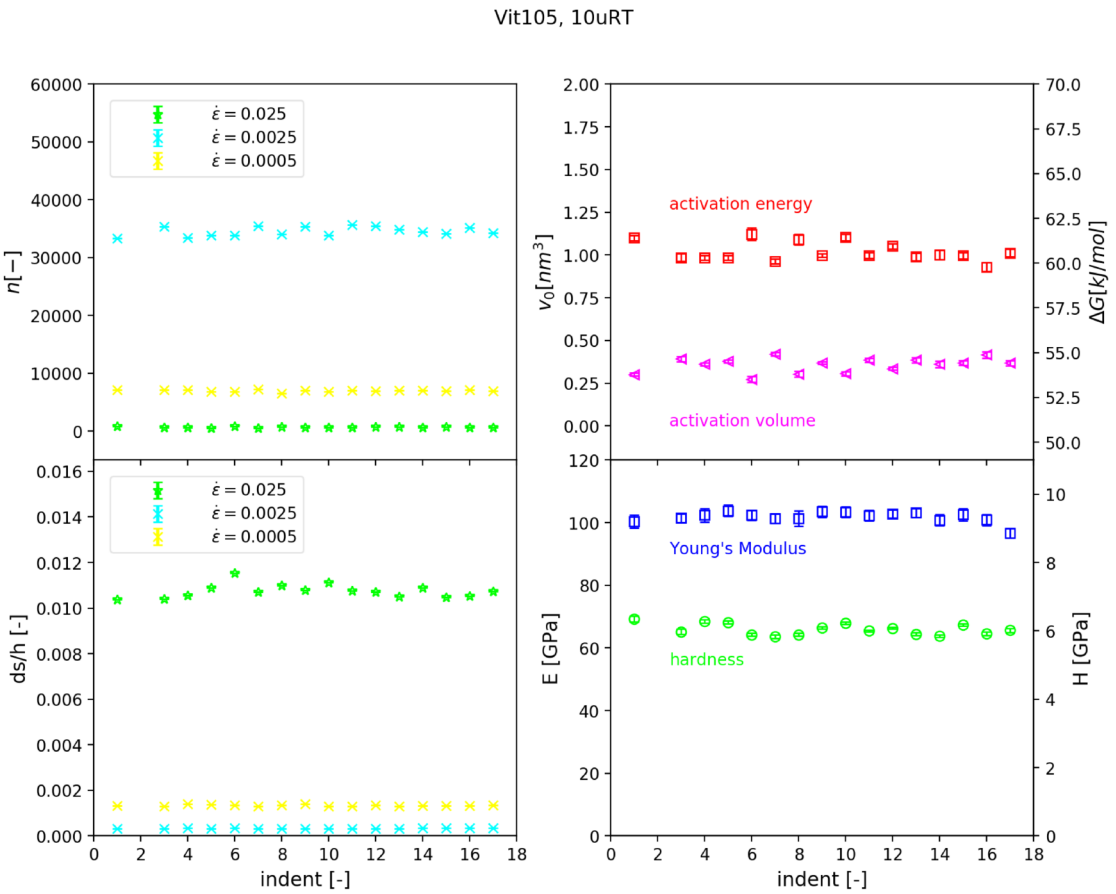

Figure 3.19.: Plastic strain, number of serrations, hardness, Young's modulus, activation energy and activation volume for 16 indents. The indents were aligned at one radius in a deformed BMG (Vit105) to investigate the heterogeneity of the HPT-deformation. Only small differences between the indents are visible.

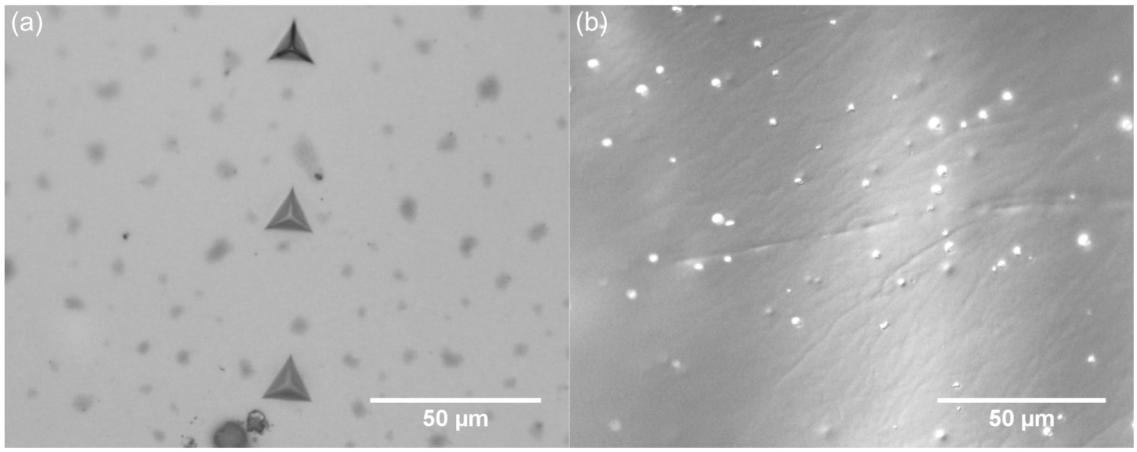

Figure 3.20.: (a) Optical micrographs of nanoindenation imprints in Vit105 deformed for 10 turns. All indents were conducted along a line at radius 2 mm to investigate the heterogeneity of a sample subjected to HPT-deformation. (b) Optical micrographs of the same area after etching. Fine distributed shear bands are visible.

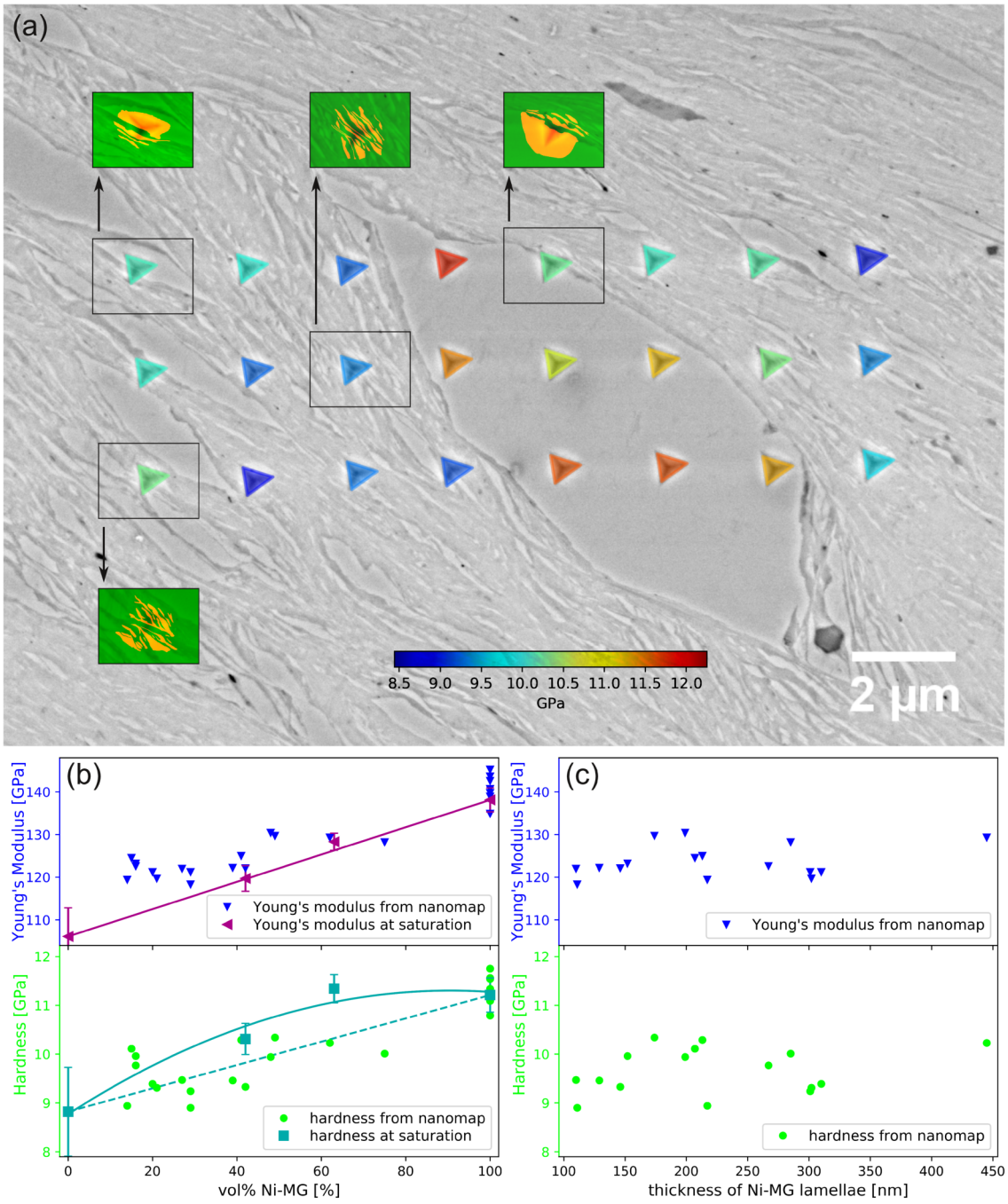

Figure 3.21.: (a) Illustration of a nanoindentation property map with colored the residual impression according to the respective measured hardness and micrographs with colored phases of four representative indentation marks are included. Graphs of Young's modulus and hardness as a function of the (b) vol of Ni-MG and of the (c) mean thickness of the Ni-MG lamellae can be seen. Redrawn from Paper C

seemed to have only little effect. Activation energy and volume were mainly affected by the chemical composition and the homologous testing temperature. Here, additional treatments like HPT or thermal cycling had no pronounced effects.

3.3.2. Micropillar compression

Mechanical properties of BMGCs depend on a variety of factors such as the types of the two phases or the microstructure. For increasing the ductility, a high fraction of a ductile crystalline phase is favorable especially if a fine homogeneous distribution exists [42–44, 46–48, 68–70]. A fabrication method to individually change dimensions and fractions of the both phases in composites is sputtering. It can be used to produce multilayers containing amorphous films [71–73]. Micropillar compression testing on amorphous ZrCu/Cu systems demonstrates a critical thickness for the amorphous phase of approximately 20 nm, under which the nucleation of SBs is not possible [74, 75] and a critical thickness of the crystalline phase thicker than 100 nm to efficiently stop the propagation of SBs [76]. However, no studies known to the author's knowledge investigated the influences of the orientation of the loading direction to the lamellae. Micropillar compression tests on nanocrystalline perlite and nanocrystalline steel showed a change of the deformation behavior if the orientation of the lamellar structure to the loading direction is changed [77]. Lamellae normal to the loading direction formed a SB, while dislocation movement parallel to the interfaces was the main contribution to deformation in pillars with a lamellar structure inclined to the loading direction (confined layer slip). Kink bands were observed for an orientation of the lamellae perpendicular to the loading direction.

In the course of the present thesis many different BMGCs were fabricated, whilst combining different materials and adjusting the microstructure by changing the applied shear strain. The investigation of the mechanical properties by means of pillar compression testing was only conducted on few selected materials. The investigated BMGCs contained two MGs (Ni-MG and Zr-MG) or Zr-MG and crystalline Cu, but the phase fraction, thickness and orientations were varied. Additionally, also the twp single phased BMGs were tested.
The pillars were prepared by focused ion beam focused ion beam (FIB) cutting

with dimensions of approximately $(5 \times 5 \times 10)\,\mu m^3$. The pillars were all tested in-situ inside a Zeiss LEO982 SEM equipped with an ASMEC UNAT microindenter with a constant strain rate of $10^{-3}\,s^{-1}$.
For the determination of the compliance also the bulk material next to the pillars was tested and micrograph sequences, which were conducted for all tests, were used to calculate the drift between the first and the last micrograph. Therefore, the pillar must not be loaded as this leads to a shift of the entire system. Also, the accuracy of measuring was one pixel (20 nm to 30 nm) and it was tried to reduce the error by measuring at least three different distinctive points. Additionally, the micrograph sequences were also used to determine the strain during the deformation. For that reason, each micrograph was binarized to distinguish between pillar and background and the boundary points were marked (see Figure 3.22 a). These points were then fitted linearly (see Figure 3.22 b) and the intersections of the lines were determined. The average distance between the intersections was determined for each micrograph and was aligned to the correct load value by using the time of record. However, for the recording time of the micrographs only seconds were noted, even though more than one image was taken per second. Hence, new time values were assigned to each image.
The good agreement between the corrected data and the data determined from the image sequence can be seen in Figure 3.23. In Figure 3.23 a, the uncorrected data obtained from the ASMEC is shown, while in b the corrected data is compared to the data determined from the in-situ video. A drawback of using the strain determine from the micrographs is the low number of data, and therefore, only corrected ASMEC data was used furthermore.

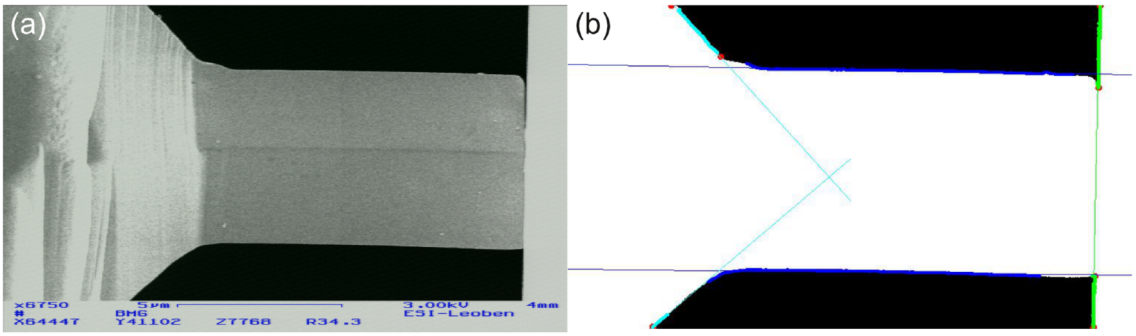

Figure 3.22.: (a) In-situ micrograph during a compression testing. (b) The same image, which was binarized and the boundary pixels are marked in color and then linearly fitted. The strain was determined by measuring the intersection of the fitted lines for the whole sequence.

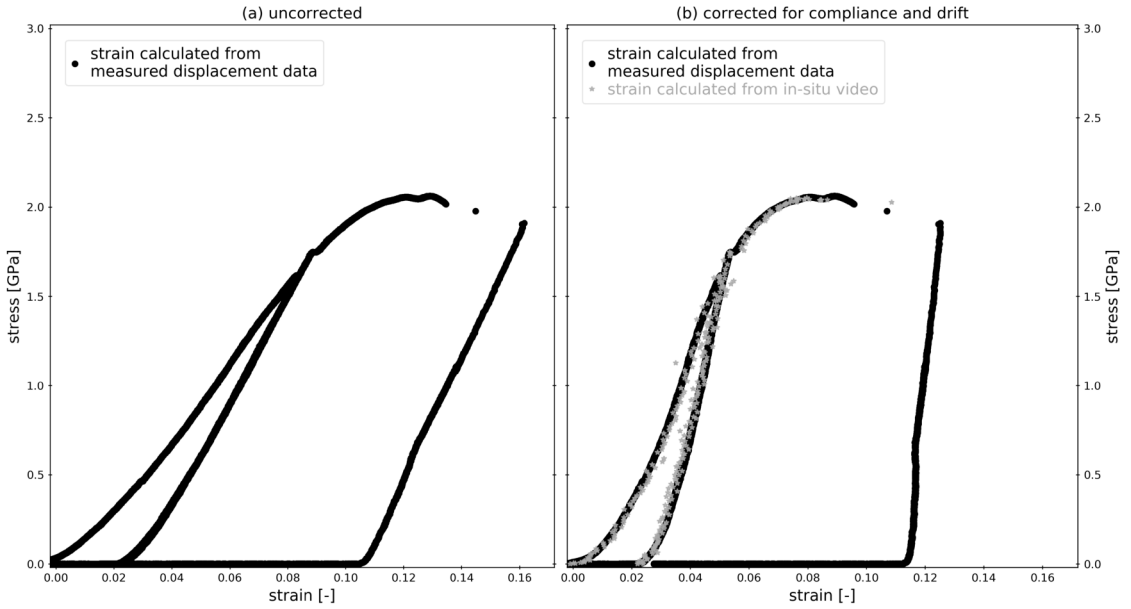

Figure 3.23.: (a) Uncorrected data obtained by ASMEC. (b) Data obtained from ASMEC corrected for the compliance of the system and the drift. Also the data obtained from the micrograph sequence is shown. Due to the good agreement and the lower number of data points obtained from the second method, the corrected ASMEC data is used furthermore. Redrawn from Paper E.

The results and a detailed discussion can be found in Paper E, but the main points are:

- The combination of phases with different mechanical properties determines strongly the deformation behavior during the compression tests.
  - Adding a second, harder, amorphous phase efficiently stops SBs and SB branching is enhanced.
  - Adding a second, softer, crystalline phase shows a lower impact.
  - However, increasing the thickness of a the crystalline layers increases the amount of deformation before even a SB is formed. Additionally, if the crystalline lamellae is thick enough, also stopping of SBs is observed.
- An effect of the high deformation during the HPT-process is the mixing of the phases, which is accompanied by an increase in hardness. This is also reflected in an increase of strength during the compression testing. Changing the lamellae thickness of amorphous/amorphous composites does increase the strength, but the higher strength of Ni-MG enables stopping of SB also at thinner lamellae compared to amorphous/crystalline

BMGCs.

- Nearly all tested composites show the formation of a fatal SB at the end, which leads to a fracture under 45° to 65° running straight through all interfaces. Only if a lamellae is oriented favorable, the SB will run along its interface and a reduction in strength and ductility is observed.
  - The only exception was one pillar with a high fraction of Cu and inclined lamellae. Here, the deformation of the Cu-lamellae led to a rotation of the pillar and therefore to a change in the stress distribution and instead of SB a kink band was formed. This kink band enhanced the ductility and distributed the deformation into a larger volume compared to SBs.

3.3.3. Tensile testing

Tensile specimens were prepared using a circular grinding tool developed by G. Rathmayer starting with a half of HPT-disk [78]. A Kammrath&Weiss testing device with an additional stereo microscope was used. Thereby, true strain and true stress could be determined. In Figure 3.24, results for samples of Zr-MG, Zr-MG 20wt% Al, Zr-MG 20wt% Cu, and Zr-MG 40wt% Cu are shown. All samples show purely brittle behavior. Even tensile samples fabricated from the same HPT-disk break at different stresses (Zr-MG) indicating that fracture is mainly governed by defects. These defects could be not fully welded areas, where the initial particle surfaces acts as cracks, phase boundaries or undeformed particles in composites, and impurities caused by the powder approach. Increasing the content of Cu leads to higher fracture strengths, but increasing the number of turns and thereby decreasing the fraction of crystalline Cu reverses this effect and a decrease is observed (see Zr-MG 40wt% Cu).

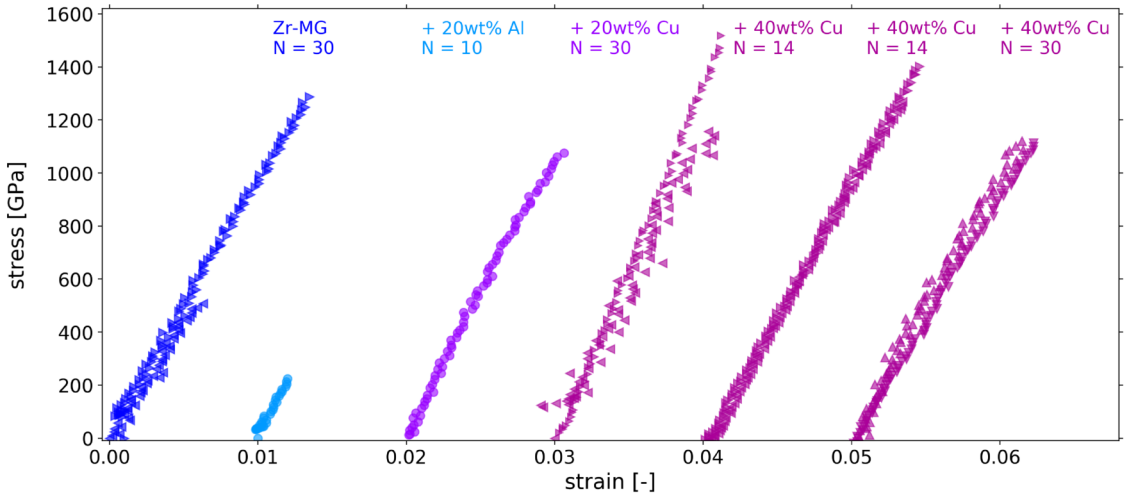

Figure 3.24.: Illustration of tensile measurements of Zr-MG and three different BMGCs. True stress versus true strain could be measured by using an optical system additional to the K&W device. For all samples a brittle behavior is measured, whereas the probability of fracture was reduced by increasing the Cu content.

4. Summary

The present thesis had two main focuses. Firstly, BMGs and BMGCs were produced via HPT and the microstructural evolution was investigated. Secondly, the mechanical properties of the BMGs and BMGCs were characterizing. Three amorphous and three crystalline powders were mixed, varying their combinations and fractions. Subsequently, HPT was used to consolidate particles and deform till very high strains. The evolution of the microstructures was investigated by SEM, TEM, X-ray diffraction and microhardness. The main conclusions are the following:

1. HPT can be used to generate BMGs and BMGCs starting from amorphous and crystalline powders. The amount of the applied shear strain is essential, because welding of the particles is a gradual process. For single phased materials, the strain necessary for densification depends mainly on the chosen amorphous powder and its hardness. In case of BMGCs, the ratio and hardness of the two phases is of great importance too. A softer phase as crystalline Cu is faster dispersed than a hard amorphous phase. The required strain for consolidation decreases if the volume fraction of the softer phase, being either crystalline or amorphous, is increased. The hardness evolution illustrates the gradual consolidation, because cracks and defects lead to higher scattering of the data. The hardness evolution illustrates the gradual consolidation, because cracks and defect lead too higher scattering of the data.
2. The HPT-process is limited by the strength of the anvils, which must be higher than the powders for a successful fabrication.
3. For BMGCs, the evolution of the microstructure depends on the properties and the fraction of the two mixed phases, as well as on the applied shear strain.
4. Due to the applied pressure and the shear deformation, an elongated microstructure is developed for all composites. The lamellar structure can

be adjusted by changing the number of turns. Phase dimensions from the micrometer to the nanometer regime can be generated.

5. At larger strains mixing of the phases occurs, which eventually leads to a microstructural saturation at very high strains. This saturation microstructure is either a single phased BMG obtained by full mixing of both phases, or nanocrystalline supersaturated solid solution with embedded amorphous nanolamellae. The required strain for reaching saturation depends on the combined materials and their fraction. If the difference in hardness is small and the fraction of the harder phase is high, the saturation is reached sooner.

The second focus was on the mechanical properties of the fabricated BMGs and BMGCs. Nanoindenation jump tests and micropillar compression tests were used to probe different mechanical properties. By the former the nucleation of shear bands was characterized, whereas the latter showed how the propagation of shear bands was influenced by a second phase.

1. The activation volume and energy at the onset of deformation describe the nucleation of shear bands and it was shown that the main influencing factors were the composition and the testing temperature. Adding a second phase does not influence the nucleation, because the phase dimensions are significantly larger than the activation volumes. Even if the composition is changed by mixing during the HPT-process, the changes of T_g are not large enough to affect the activation energy and volume.
2. Thermal cycling and the plastic deformation during the HPT-process exhibit no influence on the activation volume and energy.
3. The propagation of shear bands is influences by adding a second phase. In particular, the type of the second phase (amorphous or crystalline) as well as the size and orientation of the lamellar microstructure are of great importance.
4. An amorphous phase hinders the propagation of the shear bands more effectively, which can be explained by its higher strength. Decreasing the lamellae thickness of the crystalline phase decreases its positive influence. On the one hand, thinner lamellae have a lower capability to endure plastic deformation and on the other hand, a new brittle amorphous material is formed when the mixing of the two phases starts. the two phases are mixed and form a new brittle amorphous phase.

5. Changing the lamellae orientation influences the propagation of shear bands. A lamellae orientation in the direction of the the highest shear stress facilitates shear band propagation. This leads to reduced strength and ductility. Any deviation from this ideal orientation will promote branching and stopping of the shear bands, thereby increasing the strength and ductility.

5. References

[1] C. Boesch and H. Boesch. "Tool Use and Tool Making in Wild Chimpanzees." In: *Folia Primatol* 54 (1990), pp. 86–99. DOI: 10.1159/000156428 (cit. on p. 1).

[2] W. Klement, R. H. Willens, and P. Duwez. "Non-crystalline Structure in Solidified Gold–Silicon Alloys." In: *Nature* 187.4740 (1960), pp. 869–870. DOI: 10.1038/187869b0 (cit. on p. 1).

[3] W. H. Wang, C. Dong, and C. H. Shek. "Bulk metallic glasses." In: *Materials Science and Engineering: R: Reports* 44.2-3 (2004), pp. 45–89. DOI: 10.1016/j.mser.2004.03.001 (cit. on p. 1).

[4] J. F. Löffler. "Bulk metallic glasses." In: *Intermetallics* 11.6 (2003), pp. 529–540. DOI: 10.1016/S0966-9795(03)00046-3 (cit. on p. 1).

[5] Y. F. Sun et al. "Fabrication of CuZr(Al) bulk metallic glasses by high pressure torsion." In: *Intermetallics* 17.4 (2009), pp. 256–261. DOI: 10.1016/j.intermet.2008.07.023 (cit. on pp. 1, 12).

[6] S. Nowak et al. "Approach of the spark plasma sintering mechanism in $Zr_{57}Cu_{20}Al_{10}Ni_8Ti_5$ metallic glass." In: *Journal of Alloys and Compounds* 509.3 (2011), pp. 1011–1019. DOI: 10.1016/j.jallcom.2010.09.158 (cit. on p. 1).

[7] G. Q. Xie et al. "Ceramic particulate reinforced $Zr_{55}Cu_{30}Al_{10}Ni_5$ metallic glassy matrix composite fabricated by spark plasma sintering." In: *Materials Transactions* 48.7 (2007), pp. 1600–1604. DOI: 10.2320/matertrans.MJ200716 (cit. on p. 1).

[8] G. Xie et al. "Nearly full density $Ni_{52.5}Nb_{10}Zr_{15}Ti_{15}Pt_{7.5}$ bulk metallic glass obtained by spark plasma sintering of gas atomized powders." In: *Applied Physics Letters* 90.24 (2007), pp. 12–15. DOI: 10.1063/1.2748102 (cit. on p. 1).

[9] I. Karaman et al. "The effect of temperature and extrusion speed on the consolidation of zirconium-based metallic glass powder using equal-channel angular extrusion." In: *Metallurgical and Materials Transactions A* 35.1 (2004), pp. 247–256. DOI: 10.1007/s11661-004-0125-5 (cit. on p. 1).

[10] K. S. Kormout, B. Yang, and R. Pippan. "Deformation Behavior and Microstructural Evolution of Cu-Ag Alloys Processed by High-Pressure Torsion." In: *Advanced Engineering Materials* 17.12 (2015), pp. 1828–1834. DOI: 10.1002/adem.201500109 (cit. on p. 2).

[11] K. S. Kormout, R. Pippan, and A. Bachmaier. "Deformation-Induced Supersaturation in Immiscible Material Systems during High-Pressure Torsion." In: *Advanced Engineering Materials* 19.4 (2016), p. 1600675. DOI: 10.1002/adem.201600675 (cit. on p. 2).

[12] A. Bachmaier et al. "Supersaturation in Ag–Ni alloy by two-step high-pressure torsion processing." In: *Philosophical Magazine Letters* 94.1 (2014), pp. 9–17. DOI: 10.1080/09500839.2013.852284 (cit. on p. 2).

[13] J. Qiang and K. Tsuchiya. "Concurrent solid-state amorphization and structural rejuvenation in Zr-Cu-Al alloy by high-pressure torsion." In: *Materials Letters* 204 (2017), pp. 138–140. DOI: 10.1016/j.matlet.2017.06.032 (cit. on p. 2).

[14] H. Razavi-Khosroshahi et al. "Plastic strain and grain size effect on high-pressure phase transformations in nanostructured TiO_2 ceramics." In: *Scripta Materialia* 124 (2016), pp. 59–62. DOI: 10.1016/j.scriptamat.2016.06.022 (cit. on p. 2).

[15] W. Dmowski et al. "Structural rejuvenation in a bulk metallic glass induced by severe plastic deformation." In: *Acta Materialia* 58.2 (2010), pp. 429–438. DOI: 10.1016/j.actamat.2009.09.021 (cit. on pp. 2, 12).

[16] S.-h. Joo et al. "Work-Hardening Induced Tensile Ductility of Bulk Metallic Glasses via High-Pressure Torsion." In: *Scientific reports* 5 (2015), p. 9660. DOI: 10.1038/srep09660 (cit. on pp. 2, 12, 15).

[17] F. Meng et al. "Reversible transition of deformation mode by structural rejuvenation and relaxation in bulk metallic glass." In: *Applied Physics Letters* 101.12 (2012), p. 121914. DOI: 10.1063/1.4753998 (cit. on pp. 2, 12, 15, 18).

[18] Y. B. Wang et al. “Introducing a strain-hardening capability to improve the ductility of bulk metallic glasses via severe plastic deformation.” In: *Acta Materialia* 60.1 (2012), pp. 253–260. DOI: 10.1016/j.actamat.2011.09.026 (cit. on pp. 2, 12).

[19] J. Das et al. ““Work-Hardenable” Ductile Bulk Metallic Glass.” In: *Physical Review Letters* 94.20 (2005). DOI: 10.1103/physrevlett.94.205501 (cit. on p. 2).

[20] A. Hohenwarter et al. “Technical parameters affecting grain refinement by high pressure torsion.” In: *International Journal of Materials Research* 100.12 (2009), pp. 1653–1661. DOI: 10.3139/146.110224 (cit. on p. 5).

[21] L. Perrière and Y. Champion. “Phases distribution dependent strength in metallic glass – aluminium composites prepared by spark plasma sintering.” In: *Materials Science & Engineering A* 548 (2012), pp. 112–117. DOI: 10.1016/j.msea.2012.03.100 (cit. on p. 11).

[22] N. Ciftci et al. “Atomization and characterization of a glass forming alloy {(Fe0.6Co0.4)0.75B0.2Si0.05}96Nb4.” In: *Journal of Non-Crystalline Solids* 394-395 (2014), pp. 36–42. DOI: 10.1016/j.jnoncrysol.2014.03.023 (cit. on p. 11).

[23] X. D. Wang et al. “Atomic-level structural modifications induced by severe plastic shear deformation in bulk metallic glasses.” In: *Scripta Materialia* 64.1 (2011), pp. 81–84. DOI: 10.1016/j.scriptamat.2010.09.015 (cit. on pp. 12, 18).

[24] P. Denis et al. “Indenter size effect in high-pressure torsion deformed Pd-based metallic glass.” In: *International Journal of Materials Research* (2018). DOI: 10.3139/146.111627 (cit. on p. 12).

[25] X. Sauvage et al. “Structure and properties of a nanoscaled composition modulated metallic glass.” In: *Journal of Materials Science* 49.16 (2014), pp. 5640–5645. DOI: 10.1007/s10853-014-8279-z (cit. on p. 12).

[26] J. Sort et al. “Cold-consolidation of ball-milled Fe-based amorphous ribbons by high pressure torsion.” In: *Scripta Materialia* 50.9 (2004), pp. 1221–1225. DOI: 10.1016/j.scriptamat.2004.02.004 (cit. on p. 12).

[27] H. Asgharzadeh et al. “Consolidation of Cu-based amorphous alloy powders by high-pressure torsion.” In: *Journal of Materials Science* 50.8 (2015), pp. 3164–3174. DOI: 10.1007/s10853-015-8877-4 (cit. on p. 12).

[28] J. B. Fogagnolo et al. "Consolidation of easy glass former $Zr_{55}Cu_{30}Al_{10}Ni_5$ alloy ribbons by severe plastic deformation." In: *Journal of Metastable and Nanocrystalline Materials* 20-21 (2004), pp. 253–256. DOI: 10.4028/www.scientific.net/JMNM.20-21.253 (cit. on p. 12).

[29] E. V. Boltynjuk et al. "Enhanced strain rate sensitivity of Zr-based bulk metallic glasses subjected to high pressure torsion." In: *Journal of Alloys and Compounds* 747 (2018), pp. 595–602. DOI: 10.1016/j.jallcom.2018.03.018 (cit. on p. 12).

[30] S. V. Ketov et al. "Rejuvenation of metallic glasses by non-affine thermal strain." In: *Nature* 524.7564 (2015), pp. 200–203. DOI: 10.1038/nature14674 (cit. on pp. 15, 18).

[31] P. Murali and U. Ramamurty. "Embrittlement of a bulk metallic glass due to sub-T_g annealing." In: *Acta Materialia* 53.5 (2005), pp. 1467–1478. DOI: 10.1016/j.actamat.2004.11.040 (cit. on p. 18).

[32] Y. Q. Cheng and E. Ma. "Intrinsic shear strength of metallic glass." In: *Acta Materialia* 59.4 (2011), pp. 1800–1807. DOI: 10.1016/j.actamat.2010.11.046 (cit. on p. 18).

[33] D. V. Louzguine-Luzgin et al. "Influence of cyclic loading on the onset of failure in a Zr-based bulk metallic glass." In: *Journal of Materials Science* 49.19 (2014), pp. 6716–6721. DOI: 10.1007/s10853-014-8276-2 (cit. on p. 18).

[34] J. Pan et al. "Extreme rejuvenation and softening in a bulk metallic glass." In: *Nature Communications* 9.1 (2018). DOI: 10.1038/s41467-018-02943-4 (cit. on p. 18).

[35] J. Eckert et al. "Mechanical properties of bulk metallic glasses and composites." In: *Journal of Materials Research* 22.02 (2007), pp. 285–301. DOI: 10.1557/jmr.2007.0050 (cit. on p. 18).

[36] J. L. Cheng et al. "Correlation of the microstructure and mechanical properties of Zr-based in-situ bulk metallic glass matrix composites." In: *Intermetallics* 18.12 (2010), pp. 2425–2430. DOI: 10.1016/j.intermet.2010.08.040 (cit. on p. 18).

[37] C. C. Hays, C. P. Kim, and W. L. Johnson. "Microstructure controlled shear band pattern formation and enhanced plasticity of bulk metallic glasses containing in situ formed ductile phase dendrite dispersions." In: *Physical Review Letters* 84.13 (2000), pp. 2901–2904. DOI: 10.1103/PhysRevLett.84.2901 (cit. on p. 18).

[38] M. Heilmaier. "Deformation behavior of Zr-based metallic glasses." In: *Journal of Materials Processing Technology* 117.3 (2001), pp. 374–380. DOI: 10.1016/S0924-0136(01)00782-8 (cit. on p. 18).

[39] J. C. Qiao and J. M. Pelletier. "Crystallization kinetics in $Cu_{46}Zr_{45}Al_7Y_2$ bulk metallic glass by differential scanning calorimetry (DSC)." In: *Journal of Non-Crystalline Solids* 357.14 (2011). STRUCTURE OF NON-CRYSTALLINE MATERIALS 11 Proceedings of the 11th Conference on the Structure of Non-Crystalline Materials (NCM11) Paris, France June 28- July 2, 2010, pp. 2590–2594. DOI: 10.1016/j.jnoncrysol.2010.12.071 (cit. on p. 18).

[40] Y. Wu et al. "Formation of Cu-Zr-Al bulk metallic glass composites with improved tensile properties." In: *Acta Materialia* 59.8 (2011), pp. 2928–2936. DOI: 10.1016/j.actamat.2011.01.029 (cit. on p. 18).

[41] R. T. Ott et al. "Structure and properties of Zr–Ta–Cu–Ni–Al bulk metallic glasses and metallic glass matrix composites." In: *Journal of Non-Crystalline Solids* 317.1-2 (2003), pp. 158–163. DOI: 10.1016/s0022-3093(02)01996-8 (cit. on p. 18).

[42] H. Choi-Yim et al. "Synthesis and characterization of particulate reinforced $Zr_{57}Nb_5Al_{10}Cu_{15.4}Ni_{12.6}$ bulk metallic glass composites." In: *Acta Materialia* 47.8 (1999), pp. 2455–2462. DOI: 10.1016/s1359-6454(99)00103-2 (cit. on pp. 18, 39).

[43] R. D. Conner, R. B. Dandliker, and W. L. Johnson. "Mechanical properties of tungsten and steel fiber reinforced Zr41.25Ti13.75Cu12.5Ni10Be22.5 metallic glass matrix composites." In: *Acta Materialia* 46.17 (1998), pp. 6089–6102. DOI: 10.1016/S1359-6454(98)00275-4 (cit. on pp. 18, 39).

[44] S. T. Deng et al. "Metallic glass fiber-reinforced Zr-based bulk metallic glass." In: *Scripta Materialia* 64.1 (2011), pp. 85–88. DOI: 10.1016/j.scriptamat.2010.09.014 (cit. on pp. 18, 39).

[45] Y.-K. Xu et al. "Mg-based bulk metallic glass composites with plasticity and gigapascal strength." In: *Acta Materialia* 53.6 (2005), pp. 1857–1866. DOI: 10.1016/j.actamat.2004.12.036 (cit. on p. 18).

[46] T. Liu et al. "Synthesis and mechanical properties of TiC-reinforced Cu-based bulk metallic glass composites." In: *Scripta Materialia* 60.2 (2009), pp. 84–87. DOI: 10.1016/j.scriptamat.2008.09.004 (cit. on pp. 18, 39).

[47] H. Shakur Shahabi et al. "Metallic glass–steel composite with improved compressive plasticity." In: *Materials & Design* 59 (2014), pp. 241–245. DOI: 10.1016/j.matdes.2014.03.007 (cit. on pp. 18, 39).

[48] J. G. Lee et al. "Mechanical property and fracture behavior of strip cast Zr-base BMG alloy containing crystalline phase." In: *Intermetallics* 12.10-11 SPEC. ISS. (2004), pp. 1125–1131. DOI: 10.1016/j.intermet.2004.04.022 (cit. on pp. 18, 39).

[49] H. S. Wang, J. Y. Wu, and Y. T. Liu. "Effect of the volume fraction of the ex-situ reinforced Ta additions on the microstructure and properties of laser-welded Zr-based bulk metallic glass composites." In: *Intermetallics* 68 (2016), pp. 87–94. DOI: 10.1016/j.intermet.2015.09.007 (cit. on p. 18).

[50] N. Chen et al. "A nanoglass alloying immiscible Fe and Cu at the nanoscale." In: *Nanoscale* 7.15 (2015), pp. 6607–6611. DOI: 10.1039/c5nr01406a (cit. on p. 18).

[51] W. J. Wright, R. Saha, and W. D. Nix. "Deformation Mechanisms of the $Zr_{40}Ti_{14}Ni_{10}Cu_{12}Be_{24}$ Bulk Metallic Glass." In: *MATERIALS TRANSACTIONS* 42.4 (2001), pp. 642–649. DOI: 10.2320/matertrans.42.642 (cit. on p. 32).

[52] W. Liang et al. "Plastic deformation behaviors of Ni- and Zr-based bulk metallic glasses subjected to nanoindentation." In: *Materials Characterization* 86 (2013), pp. 290–295. DOI: 10.1016/j.matchar.2013.10.014 (cit. on p. 32).

[53] C. A. Schuh and T. G. Nieh. "A nanoindentation study of serrated flow in bulk metallic glasses." In: *Acta Materialia* 51.1 (2003), pp. 87–99. DOI: 10.1016/s1359-6454(02)00303-8 (cit. on p. 32).

[54] C. A. Schuh, A. C. Lund, and T. G. Nieh. "New regime of homogeneous flow in the deformation map of metallic glasses: elevated temperature nanoindentation experiments and mechanistic modeling." In: *Acta Materialia* 52.20 (2004), pp. 5879–5891. DOI: 10.1016/j.actamat.2004.09.005 (cit. on p. 32).

[55] L. Cheng et al. "Serrated flow behaviors of a Zr-based bulk metallic glass by nanoindentation." In: *Journal of Applied Physics* 115.8 (2014), p. 084907. DOI: 10.1063/1.4866874 (cit. on p. 32).

[56] T. Burgess, K. J. Laws, and M. Ferry. "Effect of loading rate on the serrated flow of a bulk metallic glass during nanoindentation." In: *Acta Materialia* 56.17 (2008), pp. 4829–4835. DOI: 10.1016/j.actamat.2008.05.039 (cit. on p. 32).

[57] F. Haag et al. "Influences of residual stresses on the serrated flow in bulk metallic glass under elastostatic four-point bending – A nanoindentation and atomic force microscopy study." In: *Acta Materialia* 70 (2014), pp. 188–197. DOI: 10.1016/j.actamat.2014.01.053 (cit. on p. 32).

[58] H. Huang et al. "Effects of pre-compression deformation on nanoindentation response of $Zr_{65}Cu_{15}Al_{10}Ni_{10}$ bulk metallic glass." In: *Journal of Alloys and Compounds* 674 (2016), pp. 223–228. DOI: 10.1016/j.jallcom.2016.03.057 (cit. on p. 32).

[59] C. Schuh, T. Hufnagel, and U. Ramamurty. "Mechanical behavior of amorphous alloys." In: *Acta Materialia* 55.12 (2007), pp. 4067–4109. DOI: 10.1016/j.actamat.2007.01.052 (cit. on p. 32).

[60] R. Limbach et al. "Serrated flow of CuZr-based bulk metallic glasses probed by nanoindentation: Role of the activation barrier, size and distribution of shear transformation zones." In: *Journal of Non-Crystalline Solids* 459 (2017), pp. 130–141. DOI: 10.1016/j.jnoncrysol.2017.01.015 (cit. on p. 32).

[61] I.-C. Choi et al. "Estimation of the shear transformation zone size in a bulk metallic glass through statistical analysis of the first pop-in stresses during spherical nanoindentation." In: *Scripta Materialia* 66.11 (2012), pp. 923–926. DOI: 10.1016/j.scriptamat.2012.02.032 (cit. on p. 32).

[62] J. P. Coleman et al. "Effect of annealing on nanoindentation slips in a bulk metallic glass." In: *Physical Review B* 96.13 (2017). DOI: 10.1103/physrevb.96.134117 (cit. on p. 32).

[63] B. Yang and T. Nieh. "Effect of the nanoindentation rate on the shear band formation in an Au-based bulk metallic glass." In: *Acta Materialia* 55.1 (2007), pp. 295–300. DOI: 10.1016/j.actamat.2006.08.028 (cit. on p. 32).

[64] J. M. Wheeler et al. "Activation parameters for deformation of ultrafine-grained aluminium as determined by indentation strain rate jumps at elevated temperature." In: *Materials Science and Engineering: A* 585 (2013), pp. 108–113. DOI: 10.1016/j.msea.2013.07.033 (cit. on p. 32).

[65] F. Spaepen. *Defects in amorphous metals*. Technical Report 16. Office of naval research, 1982 (cit. on p. 32).

[66] A. Leitner, V. Maier-Kiener, and D. Kiener. "Essential refinements of spherical nanoindentation protocols for the reliable determination of mechanical flow curves." In: *Materials & Design* 146 (2018), pp. 69–80. DOI: 10.1016/j.matdes.2018.03.003 (cit. on p. 33).

[67] C. A. Pampillo and A. C. Reimschuessel. "The fracture topography of metallic glasses." In: *Journal of Materials Science* 9.5 (1974), pp. 718–724. DOI: 10.1007/bf00761791 (cit. on p. 36).

[68] S. Pauly et al. "Microstructural heterogeneities governing the deformation of Cu47.5Zr47.5Al5 bulk metallic glass composites." In: *Acta Materialia* 57.18 (2009), pp. 5445–5453. DOI: 10.1016/j.actamat.2009.07.042 (cit. on p. 39).

[69] Y. Wu et al. "Designing Bulk Metallic Glass Composites with Enhanced Formability and Plasticity." In: *Journal of Materials Science & Technology* 30.6 (2014), pp. 566–575. DOI: 10.1016/j.jmst.2014.03.028 (cit. on p. 39).

[70] Y. Jiang et al. "Modeling of Metallic Glass Matrix Composites Under Compression: Microstructure Effect on Shear Band Evolution." In: *Metallurgical and Materials Transactions A* 49.1 (2017), pp. 417–424. DOI: 10.1007/s11661-017-4412-3 (cit. on p. 39).

[71] A. Donohue et al. "Suppression of the shear band instability during plastic flow of nanometer-scale confined metallic glasses." In: *Applied Physics Letters* 91.24 (2007), p. 241905. DOI: 10.1063/1.2821227 (cit. on p. 39).

[72] J.-Y. Kim et al. "Suppression of Catastrophic Failure in Metallic Glass-Polyisoprene Nanolaminate Containing Nanopillars." In: *Advanced Functional Materials* 22.9 (2012), pp. 1972–1980. DOI: 10.1002/adfm.201103050 (cit. on p. 39).

[73] M. C. Liu et al. "Superplastic-like deformation in metallic amorphous/crystalline nanolayered micropillars." In: *Intermetallics* 30 (2012), pp. 30–34. DOI: 10.1016/j.intermet.2012.03.037 (cit. on p. 39).

[74] T. G. Nieh and J. Wadsworth. "Bypassing shear band nucleation and ductilization of an amorphous–crystalline nanolaminate in tension." In: *Intermetallics* 16.9 (2008), pp. 1156–1159. DOI: 10.1016/j.intermet.2008.06.018 (cit. on p. 39).

[75] Y. Cui et al. "Plastic Deformation Modes of CuZr/Cu Multilayers." In: *Scientific Reports* 6.1 (2016). DOI: 10.1038/srep23306 (cit. on p. 39).

[76] W. Guo et al. "Intrinsic and extrinsic size effects in the deformation of amorphous CuZr/nanocrystalline Cu nanolaminates." In: *Acta Materialia* 80 (2014), pp. 94–106. DOI: 10.1016/j.actamat.2014.07.027 (cit. on p. 39).

[77] M. W. Kapp et al. "Anisotropic deformation characteristics of an ultrafine- and nanolamellar pearlitic steel." In: *Acta Materialia* 106 (2016), pp. 239–248. DOI: 10.1016/j.actamat.2015.12.037 (cit. on p. 39).

[78] G. B. Rathmayr, A. Bachmaier, and R. Pippan. "Development of a New Testing Procedure for Performing Tensile Tests on Specimens with Sub-Millimetre Dimensions." In: *Journal of Testing and Evaluation* 41.4 (2013), p. 20120175. DOI: 10.1520/jte20120175 (cit. on p. 42).

6. List of appended publications

Paper A
L. Krämer, K.S. Kormout, Y. Champion, D. Setman and R. Pippan
Production of Bulk Metallic Glasses by Severe Plastic Deformation
Metals 5.2 (2015): 720-729; doi:10.3390/met5020720

Paper B
L. Krämer, Y. Champion, and R. Pippan
From powders to bulk metallic glass composites
Scientific Reports 7 (2017): 6651; doi:10.1038/s41598-017-06424-4

Paper C
L. Krämer, Y. Champion, K.S. Kormout, V. Maier-Kiener and R. Pippan
Bulk metallic dual phase glasses by severe plastic deformation
Intermetallics 94 (2018): 172-178; https://doi.org/10.1016/j.intermet.2017.12.005

Paper D
L. Krämer, V. Maier-Kiener, Y. Champion, B. Sarac and R. Pippan
Activation volume and energy of bulk metallic glasses determined by nanoindentation
Submitted to Materials and Design

Paper E
L. Krämer, M. Kapp, M. Alfreider and R. Pippan
Micropillars compression testing of bulk metallic glass composites
Manuscript in preparation, will be submitted to a SCI journal

A. Production of Bulk Metallic Glasses by Severe Plastic Deformation

Lisa Krämer [1], Karoline S. Kormout [1], Daria Setman [2], Yannick Champion [3] and Reinhard Pippan [1,4]

[1] Erich Schmid Institute of Materials Science, Austrian Academy of Sciences
[2] Physics of Nanostructured Materials, Faculty of Physics, University of Vienna
[3] Institut de Chimie et des Matériaux Paris-Est, Université Paris-Est Créteil
[4] Department of Materials Physics, Montanuniversität Leoben

Abstract. The aim of this study was to show the possibility to produce bulk metallic glass with severe plastic deformation. High pressure torsion was used to consolidate Zr-based metallic glass powder and deform it further to weld the powder particles together. The produced samples were investigated with Scanning electron microscope (SEM), Transmission electron microscope (TEM), Differential scanning calorimetry (DSC) and X-ray diffraction (XRD) to check if the specimens are fully dense and have an amorphous structure. The results show that the specimens remain amorphous during high pressure torsion and the density depends on the applied strain. Additional Vickers hardness measurements enable a comparison with literature and show for Zr-based metallic glass powder typical values (approximately 500 HV).

A.1. Introduction

Metallic glasses are a new class of metals which were discovered in the 1950s [1–4]. As a consequence of their amorphous structure, they have no crystal defects

as grain boundaries or dislocations [2, 5, 6]. This microstructural state changes the mechanism of deformation and subsequently their mechanical properties. Their high yield strength and high elastic strain qualifies them for various applications [7, 8]. But as any new developed material they also harbor some obstacles. Metallic glasses are not easy to produce as crystallization of the melt must be prevented. This can be difficult depending on the used composition and the aimed large dimensions [9, 10]. A solution for producing bulk metallic glasses from not so stable metallic glass compositions is to produce metallic glass powder and form the bulk metallic glass in an additional step. Severe plastic deformation (SPD) can be this additional step [11, 12] as well as a powder metallurgy process [13–15]. SPD techniques were used in the past to obtain ultra-fine grained (ufg) and nanocrystalline (nc) specimens [16–19]. A wide range of materials was processed with SPD and even immiscible systems were deformed to obtain nanocomposites [20]. The flexibility of these routes is also shown in the used starting materials. Those can range from solid to powder and so the process of alloying is simplified. If High Pressure Torsion (HPT) is used, powders can simply be mixed and the achieved mixture consolidated. With the applied strain during the following HPT step the material becomes homogenous. SPD was already used to deform bulk metallic glass samples and even metal-metallic glass composites were obtained [21–25].
The aim of this study was to produce bulk metallic glass samples with SPD. The Zr-based metallic glass powder was consolidated and deformed with HPT. SEM, TEM, XRD, DSC and hardness measurements were used to investigate the specimen.

A.2. Experimental Section

For the production of bulk metallic glass samples a metallic glass powder with the composition $Zr_{57}Cu_{20}Al_{10}Ni_8Ti_5$ has been used. This powder was prepared by high pressure gas atomization and shows an average particle size of 25 µm [21]. SEM images of the bulk metallic glass powder can be seen in Figure A.1. A contamination particle is indicated with an arrow (see Figure A.1b). Energy dispersive X-ray spectroscopy (EDX) measurements have shown that contamination contains Mn, Si, Fe, Al and Mg. For the HPT process powder was filled between the gap of the grooved HPT anvils, where it was then compacted and processed

by torsion under a pressure of 8 GPa at room temperature up to 63 revolutions. The final dimensions of the samples used in this study are 6 mm in diameter and 0.6 mm in height.
Some contaminating particles were too hard to be deformed simultaneously with the metallic glass powder. They, however, do not seem to influence the results of the general microstructure (their total amount is below 1%); they may affect the ductility which is not in the focus of this paper.
The deformed HPT disks were cut into halves, ground and polished for SEM investigations and hardness measurements. The Vickers hardness was measured along the diameter in the cross section of the HPT sample with a load of 0.5 kg.
XRD phase analysis of the samples was performed using a 5-circle X-ray diffractometer (SmartLab from Rigaku Co., Tokyo, Japan) equipped with a source for Cu-Kα radiation.
DSC was performed using a Netzsch DSC 204. The heating range was between 25 and 590 °C. The heating rate was 10 K min^{-1}. For the DSC measurements undeformed powder and HPT samples, which were cut in half, were used.
TEM samples were prepared by a standard procedure: grinding, polishing and dimple grinding with subsequent ion milling. TEM micrographs were recorded in top view at a radius of 2 mm ($\pm$0.3 mm due to varying dimension and position of the hole). Microstructural investigations were conducted using a SEM LEO1525 and a (scanning) transmission electron microscope (S)TEM JEOL JEM 2100F equipped with a C_S-corrector.

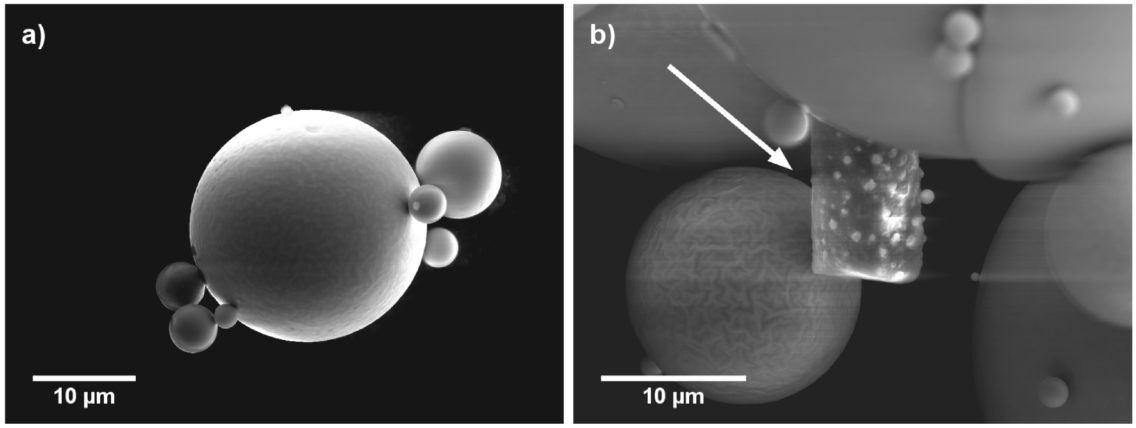

Figure A.1.: SEM images of the Zr-based metallic glass powder. The average particle size is 25 µm. The spherical shape (a) is a result of the production by high pressure gas atomization. Contaminating particle indicated with an arrow in (b).

A.3. Results and Discussion

This work studies the possibility to produce bulk metallic glass specimens by using HPT; starting with compaction of metallic glass powder and subsequent deformation. Therefore, three essential questions must be answered: Is the final sample fully dense or does the sample contain pores or cracks? Does the structure of the metallic glass change during deformation? Is the hardness of the HPT produced metallic glass comparable to values of bulk metallic glass in literature?

To answer the first question samples were investigated in the SEM to find (even very small) inhomogeneities. In HPT the torsion of the sample leads to a strain gradient along the radius of the sample. At the center the applied shear strain is nearly zero, but at the edge it increases linearly with the radius. Hence, only few HPT disks are sufficient to investigate the influence of the applied strain. The investigated sample was deformed for 30 rotations at room temperature and cut into halves. Figure A.2 and Figure A.3 show the center and the edge in the cross-section of the HPT disk with a shear strain of approximately 0 and 900, respectively.
In Figure A.2, crack-like defects can be seen. These cracks are not induced by deformation, they are a consequence of the insufficient deformation of the initial powder particles. The distance between these defects corresponds to the particle diameter; it is between 2 and 25 µm (see Figure A.1). Those cracks can be found up to a radius of approximately 1.5 mm, which equals to a shear strain of about

600. Apparently, the deformation near the center was not large enough to enforce a full consolidation of the powder and fully weld the particles together.

At the edge of the same specimen (Figure A.3), no cracks or pores can be detected. So, these SEM images confirm that full density is reached after sufficient deformation of the specimen. No other features are visible in the SEM images due to the absence of cracks, pores and boundaries.
XRD and DSC measurements as well as TEM imaging were used to investigate the microstructure of the HPT deformed specimen. In XRD broad peaks are expected for an amorphous material, while crystalline materials would show several sharp peaks depending on the crystal structure and the lattice parameters. The position of the metallic glass peak depends on the present short-range order, which is strongly influenced by the composition. In Figure A.4, the XRD results of the undeformed powder and a deformed specimen are presented. A broad peak typical for amorphous material can be seen for the HPT deformed sample (black line) and the undeformed powder (gray line). The position and width of the peaks are identical and this confirms that bulk metallic glass can be produced by HPT using metallic glass powder. For the used Zr-based metallic glass the broad peaks are in the same angle range as the peaks of crystalline Zr. Shifting of this angles is due to the other elements, such as Cu and Ni.

Additionally, the specimen was examined in TEM to confirm that the material is still amorphous after HPT deformation. In Figure A.5, a high resolution TEM image and the diffraction pattern for the same position are shown. In the TEM image no ordered region is visible. The diffraction pattern consists of two broad rings only, which indicates-analog to the XRD measurements-an amorphous state of the sample.

DSC measurements substantiate the results of XRD and TEM. Two HPT disks with 10 and 30 turns at room temperature and undeformed powder were measured and the results can be seen in Figure A.6. All three specimens crystallize at nearly the same temperature (460 °C, 457 °C and 455 °C) and the crystallization peaks have got a very similar breadth. Therefore, it can be concluded that during HPT deforming no crystallization occurs. The onset of crystallization differs for the deformed specimen and the undeformed powder. This is caused by structural relaxation during the deformation as the high compressive loading of the HPT favors a structural change to a state with higher density (which equals a more relaxed state) [26]. The relaxation in the HPT specimen causes also a shift of the

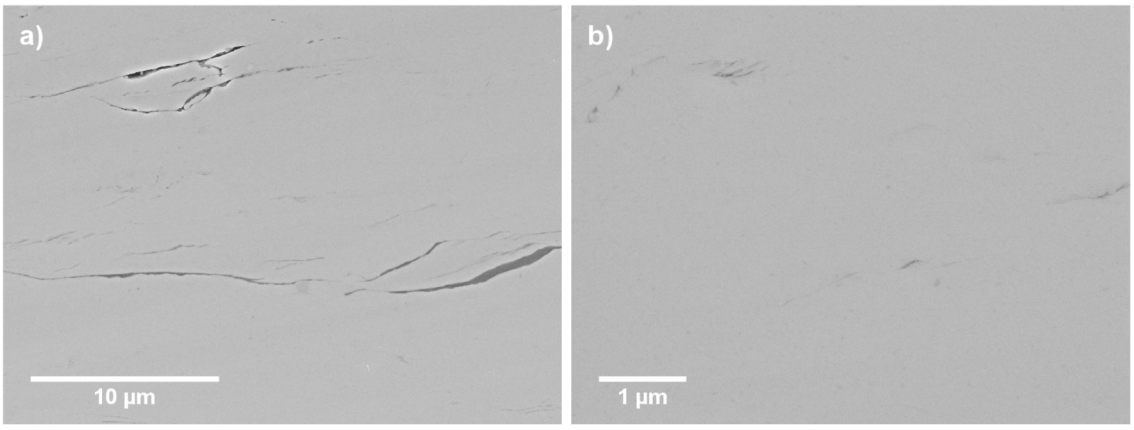

Figure A.2.: SEM images taken from regions near the center of the High Pressure Torsion (HPT) disk at different magnifications (lower magnification (**a**) and higher magnification (**b**). The crack-like defects are the result of unfinished welding of the metallic glass powder. The distance between the cracks correlates with the particle size of the powder.

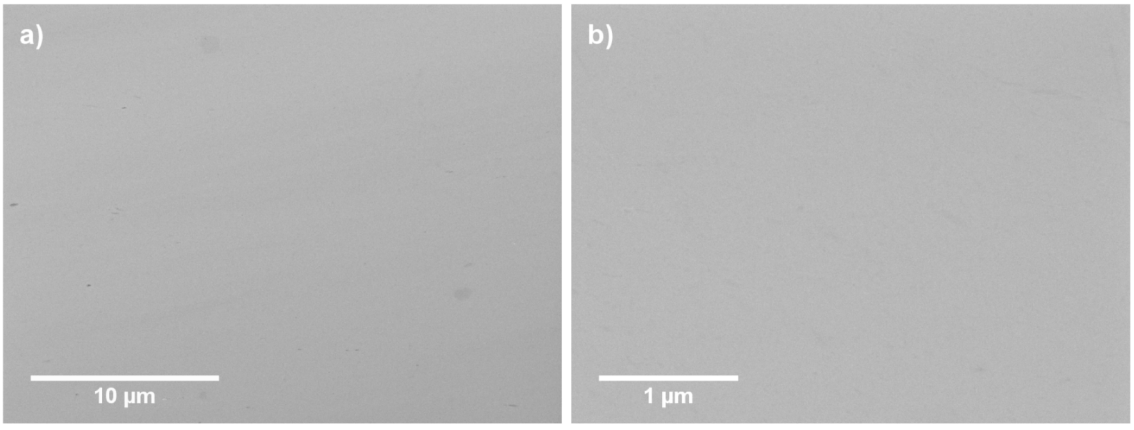

Figure A.3.: SEM images near the edge of the HPT disk. At low magnifications (**a**) and even at higher magnifications (**b**), no cracks, pores or other inhomogeneities can be detected.

glass transition temperature to higher temperatures and a stronger overlap with the crystallization peak.

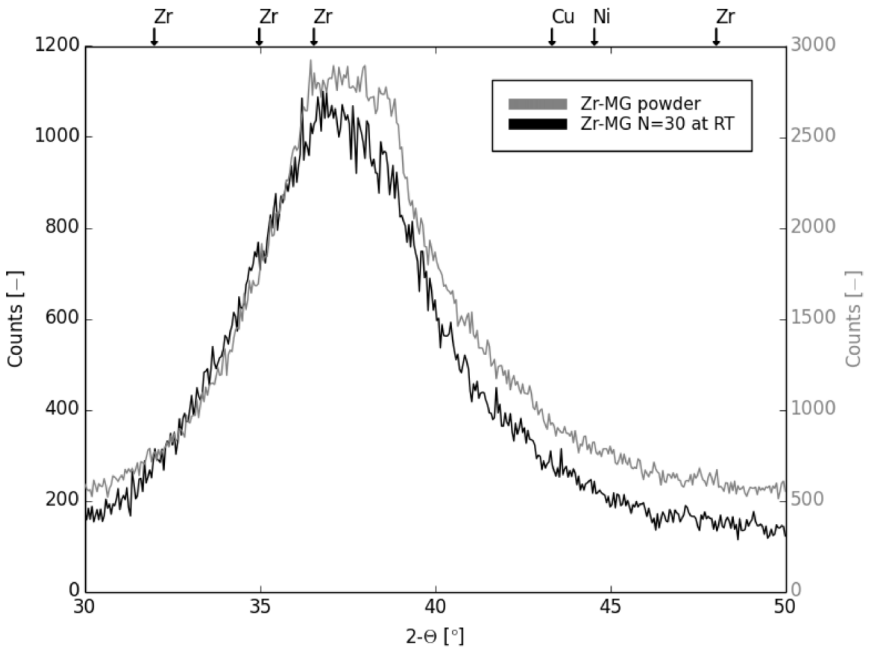

Figure A.4.: XRD measurement of the HPT deformed sample and the undeformed powder (gray line). The peak position and width are in both cases the same, which indicates an unchanged amorphous structure after HPT deformation. The arrows indicate the peak positions of crystalline Zr, Ni and Cu. The number of counts differs as different slits were used during the XRD measurements.

The Vickers hardness was measured to get information about the mechanical properties of the processed bulk metallic glass. In Figure A.7, the results are shown for three specimens, which were deformed at room temperature for three different numbers of rotations (10, 30 and 63 turns). After ten turns the specimen contains crack-like defects all over the diameter as the applied strain was not high enough to fully consolidate the powder. This leads to a decrease of hardness. Only near the edge, the hardness nearly approaches the value of the other samples. The hardness of the specimens with 30 and 63 turns is similar. Near the center a minimum hardness with about 450 HV is measured and at the edge it increases up to 500 HV. From the fact that the specimens with 30 and 63 rotation show nearly the same hardness it can be concluded that the hardness will not increase further more, even when additional deformation is applied. Hence, it is obvious that a saturation state is reached at the edge of the samples. The values of hardness for Zr-based glass in literature are in the range of

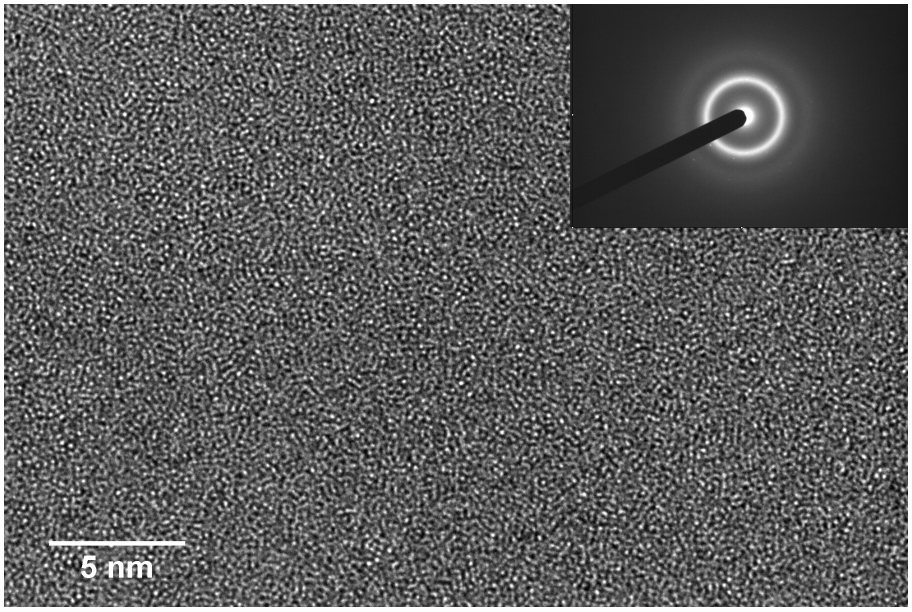

Figure A.5.: In the high resolution TEM image no ordered regions can be detected. The inset shows a diffraction pattern at the same position but from a much larger region selected area diffraction (SAD)aperture size: 120 µm). The broad rings confirm the amorphous state of the specimen.

420 −470 HV (Stolpe *et al.* [24]), 455 −475 HV (Luo *et al.* [27]), 480 HV (Champion and Perrière [28]) and 500 HV (Chen [29] and Xu *et al.* [30]). The variation in hardness seems to be caused by different compositions and production routes. Furthermore, one should take into account that HPT generated bulk metallic glass is heavily deformed.

The SEM micrographs indicate that HPT is a process capable to consolidate metallic glass powder by welding the particles together. In the past HPT has been already used to produce nanocomposites by co-deforming of two different materials. Hence, the next step is producing metallic glass composites. The second component next to a metallic glass can be a crystalline metal, but also another metallic glass. Mixing crystalline and amorphous metals together changes the deformation behavior and so, the formation of one fatal shear band can be prevented and the mechanical properties could be improved [21, 31, 32]. Metallic glass/metallic glass composites will also show different properties, because the two metallic glasses differ in the chemical composition and the near range ordering will vary. The interfaces between the two metallic glasses will strongly influence the properties of the composite.

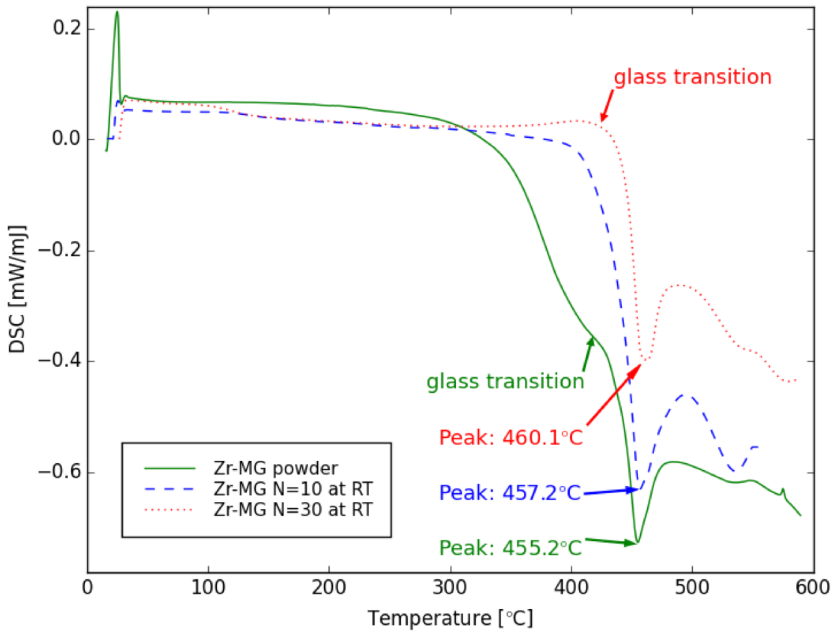

Figure A.6.: Differential scanning calorimetry (DSC) measurements exclude a crystallization during HPT deformation. The powder as well as the HPT disks show a distinctive crystallization peak at 457 °C, 455 °C and 460 °C, respectively. The peak breadth and position are nearly the same, which indicates an amorphous structure for all. The difference in the onset of crystallization and in the transition temperature is caused by structural relaxation due to the HPT process.

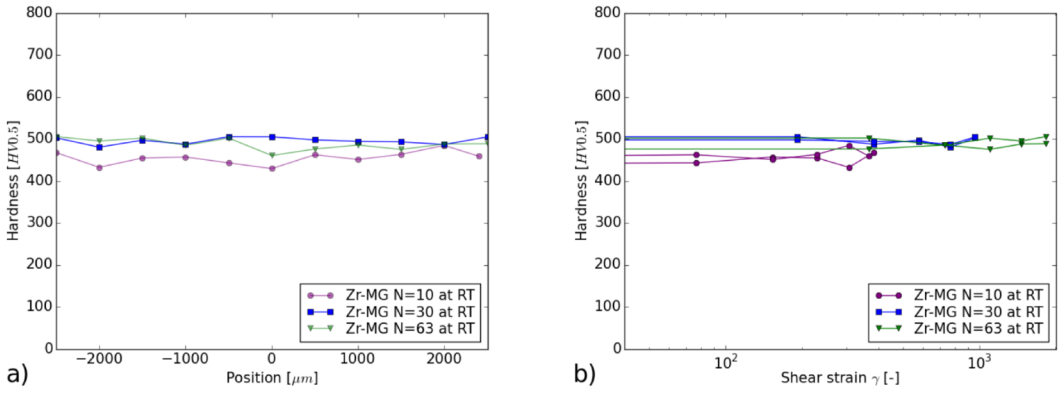

Figure A.7.: The results of Vickers hardness measurements can be seen. The hardness depending on the radius (**a**) of the HPT disk is shown as well as the hardness depending on the shear strain (**b**). Specimens with a higher number of applied rotations, show higher shear strain. For the sample with 10 turns the lowest hardness was measured. This is a result of incomplete welding of the powder and therefore crack-like defects. The specimens with 30 and 63 rotations show a similar hardness, which indicates that an equilibrium state is reached.

A.4. Conclusions

(i) Bulk metallic glass specimens can be produced by consolidation and deforming metallic glass powder with HPT; (ii) fully dense samples without cracks and pores can be achieved as long as sufficient strain (γ = 600) is applied to weld the powder particles; the necessary strain is significantly larger than in the case of consolidation of metal powder, due to the more localized deformation in metallic glasses; (iii) during HPT at room temperature no crystallization of the Zr-based metallic glass was observed, the specimens were found to be fully amorphous; (iv) a hardness of up to 500 HV is measured.

With this processing route it is possible to create new materials such as metal/metallic glass composites and metallic glass/metallic glass composites (two different metallic glasses). Those materials are expected to show interesting properties as the new interfaces will change dramatically the properties of metallic glasses.

Acknowledgments

Funding for this work has been provided by the European Research Council under ERC Grant Agreement No. 340185 USMS and by the Austrian Science Fund (FWF) under Project: T512-20.

Author Contributions

Lisa Krämer processed the samples, did the SEM and XRD investigations, carried out the hardness measurements and created the initial draft. Karoline Kormout carried out high resolution TEM imaging and recorded diffraction patterns. Daria Setman characterized the material with DSC measurements. Yannick Champion provided the metallic powder. Reinhard Pippan formulated the idea of this work. All authors discussed the results, contributed ideas, participated in the manuscript preparation and approved the final manuscript.

Conflicts of Interest

The authors declare no conflict of interest.

A.5. References

[1] A. L. Greer. "Metallic glasses... on the threshold." In: *Materials Today* 12.1-2 (2009), pp. 14–22. DOI: 10.1016/S1369-7021(09)70037-9 (cit. on p. 61).

[2] J. F. Löffler. "Bulk metallic glasses." In: *Intermetallics* 11.6 (2003), pp. 529–540. DOI: 10.1016/S0966-9795(03)00046-3 (cit. on pp. 61, 62).

[3] M. F. Ashby and A. L. Greer. "Metallic glasses as structural materials." In: *Scripta Materialia* 54.3 (2006), pp. 321–326. DOI: 10.1016/j.scriptamat.2005.09.051 (cit. on p. 61).

[4] W. H. Wang, C. Dong, and C. H. Shek. "Bulk metallic glasses." In: *Materials Science and Engineering: R: Reports* 44.2-3 (2004), pp. 45–89. DOI: 10.1016/j.mser.2004.03.001 (cit. on p. 61).

[5] C. E. Packard and C. A. Schuh. "Initiation of shear bands near a stress concentration in metallic glass." In: *Acta Materialia* 55.16 (2007), pp. 5348–5358. DOI: 10.1016/j.actamat.2007.05.054 (cit. on p. 62).

[6] X. J. Liu et al. "Metallic liquids and glasses: Atomic order and global packing." In: *Physical Review Letters* 105.15 (2010), pp. 1–4. DOI: 10.1103/PhysRevLett.105.155501 (cit. on p. 62).

[7] J. Schroers et al. "Bulk metallic glasses for biomedical applications." In: *JOM* 61.9 (2009), pp. 21–29. DOI: 10.1007/s11837-009-0128-1 (cit. on p. 62).

[8] A. Inoue, X. M. Wang, and W. Zhang. "Developments and Applications of Bulk Metallic Glasses." In: *Reviews on advanced materials science* 18.1 (2008), pp. 1–9. DOI: 10.1007/978-0-387-48921-6_1 (cit. on p. 62).

[9] Z. P. Lu and C. T. Liu. "A new glass-forming ability criterion for bulk metallic glasses." In: *Acta Materialia* 50.13 (2002), pp. 3501–3512. DOI: 10.1016/S1359-6454(02)00166-0 (cit. on p. 62).

[10] Y. Li et al. "Formation of Bulk Metallic Glasses and Their Composites." In: *MRS Bulletin* 32.08 (2007), pp. 624–628. DOI: 10.1557/mrs2007.123 (cit. on p. 62).

[11] A. Azushima et al. "Severe plastic deformation (SPD) processes for metals." In: *CIRP Annals* 57.2 (2008), pp. 716–735. DOI: 10.1016/j.cirp.2008.09.005 (cit. on p. 62).

[12] L. Krämer, S. Wurster, and R. Pippan. "Deformation behavior of Cu-composites processed by HPT." In: *IOP Conference Series: Materials Science and Engineering*. Vol. 63. 1. 2014. DOI: 10.1088/1757-899X/63/1/012026 (cit. on p. 62).

[13] S. Nowak et al. "Approach of the spark plasma sintering mechanism in $Zr_{57}Cu_{20}Al_{10}Ni_8Ti_5$ metallic glass." In: *Journal of Alloys and Compounds* 509.3 (2011), pp. 1011–1019. DOI: 10.1016/j.jallcom.2010.09.158 (cit. on p. 62).

[14] G. Xie et al. "Nearly full density $Ni_{52.5}Nb_{10}Zr_{15}Ti_{15}Pt_{7.5}$ bulk metallic glass obtained by spark plasma sintering of gas atomized powders." In: *Applied Physics Letters* 90.24 (2007), pp. 12–15. DOI: 10.1063/1.2748102 (cit. on p. 62).

[15] G. Q. Xie et al. "Ceramic particulate reinforced $Zr_{55}Cu_{30}Al_{10}Ni_5$ metallic glassy matrix composite fabricated by spark plasma sintering." In: *Materials Transactions* 48.7 (2007), pp. 1600–1604. DOI: 10.2320/matertrans.MJ200716 (cit. on p. 62).

[16] R. Z. Valiev, R. K. Islamgaliev, and I. V. Alexandrov. "Bulk nanostructured materials from severe plastic deformation." In: *Progress in Materials Science* 45.2 (2000), pp. 103–189. DOI: 10.1016/S0079-6425(99)00007-9 (cit. on p. 62).

[17] R. Z. Valiev et al. "Producing Bulk Ultrafine-Grained Materials by Severe Plastic Deformation: Ten Years Later." In: *JOM* 68.4 (2006), pp. 1216–1226. DOI: 10.1007/s11837-016-1820-6 (cit. on p. 62).

[18] Y. Estrin and A. Vinogradov. "Extreme grain refinement by severe plastic deformation: A wealth of challenging science." In: *Acta Materialia* 61.3 (2013), pp. 782–817. DOI: 10.1016/j.actamat.2012.10.038 (cit. on p. 62).

[19] I. Sabirov and R. Pippan. "Formation of a W-25%Cu nanocomposite during high pressure torsion." In: *Scripta Materialia* 52.12 (2005), pp. 1293–1298. DOI: 10.1016/j.scriptamat.2005.02.017 (cit. on p. 62).

[20] A. Bachmaier and R. Pippan. "Generation of metallic nanocomposites by severe plastic deformation." In: *International Materials Reviews* 58.1 (2013), pp. 41–62. DOI: 10.1179/1743280412Y.0000000003 (cit. on p. 62).

[21] X. Sauvage et al. "Structure and properties of a nanoscaled composition modulated metallic glass." In: *Journal of Materials Science* 49.16 (2014), pp. 5640–5645. DOI: 10.1007/s10853-014-8279-z (cit. on pp. 62, 68).

[22] J. Sort et al. "Cold-consolidation of ball-milled Fe-based amorphous ribbons by high pressure torsion." In: *Scripta Materialia* 50.9 (2004), pp. 1221–1225. DOI: 10.1016/j.scriptamat.2004.02.004 (cit. on p. 62).

[23] N. Van Steenberge et al. "Effects of severe plastic deformation on the structure and thermo-mechanical properties of $Zr_{55}Cu_{30}Al_{10}Ni_5$ bulk metallic glass." In: *Journal of Alloys and Compounds* 500.1 (2010), pp. 61–67. DOI: 10.1016/j.jallcom.2010.03.195 (cit. on p. 62).

[24] M. Stolpe, J. J. Kruzic, and R. Busch. "Evolution of shear bands, free volume and hardness during cold rolling of a Zr-based bulk metallic glass." In: *Acta Materialia* 64 (2014), pp. 231–240. DOI: 10.1016/j.actamat.2013.10.035 (cit. on pp. 62, 68).

[25] H. Shakur Shahabi et al. "Metallic glass–steel composite with improved compressive plasticity." In: *Materials & Design* 59 (2014), pp. 241–245. DOI: 10.1016/j.matdes.2014.03.007 (cit. on p. 62).

[26] A. Concustell et al. "Structural relaxation and rejuvenation in a metallic glass induced by shot-peening." In: *Philosophical Magazine Letters* 89.12 (2009), pp. 831–840. DOI: 10.1080/09500830903337919 (cit. on p. 65).

[27] K. Luo et al. "Changes of hardness and electronic work function of $Zr_{41.2}Ti_{13.8}Cu_{12.5}Ni_{10}Be_{22.5}$ bulk metallic glass on annealing." In: *Philosophical Magazine Letters* 91.4 (2011), pp. 237–245. DOI: 10.1080/09500839.2010.539989 (cit. on p. 68).

[28] L. Perrière and Y. Champion. "Phases distribution dependent strength in metallic glass – aluminium composites prepared by spark plasma sintering." In: *Materials Science & Engineering A* 548 (2012), pp. 112–117. DOI: 10.1016/j.msea.2012.03.100 (cit. on p. 68).

[29] X. Chen. "Structure and hardness evolution of the scale of a Zr-based metallic glass during oxidation." In: *Journal of Non-Crystalline Solids* 362.1 (2013), pp. 140–146. DOI: 10.1016/j.jnoncrysol.2012.11.018 (cit. on p. 68).

[30] Y. Xu et al. "Enhanced thermal stability and hardness of $Zr_{46}Cu_{39.2}Ag_{7.8}Al_7$ bulk metallic glass with Fe addition." In: *Materials Science and Engineering: A* 527.6 (2010), pp. 1444–1447. DOI: 10.1016/j.msea.2009.10.029 (cit. on p. 68).

[31] A. Inoue, H. Kimura, and K. Sasamori. "High-strength $Al_{94}(V,Ti)_4Fe_2$ alloys consisting of nanogranular amorphous and fcc-Al phases." In: *Nanostructured Materials* 9.1-8 (1997), pp. 493–496. DOI: 10.1016/S0965-9773(97)00108-6 (cit. on p. 68).

[32] D. C. Hofmann. "Bulk Metallic Glasses and Their Composites: A Brief History of Diverging Fields." In: *Journal of Materials* 2013 (2013), pp. 1–8. DOI: 10.1155/2013/517904 (cit. on p. 68).

B. From powders to bulk metallic glass composites

Lisa Krämer [1], **Yannick Champion** [2] **and Reinhard Pippan** [1]
[1] Erich Schmid Institute of materials science, Austrian Academy of Science, Leoben, Austria
[2] Univ. Grenoble Alpes, CNRS, Grenoble INP, SIMaP, F-38000 Grenoble France

Abstract. One way to adjust the properties of materials is by changing its microstructure. This concept is not easily applicable on bulk metallic glasses (BMGs), because they do not consist of grains or different phases and so their microstructure is very homogeneous. One obvious way to integrate inhomogeneities is to produce bulk metallic glass composites (BMGCs). Here we show how to generate BMGCs via high-pressure torsion (HPT) starting from powders (amorphous Zr-MG and crystalline Cu). Using this approach, the composition can be varied and by changing the applied shear strains, the refinement of the microstructure is adjustable. This process permits to produce amorphous/crystalline composites where the scale of the phases can be varied from the micro- to the nanometer regime. Even mixing of the two phases and the generation of new metallic glasses can be achieved. The refinement of microstructure increases the hardness and a hardness higher than the initial BMG can be obtained.Microstructural changes are used to adjust the properties of the materials. This concept is not easily applicable on bulk metallic glasses (BMGs), because they do not consist of grains or different phases and so their microstructure is very homogeneous. One obvious way to integrate inhomogeneities is to produce bulk metallic glass composites (BMGCs). Here we show how to generate BMGCs via high-pressure torsion (HPT) starting from powders (amorphous Zr-MG and crystalline Cu). Using this approach, the composition can be varied and by changing the applied shear strains, the refinement of the microstructure is adjustable. This process permits to produce amorphous/crystalline composites where the scale of the

phases can be varied from the micro- to the nanometer regime. Even mixing of the two phases and the generation of new metallic glasses can be achieved. The refinement of microstructure increases the hardness and a hardness higher than the initial BMG can be obtained.

B.1. Introduction

Bulk metallic glasses (BMGs) have advantages over crystalline metals including high hardness, high elastic energy storage and high corrosion resistivity, but have also some major drawbacks. BMGs are relatively brittle and especially show poor ductility in tensile testing [1]. Changing the microstructure is a common way to tune properties of materials. It was shown for BMGs that changing the local short range order through rejuvenation by thermal or mechanical cycling will influence mechanical properties [2–4]. Another way is to produce composites containing an additional amorphous or crystalline phase [5]. One prominent route is to partly crystallize the amorphous sample by either choosing a slower cooling rate, another composition or reheating the BMG up to the crystallization temperature [6–11]. Other routes are casting the BMG with crystalline parts as springs, tubes, particles or wires [12–17] or using warm extrusion of a mixture of powders [18]. Drawbacks of these strategies are the inhomogeneous microstructure and sometimes the brittle crystalline phase [19, 20]. Another idea is to use powder metallurgy and sintering to fabricate bulk metallic glass composites (BMGCs) and despite problems with porosity, promising results have been published [21–23]. For producing crystalline composites, also severe plastic deformation (SPD) has been used in the past [24, 25]. Even though many different SPD techniques (equal channel angular extrusion, accumulative roll bonding and many others) have been developed, high pressure torsion (HPT) is used for this work because it has some major advantages especially for research. The applied strain can be easily varied by changing the number of rotations; many commonly brittle materials can be deformed due to its high nearly hydrostatic pressure and even powders are possible as initial material. By using powders, a wider range of compositions become feasible compared to conventional casting. Super saturated solid solutions are producible and unfavorable phases can be avoided [26–30]. HPT was already used on MGs, on one hand to change the properties of BMGs by structural rejuvenation [3, 4, 31–34] and on the other hand to fabricate

BMGs and BMGCs [35–44]. Zr-MG powder was compacted and deformed via HPT beforehand. It could be shown that fully dense and amorphous specimens without cracks and pores can be fabricated with sufficient applied strains and no crystallization occurred during the HPT process [45].
The aim of this study is to show that new types of BMGCs can be produced via SPD. Questions addressed are: what are the obtainable limits of the metal-metallic glass composites in scale and content, and how far can we extend the field of bulk metallic glasses. The initial materials are powders (Zr-MG and crystalline Cu) that were mixed and then consolidated, welded together and refined by HPT. Four different compositions (Zr-MG Xwt% Cu, X=20, 40, 60, 80) were produced as well as single phase Zr-MG samples as reference. To investigate the influence of the degree of deformation and the ratio of the two phases on the evolution of the microstructure and mechanical properties, scanning electron microscopy (SEM), X-ray diffraction (XRD) and hardness measurements were used.

B.2. Microstructural evolution as a function of strain

In Fig. B.1a, the microstructure of Zr-MG 20wt% Cu as a function of the applied strain is presented (the shear direction is indicated with an arrow). All micrographs are backscatter-detector images to distinguish easily between Cu and the Zr-based MG. Images in the lower row have a significant higher magnification. The two phases in the coarse state differ in their mechanical properties, which strongly influences the deformation. In the beginning, Cu sustains most of the deformation as it has a lower hardness and yield strength. Zr-MG is more difficult to deform and the initial particles are easily distinguished as they change their initial shape and size only marginally (one of those particle is marked with a white arrow in Fig. B.1a). Cu works as a glue and holds the amorphous particles together. Due to the heavy plastic deformation, its grain size is refined down to the range of several hundreds of nanometers. Higher strains (see micrographs for $\gamma = 50$) force the Zr-MG to deform and bond together. Therefore, the amorphous phase forms long elongated regions with a length of about 100 µm in the shear direction and widths up to 10 µm, where some features from the initial particles are still detectable (area marked by the black arrow). The Cu bands become thinner and more evenly distributed, but large Cu-containing areas can still be found. The Cu grains refine and become less than 100 nm in size. Micrographs at

$\gamma = 80$ show a further refinement of the microstructure. Cu and Zr-MG lamellae decrease in length and in width: All of the Cu lamellas are thinner than 1 µm and most of them exhibit a thickness of 20 nm. Cu grains are not detectable in the SEM micrographs anymore, but the thickness of the thinner lamellas can be seen as an upper limit for the grain size in this bands. The elongated regions of the amorphous phase shrinks below 100 µm in length and 10 µm in width. From $\gamma = 80$ to $\gamma = 165$ a pronounced increase of the number of the thin Zr-MG lamellas occurs, so that the Cu network in the images at low magnification, is in reality a Cu rich region consisting of Cu lamellas with lengths below 1 µm and widths below 100 nm separated by about equally sized amorphous lamellas. Additionally, the boundaries between the two phases change from sharp and easily detectable to more blurry interfaces as the Cu starts to mix with the amorphous phase at higher strains. This process starts already at $\gamma = 80$, but is clearly recognizable at $\gamma = 165$. The mixing of the two phases progresses with increasing applied deformation. At $\gamma = 250$ elongated Cu rich and Zr-MG rich regions can still be detected with smooth transitions in between, but at $\gamma = 390$ Cu the SEM micrographs seems to show a single phase metallic glass.
The ratio of the amorphous and crystalline phase can be easily modified by varying the ratio of the two initial powders. To investigate the influence of the ratio of the two phases, compositions with higher contents of Cu were produced and SEM micrographs of the cross sections of samples with 40 wt% Cu at different applied strains are shown in Fig. B.1b. At first glance the major difference visible in the composition with less Cu in Fig. B.1a, is the higher amount of the crystalline phase, but the deformation mechanism does not differ. The softer Cu phase starts to deform first, but with higher amount of applied strain, the harder Zr-MG starts to form long elongated bands, which shrink with increasing deformation. At higher strains, the two phases start to mix again until a homogeneous material is formed. However, by comparing the micrographs for the two compositions, it can be clearly seen that a higher content of Cu requires a higher strains to reach the same refinement of the microstructure. To obtain the saturation microstructure (i.e. the monolithic metallic glass), the applied strain for Zr-MG 40wt% Cu has to be doubled compared to the Zr-MG 20wt% Cu.
The content of Cu was further increased to investigate the limits of mixing and to see any resulting change of the deformation behavior. In Fig. B.1c, SEM micrographs of Zr-MG 60wt% Cu can be seen. Compared to the samples with 20 and 40 wt% Cu, the deformation behavior in the beginning does not change and

a lamellar structure is formed (see $\gamma = 550 - 1600$). At higher applied strains ($\gamma = 3300 - 5000$), the micrographs exhibits a deviation from the deformation behavior from the samples with low Cu content. The lamellas shrink in thickness with higher applied strain, but mainly a break-down of the lamellar configuration occurs. A transition microstructure develops with residual lamellar blocks embedded (see circled areas in Fig. B.1c) in a nanocrystalline (see black arrow) and amorphous structure (see white arrow). At $\gamma = 11000$, both phases seem to be fully mixed and a single phase microstructure is obtained. The amount of strain needed to reach this saturation microstructure is about 10 times higher than for Zr-MG 40wt% Cu and about 20 times higher than for Zr-MG 20wt% Cu. The composition with the highest Cu content investigated was Zr-MG 80wt% Cu. SEM micrographs of the cross sections are displayed in Fig. B.2. Again, the Zr-MG particles elongate and a lamellar structure is obtained in the beginning, but at an applied strain of $\gamma = 5000$ and higher, the lamellas start to break and the microstructure does not change significantly anymore even after applying extremely high strains (up to $\gamma = 18900$). Since the microstructure does not change significantly even after this enormous increase of the applied strain, it is assumed that a saturation is reached. The saturation microstructure seems to consist of a nanocrystalline Cu-rich matrix (in Fig. B.2 at higher magnification crystals indicated with black arrows can be seen as small freckles in the light grey area) in which elongated Zr-MG bands (some are indicated with a white arrow in Fig. B.2) with a length of several micrometers are embedded.
The evolution of the microstructure is reflected also in XRD measurements. XRD profiles of samples from Zr-MG (undeformed and deformed), crystalline Cu, and the four compositions investigated in a near saturated condition are displayed in Fig. B.3. The measured range is concentrated on the first (and strongest) peak of Zr-MG, which is very broad and has low intensity compared to the more distinctive peaks of crystalline Cu. The XRD results of a HPT deformed pure Cu powder are also depicted in Fig. B.3, which has a grain size of about 100 nm [24]. The XRD peaks of the undeformed and deformed Zr-MG coincide exactly, which indicates that the HPT process does not have an influence on the single phase BMG. The influence of the applied strain can be clearly seen at the three samples of Zr-MG 60wt% Cu as the number of rotations in the HPT process was varied from 50 to 200 and 500. The two Cu-peaks are very dominant for the specimen with 50 rotations, but shrink as the applied strain increases. After 200 rotations, the first Cu peak has a similar height as the amorphous peak and both Cu peaks

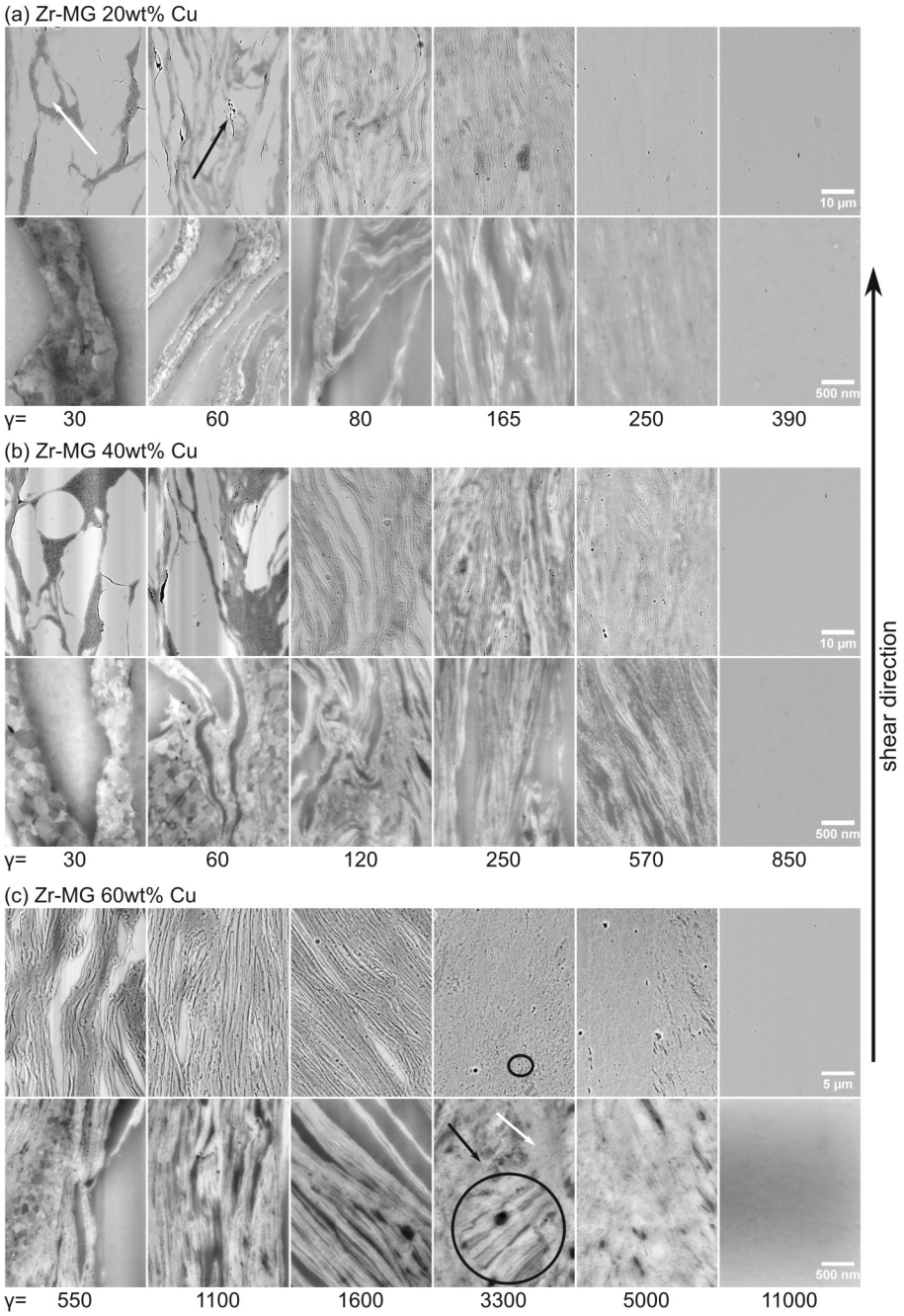

Figure B.1.: Illustration of SEM micrographs of (a) Zr-MG 20wt% Cu, (b) Zr-MG 40wt% Cu, and (c) Zr-MG 60wt% Cu. The top and bottom row of micrographs are taken at different magnifications. The evolution of the microstructure can be seen in dependence of the applied strain. The deformation increases from the left to the right and the microstructure changes from Zr-MG particles glued together by crystalline Cu to a lamellar structure. These lamellae refine with increasing applied strain until a complete mixing of the two phases occurs. Take notice in the increase of applied strain as higher contents of Cu.

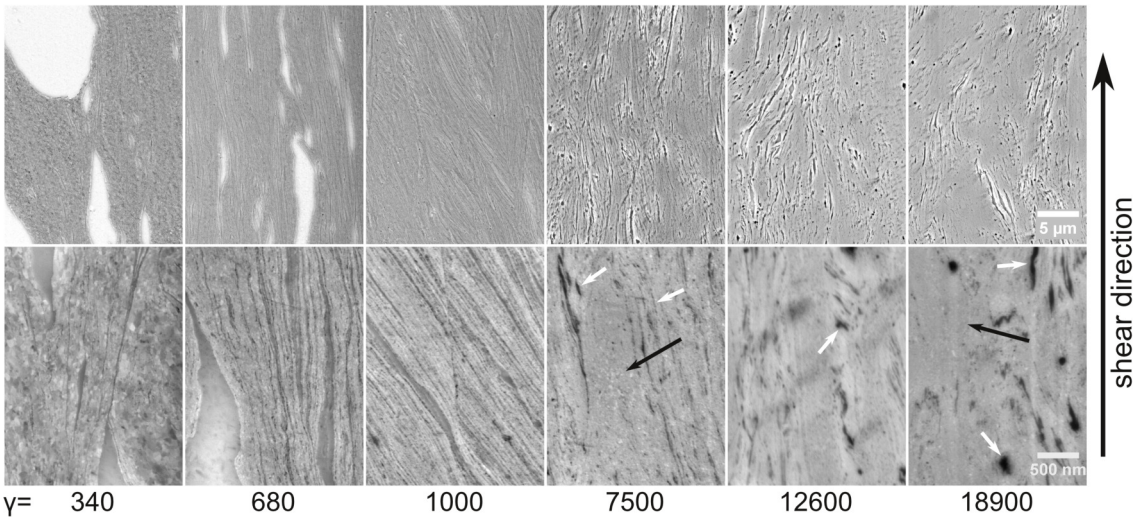

Figure B.2.: Illustration of SEM micrographs of Zr-MG 80wt% Cu. The amount of the softer phase (Cu) is too high to fully mix the two phases and Zr-MG bands and crystalline Cu rich regions characterize the microstructure. Even after $\gamma = 18900$, the microstructure does not significantly change and it is assumed that a saturation is reached.

broadened significantly, which can be caused by two effects: smaller crystal sizes and higher defect densities in the crystals. The crystalline peaks disappear after 500 rotations and only the amorphous peak remains.
For the other Cu concentrations, only one sample with a microstructure near the saturation is shown. This saturation is reached after different degrees of deformation. For Zr-MG 40wt% Cu and Zr-MG 20wt% Cu, 50 rotations are nearly sufficient to achieve a fully amorphous sample and only a minor peak indicates remaining crystalline Cu (indicated with arrows in Fig. B.3). On the other hand, even after 500 rotations Zr-MG 80wt% Cu shows a dominant Cu peak and a very weak amorphous peak (indicated with an arrow in Fig. B.3). Comparing the crystalline peak of Zr-MG 60wt% Cu and Zr-MG 80wt% Cu to the pure Cu sample, the Cu peak is shifted to lower angles due to partial solution (or formation of a supersaturated solid solution) and broadens mainly due to the small crystalline size. Furthermore, mixing Cu into the amorphous phase shifts its peak positions to higher 2-Theta values and the difference between Zr-MG and Zr-MG 60wt% Cu is approximately 5°. In order to demonstrate the possibility of analyzing the alloying region for generation of new metallic glasses, a sample with Zr-MG 20wt% Cu 10wt% Ni was investigated and after 150 rotations a fully amorphous structure is obtained.

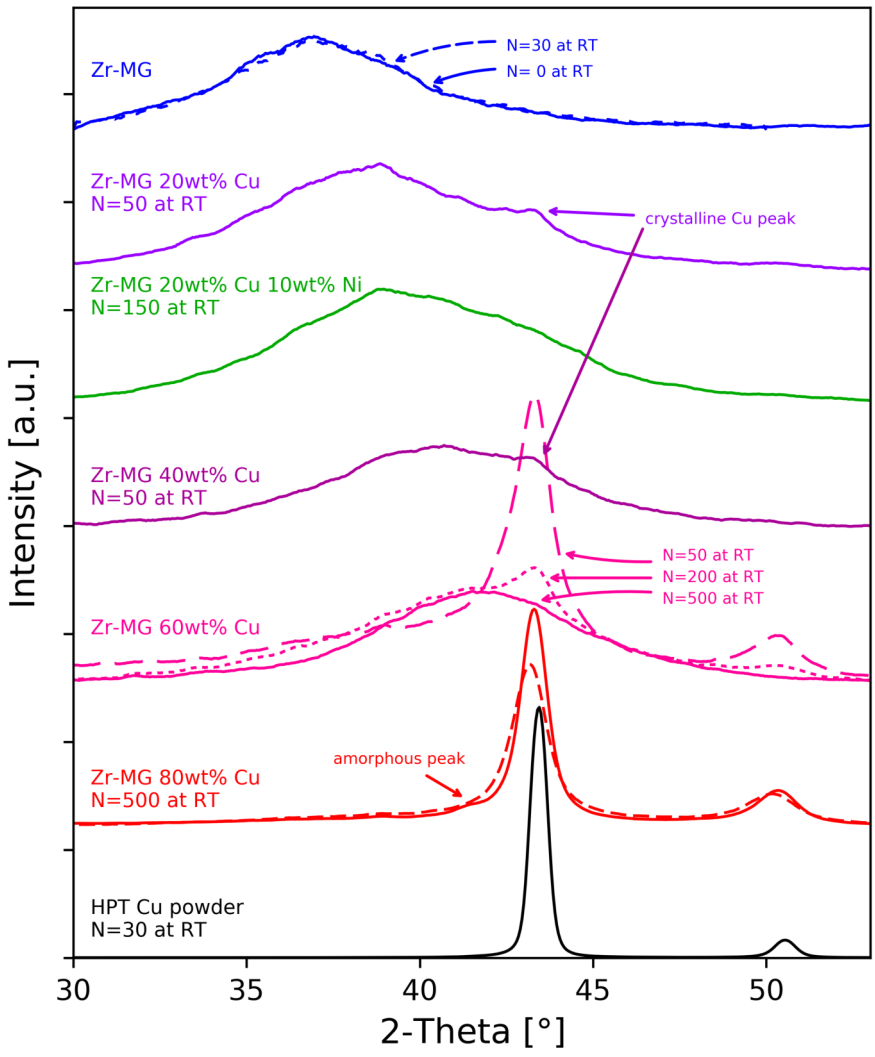

Figure B.3.: XRD results of different composite concentrations. After sufficient deformation, all compositions except Zr-MG 80wt% Cu show on broad amorphous peak. For Zr-MG 60wt% Cu, the evolution of the peaks with higher numbers of rotations is indicated: The dominant Cu peak shrinks with increasing strains until only the amorphous peak remains after 500 rotations. The amorphous peak shifts to larger angles with higher Cu content.

B.3. Impact on the mechanical properties

Microstructure influences strongly the mechanical properties, which were investigated in this study by using hardness measurement. In Fig. B.4, the Vicker's hardness is plotted versus the applied strain (see methods). Since the strain varies over about three orders of magnitudes, several specimens have been used. The fitted lines are for guiding the eye. The hardness of the single phase Zr-MG scatters strongly at low applied strain, because the particles are not welded together completely in this early state of deformation. To eliminate an effect from the HPT deformation on the hardness beside consolidation, undeformed powder and a Zr-MG sample with 30 rotations were investigated via nanoindentation. Both conditions show the same hardness with 6.12 ± 0.33 GPa for the powder and 6.11 ± 0.07 GPa for the deformed specimen. The influence of the applied strain is more pronounced for the BMGCs, because not only the particles are welded together but also a refining and mixing of the two phases occur. Three compositions (with 20, 40 and 60 wt% Cu) show a similar behavior. At low strains, the hardness is lower than the single phase Zr-MG but increases strongly with deformation. The slope decreases with higher deformation and the curves level off at a hardness higher than the Zr-MG. Exceeding the hardness of both initial powders can only be explained by mixing the two phases, shifting the chemical composition and so forming a new metallic glass with higher hardness. Higher contents of Cu shift the curve to the right, which means that welding, refining and mixing require more strain if the fraction of the softer phase is higher. This behavior of the hardness corresponds to the evolution of the microstructure where the influence of Cu can also be seen clearly by comparing micrographs of the different composition. Increasing the content of Cu in the amorphous phase also leads to higher hardness (see Zr-MG 20wt% Cu and Zr-MG 40wt% Cu), but it requires more deformation. Zr-MG 80wt% Cu also show an increase in hardness with larger applied strains, but the slope is less steep compared to the other compositions and the hardness of Zr-MG is not reached even after $\gamma = 104$. The material gets harder, but the rate is so slow that a real mixing (as it is the case for the other three compositions) is not practical, as days are needed to achieve sufficient deformation. Not only the shape and position of the hardness curves depend on the composition, but also the hardness at saturation. In Fig. B.5, the approximated hardness for the saturated microstructure depending on the composition is shown and the highest value is reached for the composition with

40 wt% Cu (which corresponds to 32at% Zr and 55.1at% Cu). The hardness drops by approximately 15% for Zr-MG compared to Zr-MG 40 wt% Cu.

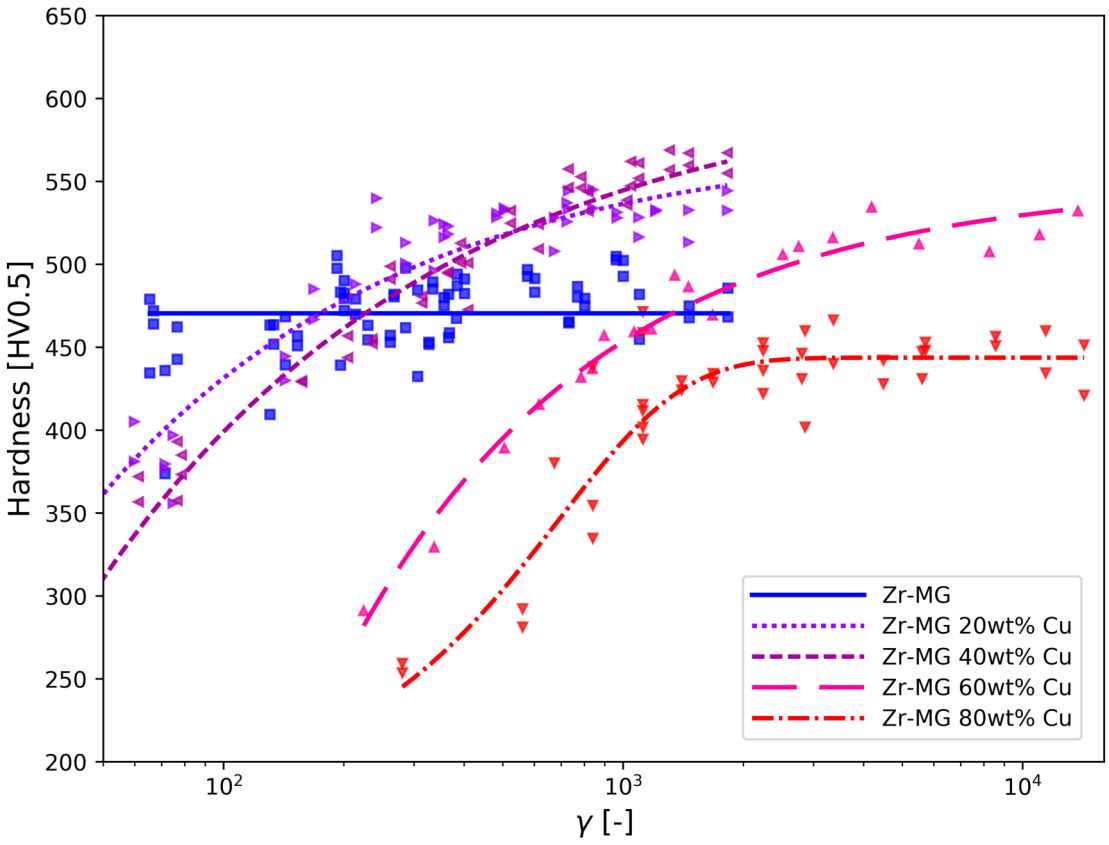

Figure B.4.: Illustration of Vicker's hardness evolution as a function of the shear strain of all compositions and Zr-BMG. The hardness of Zr-MG is constant over the applied strain, but the hardness of all compositions increases with increasing strains. In the case of Zr-MG 80wt% Cu, the hardness does not reach the hardness of Zr-MG, but all other compositions become harder than the two initial materials. The shape of the curve depends on the composition, higher contents of Cu shifts the curve to higher strains.

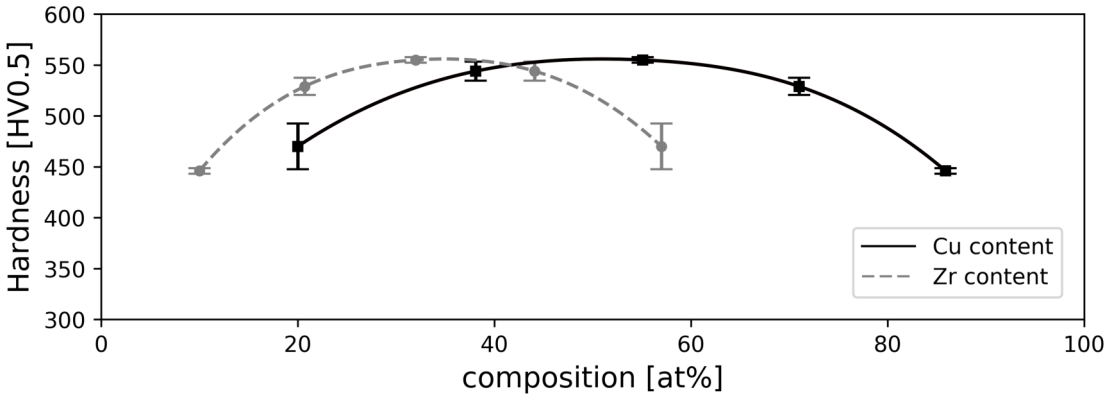

Figure B.5.: Approximated hardness at saturation for all compositions. The highest hardness can be found for the sample with 40wt% Cu (32at% Zr and 55.1at% Cu).

B.4. Discussion

The microstructure of the HPT deformed Cu + Zr-MG mixture and their mechanical properties depend strongly on the composition and on the applied strain. At low strains, a bulk composite is formed, in which the elongated phases start to refine and the hardness increases strongly. Increasing the applied strain, continuous thinning of the lamellae can be found for 20 and 40 wt% of Cu, whereas, the lamellas tend to break down at higher contents of Cu. For 60 and 80 wt% Cu, the length of the lamellae decreases more than their thickness. Additional, a mixing of the two phases takes place and at very high strains, a single phase BMG is obtained for all composition except Zr-MG 80wt% Cu. However, compared to the beginning the microstructure changes slower as the applied strain increases, which is also reflected in the hardness curves as all level off at higher degrees of deformation. The strain necessary to reach saturation increases significantly with increasing content of the softer crystalline phase (e.g.: more than 20 times if the content of Cu is increased from 20 wt% to 60 wt%). This can be seen in SEM, XRD and the hardness measurements (more Cu also shifts the hardness curves to higher strains). The position of the amorphous peak shifts to higher degrees as more Cu is mixed into the MG (the peak position of Zr-MG and Zr-MG 60wt% Cu differs with approximately 5°), but it can also been shown how the crystalline Cu in the composites is affected. As the applied strain increases, the crystalline peak broadens due to grain refinement. The grain size becomes smaller during HPT deformation in the presence of a second phase than in a single phase crystalline material. Mixing of the two phases takes place also for

Zr-MG 80wt% Cu. In this case, a part of Zr-MG is dissolved in the crystalline Cu, it remains crystalline (nanocrystalline) and a supersaturated solid solution is formed. The exact quantity is hard to obtain, because the Zr-MG contains four other elements beside Cu (if only Zr was considered, the peak shift would indicate dissolving 0.16 at% into the crystalline Cu [46]46). Two effects could simultaneously prevent a full mixing of the two phases for this composition: The solubility of Cu in the amorphous phase is restricted and the limit lies between 71at% (Zr-MG 60wt% Cu) and 85.9at% (Zr-MG 80wt% Cu). Secondly, the amorphous particles are not forced to deform as strongly as in the other compositions, because the high content of soft Cu carries all of the deformation. The consequences of the second effect is the possibility of a further mixing of the two phases if the applied strain is pushed to higher values. However, this can only happen if the emerging amorphous phase has a higher strength and forces the initial MG to deform further. Comparing the approximated hardness at saturation, it can be seen that all compositions show a higher hardening than Zr-MG 80wt% Cu. The highest value is obtained for Zr-MG 40wt% Cu. Zr-MG 80wt% CuCu still consists considerably of a crystalline phase but has already a similar hardness to Zr-MG. Nevertheless, the composition can be continuously changed in a range from $Zr_{57}Cu_{20}Al_{10}Ni_8Ti_5$ (Zr-MG) to at least $Zr_{20}Cu_{71}Al_{3.6}Ni_{2.9}Ti_{1.8}$ (Zr-MG 60wt% Cu). Additional to the compositions in this study, a fully amorphous sample with Zr-MG 20 wt% Cu 10 wt% Ni was produced. Compared to compositions from literature [37, 47–60], the adjustable range is large (see Fig. B.6) and new BMGs with a significant different chemical composition can be produced. Hence, the HPT can be used to fathom the limits of possible BMG's chemical compositions.In summary, it is shown that BMGCs can be produced via HPT and their microstructure and mechanical properties can be adjusted by changing composition and the applied strain. The BMGCs can be forced to mix and the solubility range is highly extended, producing new BMGs. The chemical composition of this new BMGs can be adjusted over a wider range compared to conventional casting and by adding additional elements (e.g. Cu and Ni), the possibility of feasible BMG compositions increases drastically. Changing the composition influences also the mechanical properties and the hardness can be increased by approximately 15%. While the generation of new BMGs is important, even more interesting is the potential for tuning the properties of metal-BMG composites with the possibility to vary the second phase. The second phase can be freely changed in choosing different materials and compositions and its

dimensions can be altered from the micrometer to the nanometer regime.

The microstructure of the HPT deformed Cu + Zr-MG mixture and their mechanical properties depend strongly on the composition and on the applied strain. At low strains, a bulk composite is formed, in which the elongated phases start to refine and the hardness increases strongly. Increasing the applied strain, continuous thinning of the lamellae can be found for 20 and 40wt% of Cu, whereas, the lamellas tend to break down at higher contents of Cu. For 60 and 80wt% Cu, the length of the lamellae decreases more than their thickness. Additional, a mixing of the two phases takes place and at very high strains, a single phase BMG is obtained for all composition but Zr-MG 80wt% Cu. However, compared to the beginning the microstructure changes slower as the applied strain increases, which is also reflected in the hardness curves as all level off at higher degrees of deformation. The strain necessary to reach saturation increases significantly with increasing content of the softer crystalline phase (e.g.: more than 20 times if the content of Cu is increased from 20wt% to 60wt%). This can be seen in SEM, XRD and the hardness measurements (more Cu also shifts the hardness curves to higher strains). The position of the amorphous peak shifts to higher degrees as more Cu is mixed into the MG (the peak position of Zr-MG and Zr-MG 60wt% Cu differs with approximately 5°), but it can also been shown how the crystalline Cu in the composites is affected. As the applied strain increases, the crystalline peak broadens due to grain refinement. The grain size during HPT deformation in the presence of a second phase than in a single phase crystalline material. Mixing of the two phases takes place also for Zr-MG 80wt% Cu. In this case, a part of Zr-MG is dissolved in the crystalline Cu, it remains crystalline (nanocrystalline) and a supersaturated solid solution is formed. The exact quantity is hard to obtain, because the Zr MG contains four other elements beside Cu (if only Zr was considered, the peak shift would indicate dissolving 0.16at% into the crystalline Cu [46]). Two effects could simultaneously prevent a full mixing of the two phases in this composition: The solubility of Cu in the amorphous phase is restricted and the limit lies between 71at% (Zr-MG 60wt% Cu) and 85.9at% (Zr-MG 80wt% Cu). Secondly, the amorphous particles are not forced to deform as strongly as in the other compositions, because the high content of soft Cu carries all of the deformation. The consequences of the second effect is the possibility of a further mixing of the two phases if the applied strain is pushed to higher values. However, this can only happen if the emerging amorphous phase has a higher strength and forces the initial MG to

deform further. Comparing the approximated hardness at saturation, it can be seen that all other compositions show a higher hardening. The highest value is obtained for Zr-MG 40wt% Cu. Zr-MG 80wt% Cu still consists considerably of a crystalline phase but has already a similar hardness to Zr-MG. Nevertheless, the composition can be continuously changed in a range from $Zr_{57}Cu_{20}Al_{10}Ni_8Ti_5$ (Zr-MG) to at least $Zr_{20}Cu_{71}Al_{3.6}Ni_{2.9}Ti_{1.8}$ (Zr-MG 60wt% Cu). Additional to the compositions in this study, a fully amorphous sample with Zr-MG 20wt% Cu 10wt% Ni was produced. Compared to compositions from literature [37, 47–60], the adjustable range is large (see Fig. B.6) and new BMGs with a total different chemical composition can be produced.
In summary, it is shown that BMGCs can be produced via HPT and their microstructure and mechanical properties can be adjusted by changing composition and the applied strain. The BMGCs can be forced to mix and the solubility range is highly extended, producing new BMGs. The chemical composition of this new BMGs can be adjusted over a wider range compared to conventional casting and by adding additional elements (e.g. Cu and Ni), the possibility of feasible BMG compositions increases drastically. Changing the composition influences also the mechanical properties and the hardness can be increased by approximately 15%. While the generation of new BMGs is important, even more interesting is the potential for tuning the properties of metal-BMG composites with the possibility to vary the second phase. The second phase can be freely changed in choosing different materials and compositions and its dimensions can be altered from the micrometer to the nanometer regime.

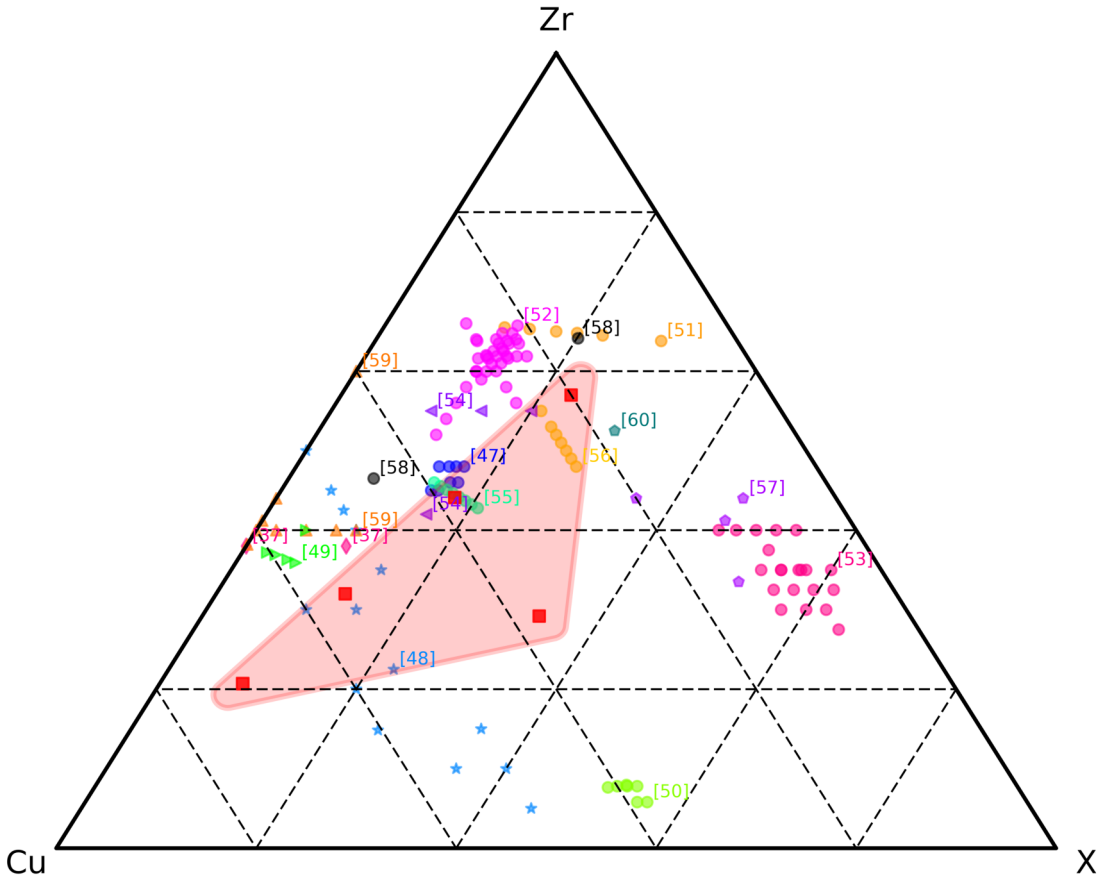

Figure B.6.: Chemical composition of BMGs from this study and literature are shown 37, 47–60 . All elements except Cu and Zr are summed up in X to enable a comparison. In this study, the chemical composition is changed by dissolving Cu into the Zr-MG and the range is marked. An additional composition with Zr-MG 20 wt% Cu 10 wt% Ni is added to show the extensive range of possible compositions.

B.5. Methods

The metallic glass powder ($Zr_{57}Cu_{20}Al_{10}Ni_8Ti_5$, spherical particle with diameters between 1 µm to 40 µm) was fabricated via high pressure gas atomization and was then mixed with crystalline Cu powder (spherical particle with diameters between 10 µm to 40 µm) in the respective compositions and blended by hand. The powder mixture was then filled into the gap between two grooved anvils and compacted by applying 4 GPa and 10° rotation in the HPT. For further deformation, the pressure was increased to 8 GPa (or 9 GPa) and samples with 2 to 500 rotations at room temperature were produced. The dimensions of the specimens were 6 mm in diameter and a height of approximately 450 µm to 600 µm. The applied shear strain γ can be estimated with

$$\gamma = \frac{2\pi N r}{t} \tag{B.1}$$

where r is the radius, N is the numbers of rotations and t is the thickness after deformation. As the dimensions were approximately the same for all samples, the degree of deformation is adjusted by the numbers of applied rotations (more turns lead to higher deformation) and at the radius where the sample was investigated (the applied strain increases with the radial distance from the center of the disk). For SEM and hardness measurement, the coin-like HPT samples were cut in half, ground and polished to investigate the cross sections. In SEM the back-scatter detector was used to provide mass contrast so that the two phases are more easily distinguishable. Vickers hardness was measured along the diameter on the cross section with a load of 0.5 kg. An error of 2% for the measured hardness values is assumed and the standard deviation errors of the fitted curve were calculated and used for the error bars for Fig. B.5. For nanoindentation testing of the powder and the deformed sample, a platform nanoindenter G200 (Keysight Tec) was used and the experiments were conducted under constant indentation strain rate ($0.05\,s^{-1}$) to a maximum indentation depth of 500 nm. The hardness was measured continuously over indentation depth and was averaged between an indentation depth between 400 nm to 450 nm. The non-deformed powder was embedded and then mechanical ground and polished like the surface of the deformed sample. Several particles were indented and for both materials, a mean value and the standard deviation were calculated from all indentations. A 5-circle X-ray diffractometer equipped with a source

for Cu-Kα radiation was used for XRD phase analysis of the specimens. Half samples were used and the surface was grounded to remove any impurities from the HPT process. The investigated 2-Theta range was concentrated around the first amorphous peak (the strongest).

Acknowledgments

The European Research Council under ERC Grant Agreement No. 3401 85 USMS has provided funding for this work.

Author contributions

Yannick Champion provided the metallic glass powder. Lisa Krämer produced the samples and performed the measurements. Reinhard Pippan formulated the idea of this work. All authors discussed the results, contributed ideas, participated in the manuscript preparation and approved the final manuscript.

B.6. References

[1] H. L. Gao, Y. Shen, and J. Xu. "Weibull analysis of fracture strength for $Zr_{55}Ti_2Co_{28}Al_{15}$ bulk metallic glass: Tension-compression asymmetry and porosity effect." In: *Journal of Materials Research* 26.16 (2011), pp. 2087–2097. DOI: 10.1557/jmr.2011.210 (cit. on p. 76).

[2] D. V. Louzguine-Luzgin et al. "Influence of cyclic loading on the onset of failure in a Zr-based bulk metallic glass." In: *Journal of Materials Science* 49.19 (2014), pp. 6716–6721. DOI: 10.1007/s10853-014-8276-2 (cit. on p. 76).

[3] F. Meng et al. "Reversible transition of deformation mode by structural rejuvenation and relaxation in bulk metallic glass." In: *Applied Physics Letters* 101.12 (2012), p. 121914. DOI: 10.1063/1.4753998 (cit. on p. 76).

[4] X. D. Wang et al. "Atomic-level structural modifications induced by severe plastic shear deformation in bulk metallic glasses." In: *Scripta Materialia* 64.1 (2011), pp. 81–84. DOI: 10.1016/j.scriptamat.2010.09.015 (cit. on p. 76).

[5] J. Eckert et al. "Mechanical properties of bulk metallic glasses and composites." In: *Journal of Materials Research* 22.02 (2007), pp. 285–301. DOI: 10.1557/jmr.2007.0050 (cit. on p. 76).

[6] J. L. Cheng et al. "Correlation of the microstructure and mechanical properties of Zr-based in-situ bulk metallic glass matrix composites." In: *Intermetallics* 18.12 (2010), pp. 2425–2430. DOI: 10.1016/j.intermet.2010.08.040 (cit. on p. 76).

[7] C. C. Hays, C. P. Kim, and W. L. Johnson. "Microstructure controlled shear band pattern formation and enhanced plasticity of bulk metallic glasses containing in situ formed ductile phase dendrite dispersions." In: *Physical Review Letters* 84.13 (2000), pp. 2901–2904. DOI: 10.1103/PhysRevLett.84.2901 (cit. on p. 76).

[8] M. Heilmaier. "Deformation behavior of Zr-based metallic glasses." In: *Journal of Materials Processing Technology* 117.3 (2001), pp. 374–380. DOI: 10.1016/S0924-0136(01)00782-8 (cit. on p. 76).

[9] J. C. Qiao and J. M. Pelletier. "Crystallization kinetics in $Cu_{46}Zr_{45}Al_7Y_2$ bulk metallic glass by differential scanning calorimetry (DSC)." In: *Journal of Non-Crystalline Solids* 357.14 (2011). STRUCTURE OF NON-CRYSTALLINE MATERIALS 11 Proceedings of the 11th Conference on the Structure of Non-Crystalline Materials (NCM11) Paris, France June 28- July 2, 2010, pp. 2590–2594. DOI: 10.1016/j.jnoncrysol.2010.12.071 (cit. on p. 76).

[10] Y. Wu et al. "Formation of Cu-Zr-Al bulk metallic glass composites with improved tensile properties." In: *Acta Materialia* 59.8 (2011), pp. 2928–2936. DOI: 10.1016/j.actamat.2011.01.029 (cit. on p. 76).

[11] R. T. Ott et al. "Structure and properties of Zr–Ta–Cu–Ni–Al bulk metallic glasses and metallic glass matrix composites." In: *Journal of Non-Crystalline Solids* 317.1-2 (2003), pp. 158–163. DOI: 10.1016/s0022-3093(02)01996-8 (cit. on p. 76).

[12] S. T. Deng et al. "Metallic glass fiber-reinforced Zr-based bulk metallic glass." In: *Scripta Materialia* 64.1 (2011), pp. 85–88. DOI: 10.1016/j.scriptamat.2010.09.014 (cit. on p. 76).

[13] H. Shakur Shahabi et al. "Metallic glass–steel composite with improved compressive plasticity." In: *Materials & Design* 59 (2014), pp. 241–245. DOI: 10.1016/j.matdes.2014.03.007 (cit. on p. 76).

[14] R. D. Conner, R. B. Dandliker, and W. L. Johnson. "Mechanical properties of tungsten and steel fiber reinforced Zr41.25Ti13.75Cu12.5Ni10Be22.5 metallic glass matrix composites." In: *Acta Materialia* 46.17 (1998), pp. 6089–6102. DOI: 10.1016/S1359-6454(98)00275-4 (cit. on p. 76).

[15] T. Liu et al. "Synthesis and mechanical properties of TiC-reinforced Cu-based bulk metallic glass composites." In: *Scripta Materialia* 60.2 (2009), pp. 84–87. DOI: 10.1016/j.scriptamat.2008.09.004 (cit. on p. 76).

[16] H. Choi-Yim et al. "Synthesis and characterization of particulate reinforced $Zr_{57}Nb_5Al_{10}Cu_{15.4}Ni_{12.6}$ bulk metallic glass composites." In: *Acta Materialia* 47.8 (1999), pp. 2455–2462. DOI: 10.1016/s1359-6454(99)00103-2 (cit. on p. 76).

[17] Y.-K. Xu et al. "Mg-based bulk metallic glass composites with plasticity and gigapascal strength." In: *Acta Materialia* 53.6 (2005), pp. 1857–1866. DOI: 10.1016/j.actamat.2004.12.036 (cit. on p. 76).

[18] K. Wang et al. "Interface structure and properties of a brass-reinforced $Ni_{59}Zr_{20}Ti_{16}Si_2Sn_3$ bulk metallic glass composite." In: *Acta Materialia* 56.13 (2008), pp. 3077–3087. DOI: 10.1016/j.actamat.2008.02.047 (cit. on p. 76).

[19] J. G. Lee et al. "Mechanical property and fracture behavior of strip cast Zr-base BMG alloy containing crystalline phase." In: *Intermetallics* 12.10-11 SPEC. ISS. (2004), pp. 1125–1131. DOI: 10.1016/j.intermet.2004.04.022 (cit. on p. 76).

[20] H. S. Wang, J. Y. Wu, and Y. T. Liu. "Effect of the volume fraction of the ex-situ reinforced Ta additions on the microstructure and properties of laser-welded Zr-based bulk metallic glass composites." In: *Intermetallics* 68 (2016), pp. 87–94. DOI: 10.1016/j.intermet.2015.09.007 (cit. on p. 76).

[21] D. J. Wang, X. S. Wei, and J. Shen. "Diamond reinforced Al-based bulk metallic glassy composites with improved plasticity fabricated by cold hydro-mechanical pressing." In: *Journal of Alloys and Compounds* 578 (2013), pp. 267–271. DOI: 10.1016/j.jallcom.2013.06.025 (cit. on p. 76).

[22] J. P. Kelly et al. "Designing in situ and ex situ bulk metallic glass composites via spark plasma sintering in the super cooled liquid state." In: *Materials & Design* 93 (2016), pp. 26–38. DOI: 10.1016/j.matdes.2015.12.130 (cit. on p. 76).

[23] L. Perrière and Y. Champion. "Phases distribution dependent strength in metallic glass – aluminium composites prepared by spark plasma sintering." In: *Materials Science & Engineering A* 548 (2012), pp. 112–117. DOI: 10.1016/j.msea.2012.03.100 (cit. on p. 76).

[24] R. Z. Valiev, R. K. Islamgaliev, and I. V. Alexandrov. "Bulk nanostructured materials from severe plastic deformation." In: *Progress in Materials Science* 45.2 (2000), pp. 103–189. DOI: 10.1016/S0079-6425(99)00007-9 (cit. on pp. 76, 79).

[25] Y. Estrin and A. Vinogradov. "Extreme grain refinement by severe plastic deformation: A wealth of challenging science." In: *Acta Materialia* 61.3 (2013), pp. 782–817. DOI: 10.1016/j.actamat.2012.10.038 (cit. on p. 76).

[26] K. S. Kormout, B. Yang, and R. Pippan. "Deformation Behavior and Microstructural Evolution of Cu-Ag Alloys Processed by High-Pressure Torsion." In: *Advanced Engineering Materials* 17.12 (2015), pp. 1828–1834. DOI: 10.1002/adem.201500109 (cit. on p. 76).

[27] A. Bachmaier et al. "Supersaturation in Ag–Ni alloy by two-step high-pressure torsion processing." In: *Philosophical Magazine Letters* 94.1 (2014), pp. 9–17. DOI: 10.1080/09500839.2013.852284 (cit. on p. 76).

[28] K. S. Kormout, R. Pippan, and A. Bachmaier. "Deformation-Induced Supersaturation in Immiscible Material Systems during High-Pressure Torsion." In: *Advanced Engineering Materials* 19.4 (2016), p. 1600675. DOI: 10.1002/adem.201600675 (cit. on p. 76).

[29] K. Edalati et al. "Plastic Deformation of $BaTiO_3$ Ceramics by High-pressure Torsion and Changes in Phase Transformations, Optical and Dielectric Properties." In: *Materials Research Letters* 3.4 (2015), pp. 216–221. DOI: 10.1080/21663831.2015.1065454 (cit. on p. 76).

[30] H. Razavi-Khosroshahi et al. "Plastic strain and grain size effect on high-pressure phase transformations in nanostructured TiO_2 ceramics." In: *Scripta Materialia* 124 (2016), pp. 59–62. DOI: 10.1016/j.scriptamat.2016.06.022 (cit. on p. 76).

[31] Y. B. Wang et al. "Introducing a strain-hardening capability to improve the ductility of bulk metallic glasses via severe plastic deformation." In: *Acta Materialia* 60.1 (2012), pp. 253–260. DOI: 10.1016/j.actamat.2011.09.026 (cit. on p. 76).

[32] S.-h. Joo et al. "Work-Hardening Induced Tensile Ductility of Bulk Metallic Glasses via High-Pressure Torsion." In: *Scientific reports* 5 (2015), p. 9660. DOI: 10.1038/srep09660 (cit. on p. 76).

[33] J. Bünz et al. "Low Temperature Heat Capacity of a Severely Deformed Metallic Glass." In: *Physical Review Letters* 112.13 (2014). DOI: 10.1103/physrevlett.112.135501 (cit. on p. 76).

[34] J. Das et al. ""Work-Hardenable" Ductile Bulk Metallic Glass." In: *Physical Review Letters* 94.20 (2005). DOI: 10.1103/physrevlett.94.205501 (cit. on p. 76).

[35] H. Asgharzadeh et al. "Consolidation of Cu-based amorphous alloy powders by high-pressure torsion." In: *Journal of Materials Science* 50.8 (2015), pp. 3164–3174. DOI: 10.1007/s10853-015-8877-4 (cit. on p. 77).

[36] J. Sort et al. "Cold-consolidation of ball-milled Fe-based amorphous ribbons by high pressure torsion." In: *Scripta Materialia* 50.9 (2004), pp. 1221–1225. DOI: 10.1016/j.scriptamat.2004.02.004 (cit. on p. 77).

[37] Y. F. Sun et al. "Fabrication of CuZr(Al) bulk metallic glasses by high pressure torsion." In: *Intermetallics* 17.4 (2009), pp. 256–261. DOI: 10.1016/j.intermet.2008.07.023 (cit. on pp. 77, 86, 88).

[38] Y. F. Sun et al. "Fabrication of ZrAlNiCu bulk metallic glass composites containing pure copper particles by high-pressure torsion." In: *Journal of Alloys and Compounds* 492.1-2 (2010), pp. 149–152. DOI: 10.1016/j.jallcom.2009.11.135 (cit. on p. 77).

[39] J. B. Fogagnolo et al. "Consolidation of easy glass former $Zr_{55}Cu_{30}Al_{10}Ni_5$ alloy ribbons by severe plastic deformation." In: *Journal of Metastable and Nanocrystalline Materials* 20-21 (2004), pp. 253–256. DOI: 10.4028/www.scientific.net/JMNM.20-21.253 (cit. on p. 77).

[40] X. Sauvage et al. "Structure and properties of a nanoscaled composition modulated metallic glass." In: *Journal of Materials Science* 49.16 (2014), pp. 5640–5645. DOI: 10.1007/s10853-014-8279-z (cit. on p. 77).

[41] Á. Révész et al. "Deformation induced crystallization in an amorphous $Cu_{60}Zr_{20}Ti_{20}$ alloy by high pressure torsion." In: *Materials Science and Engineering: A* 460-461 (2007), pp. 459–463. DOI: 10.1016/j.msea.2007.01.081 (cit. on p. 77).

[42] A. R. Yavari et al. "Nanostructured bulk $Al_{90}Fe_5Nd_5$ prepared by cold consolidation of gas atomised powder using severe plastic deformation." In: *Scripta Materialia* 46.10 (2002), pp. 711–716. DOI: 10.1016/s1359-6462(02)00057-x (cit. on p. 77).

[43] A. A. Kündig et al. "Metallic glass/polymer composites by co-processing at similar viscosities." In: *Scripta Materialia* 56.4 (2007), pp. 289–292. DOI: 10.1016/j.scriptamat.2006.10.019 (cit. on p. 77).

[44] K. Edalati, Y. Yokoyama, and Z. Horita. "High-Pressure Torsion of Machining Chips and Bulk Discs of Amorphous $Zr_{50}Cu_{30}Al_{10}Ni_{10}$." In: *Materials Transactions* 51.1 (2010), pp. 23–26. DOI: 10.2320/matertrans.mb200914 (cit. on p. 77).

[45] L. Krämer et al. "Production of Bulk Metallic Glasses by Severe Plastic Deformation." In: *Metals* 5.2 (2015), p. 720. DOI: 10.3390/met5020720 (cit. on p. 77).

[46] Tenwick. "Enhanced strength in high conductivity Cu alloys." In: *Materials Science* 98 (1988), pp. 543–546. DOI: 10.1016/0025-5416(88)90226-1 (cit. on pp. 86, 87).

[47] Q. K. Jiang et al. "Zr-(Cu,Ag)-Al bulk metallic glasses." In: *Acta Materialia* 56.8 (2008), pp. 1785–1796. DOI: 10.1016/j.actamat.2007.12.030 (cit. on pp. 86, 88).

[48] H. Men et al. "Bulk glass formation in ternary Cu-Zr-Ti system." In: *Journal of University of Science and Technology Beijing: Mineral Metallurgy Materials (Eng Ed)* 14.SUPPL. 1 (2007), pp. 19–22. DOI: 10.1016/S1005-8850(07)60100-5 (cit. on pp. 86, 88).

[49] Q. Wang et al. "Composition optimization of the Cu-based Cu-Zr-Al alloys." In: *Intermetallics* 12.10 (2004), pp. 1229–1232. DOI: 10.1016/j.intermet.2004.07.002 (cit. on pp. 86, 88).

[50] Y. L. Wang and J. Xu. "Ti (Zr)-Cu-Ni bulk metallic glasses with optimal glass-forming ability and their compressive properties." In: *Metallurgical and Materials Transactions A: Physical Metallurgy and Materials Science* 39.12 (2008), pp. 2990–2997. DOI: 10.1007/s11661-008-9647-6 (cit. on pp. 86, 88).

[51] W. Chen et al. "Bulk metallic glasses in the Zr-Al-Ni-Cu system." In: *Acta Materialia* 51.7 (2003), pp. 1899–1907. DOI: 10.1016/S1359-6454(02)00596-7 (cit. on pp. 86, 88).

[52] Q. He and J. Xu. "Locating Malleable Bulk Metallic Glasses in Zr - Ti - Cu - Al Alloys with Calorimetric Glass Transition Temperature as an Indicator." In: *Journal of Materials Science & Technology* 28.12 (2012), pp. 1109–1122. DOI: 10.1016/S1005-0302(12)60180-7 (cit. on pp. 86, 88).

[53] A. Wiest et al. "Zr -Ti-based Be-bearing glasses optimized for high thermal stability and thermoplastic formability." In: *Acta Materialia* 56.11 (2008), pp. 2625–2630. DOI: 10.1016/j.actamat.2008.02.001 (cit. on pp. 86, 88).

[54] R. Y. Umetsu, R. Tu, and T. Goto. "Thermal and Electrical Transport Properties of Zr-Based Bulk Metallic Glassy Alloys with High Glass-Forming Ability." In: *Materials Transactions* 53.10 (2012), pp. 1721–1725. DOI: 10.2320/matertrans.M2012163 (cit. on pp. 86, 88).

[55] Y. Xu et al. "Enhanced thermal stability and hardness of $Zr_{46}Cu_{39.2}Ag_{7.8}Al_7$ bulk metallic glass with Fe addition." In: *Materials Science and Engineering: A* 527.6 (2010), pp. 1444–1447. DOI: 10.1016/j.msea.2009.10.029 (cit. on pp. 86, 88).

[56] A. Caron et al. "Structurally enhanced anelasticity in Zr-based bulk metallic glasses." In: *Scripta Materialia* 64.10 (2011), pp. 946–949. DOI: 10.1016/j.scriptamat.2011.01.043 (cit. on pp. 86, 88).

[57] C. P. Kim et al. "Fracture toughness study of new Zr-based Be-bearing bulk metallic glasses." In: *Scripta Materialia* 60.2 (2009), pp. 80–83. DOI: 10.1016/j.scriptamat.2008.09.001 (cit. on pp. 86, 88).

[58] J. W. Liu et al. "Shear band evolution and hardness change in cold-rolled bulk metallic glasses." In: *Acta Materialia* 58.14 (2010), pp. 4827–4840. DOI: 10.1016/j.actamat.2010.05.018 (cit. on pp. 86, 88).

[59] X. J. Liu et al. "Atomic packing symmetry in the metallic liquid and glass states." In: *Acta Materialia* 59.16 (2011), pp. 6480–6488. DOI: 10.1016/j.actamat.2011.07.012 (cit. on pp. 86, 88).

[60] D. Ma et al. "Nearest-neighbor coordination and chemical ordering in multicomponent bulk metallic glasses." In: *Applied Physics Letters* 90.21 (2007), pp. 6–9. DOI: 10.1063/1.2742315 (cit. on pp. 86, 88).

C. Bulk metallic dual phase glasses by severe plastic deformation

Lisa Krämer [1], Yannick Champion [2], Karoline S. Kormout[1], Verena Maier-Kiener[3] and Reinhard Pippan [1]

[1] Erich Schmid Institute of materials science, Austrian Academy of Science, Leoben, Austria

[2] Univ. Grenoble Alpes, CNRS, Grenoble INP, SIMaP, F-38000 Grenoble France

[3] Department Physical Metallurgy and Materials Testing, Montanuniversität Leoben, Austria

Abstract. Two different metallic glass powders were consolidated and deformed via high pressure torsion to synthesize amorphous dual phase composites. The influence of volume fraction of the two amorphous phases and the applied shear strain was investigated. By varying the applied strain, the dimensions of the phases could be systematically varied from the micro- to the nanometer regime and at the highest applied strain even a transition to a single phase state could be observed. The study illustrates the potential of producing novel BMGs by deformation-induced mixing which are not accessible by the classical casting route.

Key words: A metallic glass; B mechanical properties, B phase stability, B bonding, C severe plastic deformation, D mechanical properties

C.1. Introduction

Bulk metallic glasses (BMGs) engage the science communities since their discovery in 1960 [1]. Besides studies on single phase BMGs, efforts are made to control the properties by producing bulk metallic glass composites (BMGCs)[2,

3]. Different combinations are possible such as amorphous/crystalline, amorphous/quasicrystalline and amorphous/amorphous[2]. The shape of the second phase can also vary from particles over dendrites to wires and even more complex forms[4–9]. One way to produce amorphous/amorphous composites is by exploiting phase separations, which can occur during annealing in the supercooled liquid region or of the undercooled melt. This chemical demixing is caused by a positive enthalpy of mixing or as pre-stage to primary crystallization. Some well studied compositions for BMGs show this behavior as Vit105, but also Cu-, Ni-, Pd-, Zr- and Mg-based BMGs [2]. Another technique is to use two targets with different chemical composition for inert gas condensation and to produce bulk samples by in-situ compaction[10]. High-pressure torsion (HPT) was used in the past to produce and deform various materials and composites. The advantages of this technique are the high flexibility as the starting material can be either in bulk or powder form and the large variation in applied strain by simply changing the numbers of rotations. Due to the high, nearly hydrostatic pressure, also brittle materials [11, 12] are deformable and the applied strain can go up to shear strains as high as $\gamma = 20000$ and more. This gives the possibility to produce supersaturated solid solutions [13, 14] and amorphization of crystalline phases. BMGs and BMGCs can be produced by HPT [15–26] and furthermore, it can be used for adjusting the microstructure of the composites [27] or rejuvenation of BMGs [28–33].

The aim of this study was to produce amorphous/amorphous BMGCs via HPT and to investigate the evolving microstructures. Main questions addressed are: How does the applied shear strain affect the microstructure? How do the mechanical properties change with refining of the phases? What happens if the applied shear strain goes to very high values? For this purpose, two different compositions (Ni-MG 30wt% Zr-MG and Ni-MG 50wt% Zr-MG) were produced as well as single phase Ni MG and Zr-MG samples as reference. The influences of shear strain and ratio of the two phases were investigated with scanning electron microscopy (SEM), transmission electron microscopy (TEM), X-ray diffraction (XRD), nanoindentation, and hardness measurements.

C.2. Materials and methods

The metallic glass powders ($Zr_{57}Cu_{20}Al_{10}Ni_8Ti_5$ and $Ni_{53}Nb_{20}Ti_{10}Zn_8Co_6Cu_3$, spherical particles with diameters between 1 µm to 40 µm) were fabricated via high pressure gas atomization [3] and were blended in the respective composition by hand. The mixtures were then filled into the gap between two grooved steel anvils and compacted by HPT (4 GPa and 10° rotation). The main deformation was applied at higher pressures (8 GPa to 9 GPa) at room temperature and the rotations were varied from 2 to 100. The thickness varied from 0.45 mm to 0.6 mm due to the anvil preparation, but the diameter of the specimens were constant with 6 mm. The applied shear strain γ can be estimated with

$$\gamma = \frac{2\pi N r}{t} \tag{C.1}$$

where r is the radius of the disk, N is the number of rotations and t is the thickness after deformation. SEM and hardness measurements were performed on the cross sections of the HPT disks, which were produced by wire saw cutting and further grinding and polishing. For TEM samples, small pieces at larger radius (about 2.5 mm) were cut from the disks and the samples were prepared via a standard procedure with dimple grinding and subsequent ion milling (to avoid heating, samples were cooled with liquid nitrogen) in radial direction. Structural analysis were conducted in Carl Zeiss Leo 1525 field emission scanning electron microscope using the back-scatter and in lens detector and in a Cs-corrected JEOL JEM-2100F operated at 200 kV transmission electron microscope. Vickers hardness was measured along the diameter on the cross section with a load of 0.5 kg and 1 kg. An error of 2% for the measured hardness values is assumed and the standard deviation errors of the fitted curve were calculated and used for the error bars in the inlet of Figure C.3.
For the nanoindentation property map, a platform nanoindenter G200 (Keysight Tec) was used and the experiments were conducted under constant indentation strain rate (0.05 s^{-1}) to a maximal indentation depth of 100 nm with a diamond Berkovich tip (Synton-MDP Inc.). Hardness and Young's modulus were measured over indentation depth with a continuous stiffness measurement unit. All data were evaluated according to Oliver and Pharr [34] using a Poisson ration of 0.37 for the modulus and were averaged between indentation depths from 80 nm to 95 nm. To estimate the phase fraction for each indent, SEM micrographs with

very high resolution were taken and the free software ImageJ was used to mark the Ni-MG lamellae by hand (due to the edge effect of the indents an automatic approach was not feasible) and only the regions inside the indents were evaluated. The lamellae thickness was determined by evaluating the intersections with a circle (also in the region of the respective indent), which was performed with an ImageJ plugin called "Oval Profile Plot" by Bill O'Connell [35]. Determining phase fraction and thickness with this methods leads to several errors. One is the lack of information, as the volume beneath the indent is unknown. Another is inaccurate marking of the Ni-MG phase by the author as subjective perception will distort the results (repeating the phase analysis for one indent showed a difference of 4 vol%). A 5-circle X-ray diffractometer equipped with a source for Cu-Kα radiation was used for reflection XRD phase analysis of the Zr-MG and the Ni-MG 50wt% Zr-MG with lower applied deformation. Only pieces from the outer part of samples were used to exclude the nearly undeformed material in the center of the disks. Additionally, the surface was ground to remove any impurities from the HPT process. The other samples were investigated with Synchrotron X-ray diffraction (XRD) performed at the PETRA III P07 beam line at the DESY Photon Science facility (Hamburg) using a beam energy of 111 keV. The primary and secondary slit of $(1 \times 0.25)\,\mathrm{nm}^2$ and $(1 \times 0.3)\,\mathrm{nm}^2$, respectively were used to measure in a small strain range. The measured transmission diffraction patterns were analyzed with FIT 2D software. The theta angles were converted to scattering vector q with

$$q = \frac{4\pi \sin\theta}{\lambda} \tag{C.2}$$

where θ is the reflection angle and λ is the wavelength of the rays. This conversion allows plotting data from the synchrotron and lab diffractometer measurement in one figure.

C.3. Results and discussion

C.3.1. Microstructural evolution as function of strain

The evolution of the microstructure was investigated by SEM, TEM, and XRD. In Figure C.1 a and b, SEM micrographs of two different composites (Ni-MG 30wt% Zr-MG and Ni-MG 50wt% Zr-MG) are shown for different applied strains.

The micrographs in the second row are taken from the same position as the micrograph above but at higher magnifications and the shear direction is indicated with an arrow on the right side. As the starting materials were powders a deformation and consolidation of the powder particles takes place in the beginning. Due to the lower hardness, this consolidation is carried mainly by the Zr-MG (light gray), while the Ni-MG particles (darker gray) show hardly any deformation and the material is hold together by the deformed softer phase (see first micrographs on the left side). The welding of the particles is not completed and the boundaries of the initial powder particles are still visible. As the two powders had similar sizes and forms, no problems regarding agglomeration was expected and at low deformations, good mixing of the two materials was observed. Regions with higher contents of Ni MG result from the higher volume fraction of Ni-MG particles in Ni-MG 30wt% Zr-MG but subsequent deformation ensures a homogeneous distribution of both phases. With higher deformation, both phases are forced to deform and a lamellar structure evolves. This structure refines with increased strain and the lamella length decreases from tens of micrometers to 1 µm and the width from 10 µm below 10 nm. TEM micrographs in Figure C.1 c, show the fine microstructure of Ni-MG 30wt% Zr-MG at $\gamma = 1200$. Thin and long lamellae are sometimes disrupted by shear bands, which cause steps and further refine the phases. At very high shear strains, a saturation is reached, where only one phase is detectable in the micrographs. A single phase microstructure imaged by SEM can be explained by a refinement of the lamellae below the resolution limit or mixing of the two MGs into a new phase. Changing the ratio of the two MGs, leads to a slightly different microstructure evolution. Ni-MG 50wt% Zr-MG shows a fast consolidation at the beginning as the fraction of the softer phase is relatively high and it can act as glue to the harder Ni MG particles. Therefore, no cracks are detectable even at low strains as $\gamma = 60$ (see Figure C.1 b). On the other hand, the high fraction of the softer Zr-MG can carry most of the applied strain and the Ni-MG is not forced to deform. This leads to an inhomogeneous deformation behavior, where large Ni-MG lamellae can still be found even at very high strains ($\gamma = 2700$). If the fraction of the harder phase is higher, strains higher than $\gamma = 590$ must be applied to achieve fully dense samples without cracks along the phase boundaries (see Figure C.1 a). The delay of the consolidation is caused by the lower fraction of the glue-like phase, which cannot hold all Ni-MG particles together, and by the hardness of the Ni-MG, which impedes fast welding of the Ni-MG particles. The lower

fraction of the softer phase forces the Ni-MG to carry more of the deformation and this causes a more homogenous deformation. The lamellae thickness is more evenly distributed and the saturation is reached at lower strains compared Ni-MG 50wt% Zr-MG.

In Figure C.2 a, XRD profiles of the two single phase BMGs and the two composites are shown with intensity as a function of the scattering vector q. For Ni-MG 50wt% Zr-MG, profiles of two different samples are shown. For one profile, an intermediate microstructure was chosen. In this state, two overlapping amorphous peaks from the two initial MGs can be seen. The second profile is acquired at higher applied shear strains; only one amorphous peak is detectable and its position lays between the positions of the amorphous peaks of the initial two metallic glasses. This can be explained by generating a new amorphous phase by mixing of the two initial MGs. Generating a single phased MG consists with SEM-micrographs, where also only one phase is detectable at high applied shear strains (see Figure C.1). For Ni-MG 30wt% Zr-MG, only the profile at saturation is shown, where a single amorphous peak is detectable. The saturation peak position depends on the composition and shifts linearly with the percentage of the phases. This can be seen in Figure C.2 b, where the peak position is plotted depending on the vol% of Ni-MG. Higher vol% of Ni-MG means a higher fraction of Ni in the metallic glass and the position shifts linearly to higher q values.

C.3.2. Influences of the microstructure on mechanical properties

The microhardness as a function of the strain is shown in Figure C.3 3. The plotted lines should help to guide the eye and have no physical meaning. Zr-MG shows a nearly constant hardness as a function of the applied strain and the large scattering at small strain can be explained by an incomplete welding of the particles, where cracks and inhomogeneities reduce the hardness. Ni-MG shows a slight softening with higher applied shear strain. Zr-MG and Ni-MG have a saturation hardness of 470 and 640 HV, respectively. In comparison, the hardness of the composites increases with the applied strains at the beginning, but then flattens until a saturation is reached. For Ni-MG 30wt% Zr-MG, the scatter of the hardness at low strains is very high, which is caused by the inhomogeneous microstructure with cracks and undeformed particles (see micrographs in Figure C.1 a and b at $\gamma = 180$), compared to Ni-MG 50wt% Zr-MG. In the inlet,

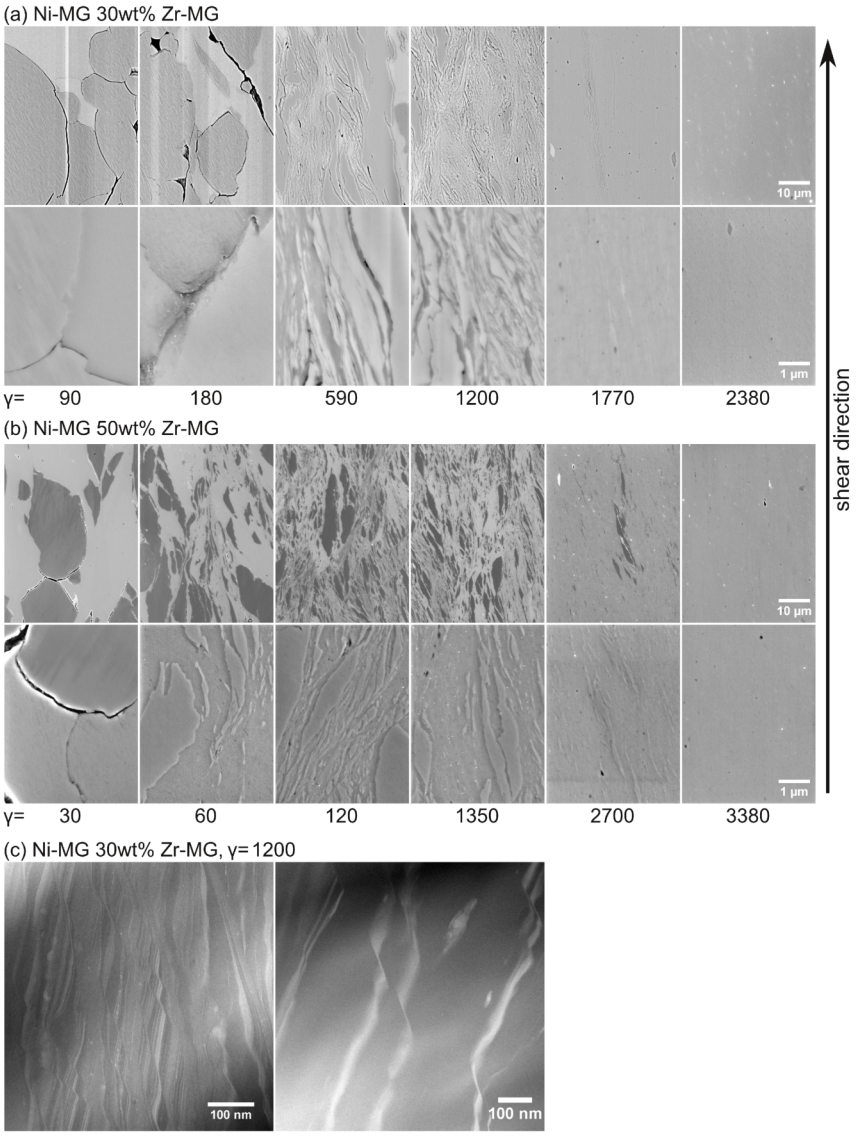

Figure C.1.: Illustration of the microstructure of (a) Ni-MG 30wt% Zr-MG (SEM micrographs), (b) Ni-MG 50wt% Zr-MG (SEM micrographs) and (c) Ni-MG 30wt% Zr-MG at $\gamma = 1200$ (TEM micrographs). In (a) and (b) the top and bottom row of micrographs are taken at different magnifications. The evolution of the microstructure can be seen in dependence of the applied strain. The deformation increases from the left to the right and the microstructure changes from Ni-MG particles hold together by the softer Zr-MG to a lamellar structure. These lamellae refine with increasing applied strain until a complete mixing of the two phases occurs. Take notice in the increase of applied strain for higher contents of Zr-MG to reach saturation. The evolving fine lamellar structure can be seen in (c) and lamellar thickness decreases below 10 nm.

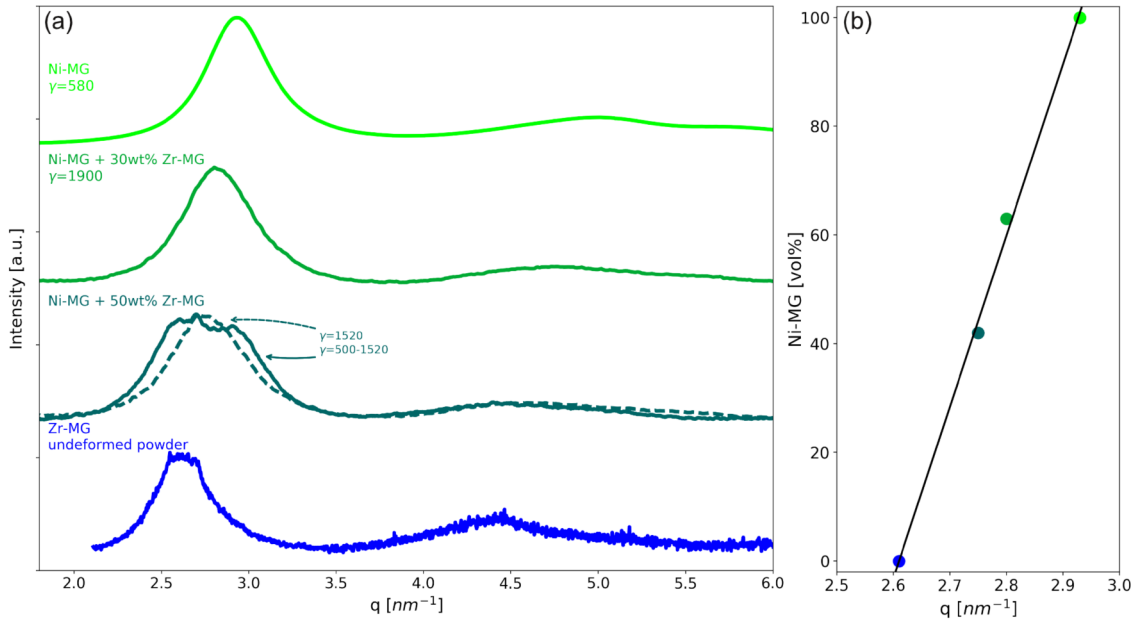

Figure C.2.: (a) XRD results of different composite concentrations. For Ni-MG 50wt% Zr-MG, samples with transient microstructure was measured and two overlapping peak of the initial MGs can be seen as well as a rising peak in between from the new MG. At saturation, both composites show just one remaining amorphous peak. (b) Positions of the first amorphous peak from XRD measurements depending on the composition. The position correlates linearly with the chemical composition of the composites. Higher fractions of Ni shifts the peak to higher q values.

the approximated saturation values are plotted over the vol% of Ni MG. The saturation hardness of the two composites lays between the hardness of the two initial MGs and depends directly on the fraction of the two MGs, but is higher than the rule of mixture predicts. In literature two different explanation can be found for an increased hardness level induced by compositional changes. Deng et al. supposed the presence of a harder crystalline phase for some compositions [36]. However, crystallization even on the nanoscale was excluded for this study by TEM investigations. Donald *et al.* showed a correlation of the hardness with the average outer electron concentration by adding different elements [37]. The composition changes drastically by mixing of the two amorphous phases and for this reason, a change in the outer electron concentration can be assumed. This can explain the discrepancy between the actual hardness and the one the rule of mixture predicts. The higher hardness of the newly formed amorphous phase causes the increase in hardness for intermediate strain regime, but a size effect cannot be ruled out. Thinning of the lamellae and increasing the number of interfaces can also influence the hardness and further studies must be conducted.

Nanoindentation was used to investigate the influence of the lamella thickness and the ratio of the two phases. In Figure C.4 a, a micrograph with a properties map with three times eight indentations is shown. The residual imprints are colored according to the measured nanohardness and the scale bar can be seen on the right side. Additionally, colored micrographs for phase analysis are added for some indentation marks. At first glance, it can be seen that the large Ni-MG particle has a higher hardness than the surrounding area, in which Zr-MG and Ni-MG contribute to the observed hardness. In Figure C.4 b, the hardness and the Young's modulus of the indentations are plotted as a function of the measured volume fraction of the Ni MG, which was calculated from SEM micrographs as shown in the small inlets in Figure C.4 a. Additionally, average values from reference nanoindentation data of the two single phase and two composites at saturation are plotted for comparison reasons. The trend shows that for both, properties map and reference indentations, Young's modulus and hardness increase with increasing volume fraction of the Ni-MG, which is harder and stiffer than the Zr MG. One challenge of measuring the volume fraction is the mixing of the two phases, which already occurs in the finer structured regions of the map. This directly leads to an underestimation of the volume fraction of Ni-MG in this region and also to a corresponding increase of the hardness as the new

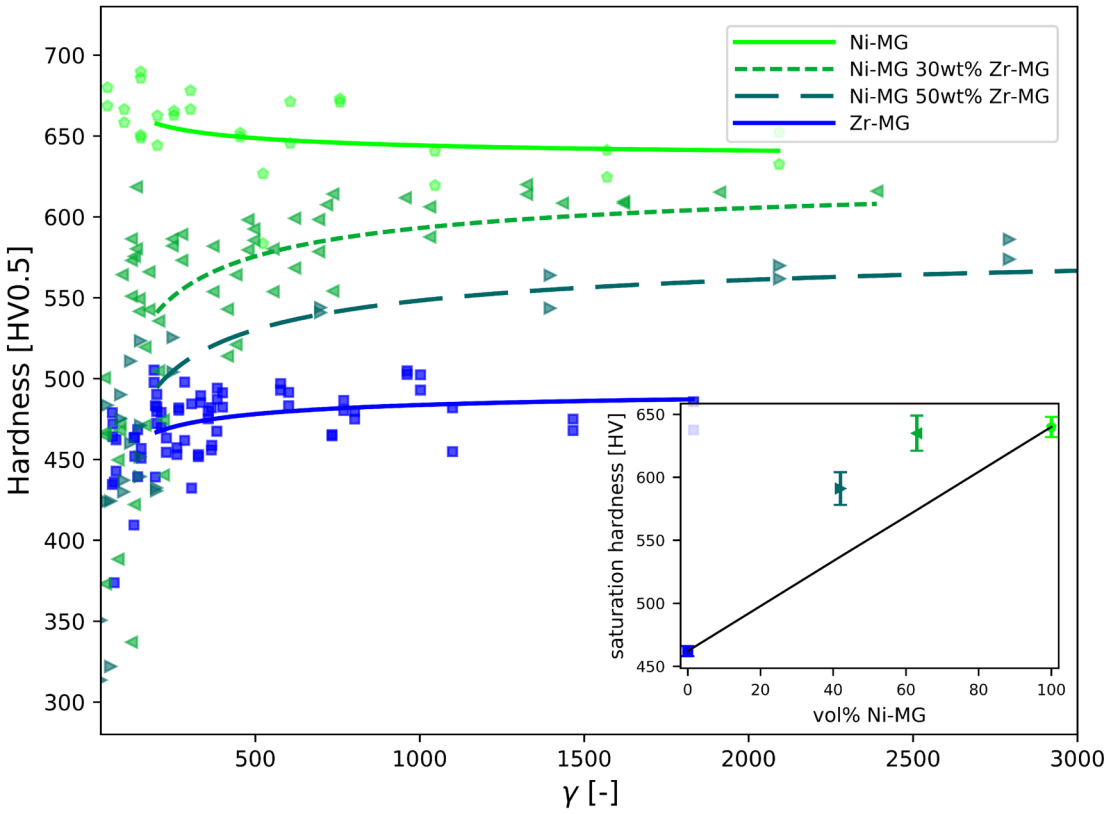

Figure C.3.: Illustration of the Vickers micro hardness evolution as a function of the shear strain. The hardness of the single phase BMGs is constant over the applied strain, whereas the composites show a strong increase in hardness at low strains and then a saturation. The saturation hardness lays higher than the rule of mixture predicts (black line in the inlet)

phase has a higher hardness, which can be also seen in comparison with reference indentations in the composite structures at saturation. The lamella thickness of the Ni-MG does not have a significant influence on the hardness, which can be seen by comparing the fifth indentation of the first row and the first indentation of the third row. Both show nearly the same hardness (10.23 and 10.29 GPa), although the one in the first row indents mainly a large lamella whereas the second one probes a region with a very fine microstructure. In Figure C.4 4c, the nanohardness and Young's modulus are plotted versus the thickness of the Ni-MG lamellae and no significant correlation is obvious. Therefore, no size effect larger than the systematic measurement error of the lamellae thickness was detected. This can be explained by TEM micrographs (Figure C.1 c), where shear bands propagate through both phases without deflection at the boundaries. For this system, phase boundaries provide no barrier to shear bands and therefore no increase in hardness is observed at smaller lamellae. Other systems that comprise amorphous phases with different properties (different Poisson ratios) might show a size effect.

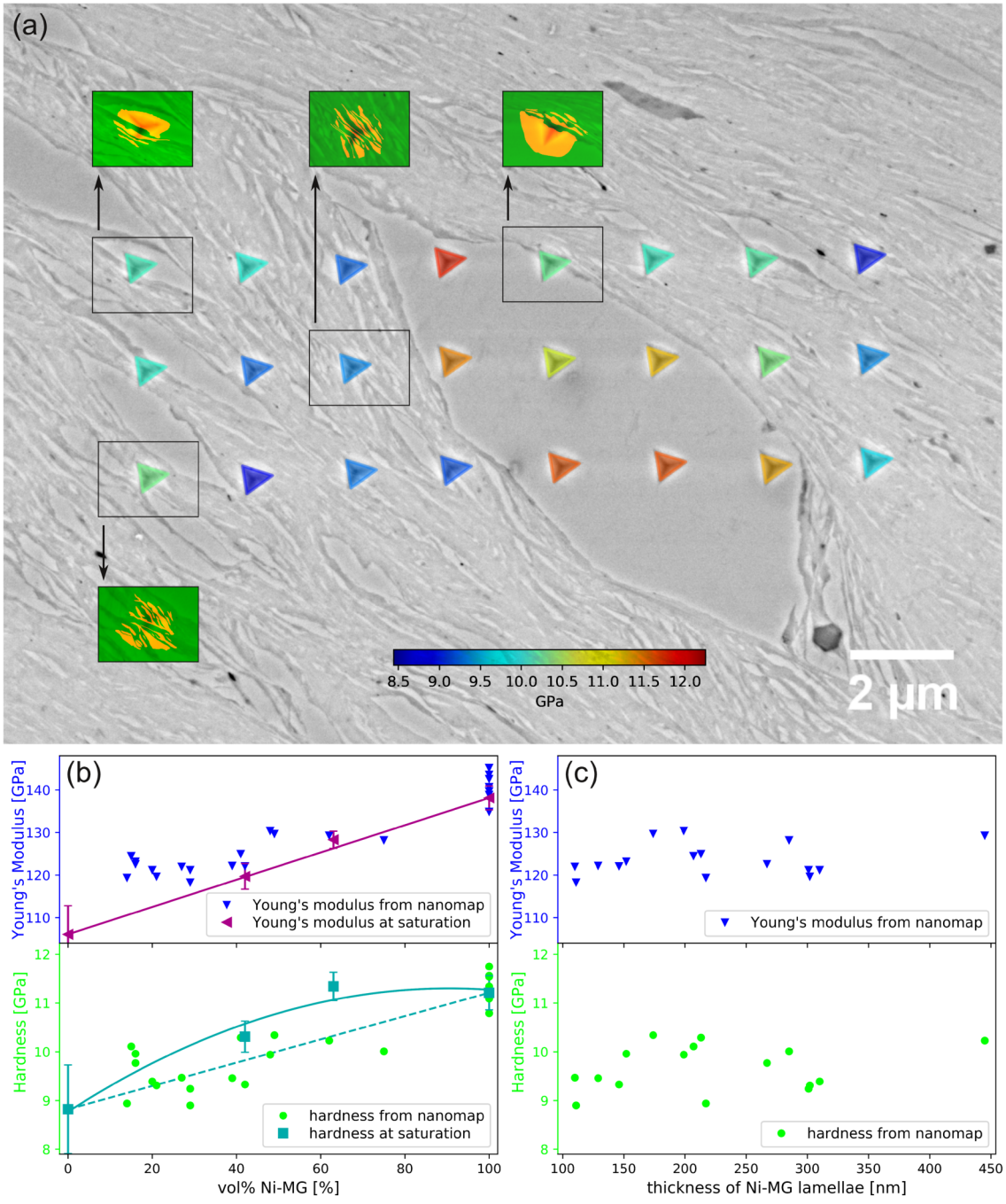

Figure C.4.: (a) Illustration of a nanoindentation property map, graphs of (b) the Young's modulus (blue) and hardness (green) depending on the phase fractions in the impressions, and (c) the Young's modulus and hardness depending on the lamellae thickness. The residual impressions in (a) are colored respective to their measured hardness and for four indentation marks, micrographs with colored phases are included. Graphs in (b) and (c) show that the hardness and Young's modulus depend on the volume fraction of the phases, but not on the lamellae thickness.

C.4. Conclusion

In summary, it was successfully shown that HPT can be used to generate amorphous/amorphous composites in bulk size and the microstructure can be controlled by the applied strain. The lamellar structure is tunable from the micrometer to the nanometer regime and at very high strains, even mixing of the two amorphous materials towards single phased BMGs occurs. The ratio of the two initial amorphous phases is smoothly adaptable, because powders were used as starting materials and therefore BMGs with different chemical compositions are producible. Higher fractions of the softer phases enhances consolidation and a crack free microstructure is reached at low strains. It also hinders a homogenous deformation and the saturation shifted to higher strains. Hardness measurements show that mixing and ratio of the two phases have a stronger influence on the mechanical properties than the microstructure. Hardness and Young's modulus correlates with the ratio of the two phases, but no clear size effect was detectable. At saturation, the newly formed amorphous phases have a hardness between the initial MGs, but higher than the rule of mixture predicts.

Acknowledgments

The European Research Council under ERC Grant Agreement No. 3401 85 USMS has provided funding for this work. The financial support by the Austrian Federal Government (837900) within the framework of the COMET Funding Program (MPPE, A7.19) is highly appreciated.

C.5. References

[1] W. Klement, R. H. Willens, and P. Duwez. "Non-crystalline Structure in Solidified Gold–Silicon Alloys." In: *Nature* 187.4740 (1960), pp. 869–870. DOI: 10.1038/187869b0 (cit. on p. 99).

[2] J. Eckert et al. "Mechanical properties of bulk metallic glasses and composites." In: *Journal of Materials Research* 22.02 (2007), pp. 285–301. DOI: 10.1557/jmr.2007.0050 (cit. on pp. 99, 100).

[3] L. Perrière and Y. Champion. "Phases distribution dependent strength in metallic glass – aluminium composites prepared by spark plasma sintering." In: *Materials Science & Engineering A* 548 (2012), pp. 112–117. DOI: 10.1016/j.msea.2012.03.100 (cit. on pp. 99, 101).

[4] H. Choi-Yim et al. "Synthesis and characterization of particulate reinforced $Zr_{57}Nb_5Al_{10}Cu_{15.4}Ni_{12.6}$ bulk metallic glass composites." In: *Acta Materialia* 47.8 (1999), pp. 2455–2462. DOI: 10.1016/s1359-6454(99)00103-2 (cit. on p. 100).

[5] R. D. Conner, R. B. Dandliker, and W. L. Johnson. "Mechanical properties of tungsten and steel fiber reinforced Zr41.25Ti13.75Cu12.5Ni10Be22.5 metallic glass matrix composites." In: *Acta Materialia* 46.17 (1998), pp. 6089–6102. DOI: 10.1016/S1359-6454(98)00275-4 (cit. on p. 100).

[6] S. T. Deng et al. "Metallic glass fiber-reinforced Zr-based bulk metallic glass." In: *Scripta Materialia* 64.1 (2011), pp. 85–88. DOI: 10.1016/j.scriptamat.2010.09.014 (cit. on p. 100).

[7] Y.-K. Xu et al. "Mg-based bulk metallic glass composites with plasticity and gigapascal strength." In: *Acta Materialia* 53.6 (2005), pp. 1857–1866. DOI: 10.1016/j.actamat.2004.12.036 (cit. on p. 100).

[8] T. Liu et al. "Synthesis and mechanical properties of TiC-reinforced Cu-based bulk metallic glass composites." In: *Scripta Materialia* 60.2 (2009), pp. 84–87. DOI: 10.1016/j.scriptamat.2008.09.004 (cit. on p. 100).

[9] H. Shakur Shahabi et al. "Metallic glass–steel composite with improved compressive plasticity." In: *Materials & Design* 59 (2014), pp. 241–245. DOI: 10.1016/j.matdes.2014.03.007 (cit. on p. 100).

[10] N. Chen et al. "A nanoglass alloying immiscible Fe and Cu at the nanoscale." In: *Nanoscale* 7.15 (2015), pp. 6607–6611. DOI: 10.1039/c5nr01406a (cit. on p. 100).

[11] K. Edalati et al. "Plastic Deformation of $BaTiO_3$ Ceramics by High-pressure Torsion and Changes in Phase Transformations, Optical and Dielectric Properties." In: *Materials Research Letters* 3.4 (2015), pp. 216–221. DOI: 10.1080/21663831.2015.1065454 (cit. on p. 100).

[12] H. Razavi-Khosroshahi et al. "Plastic strain and grain size effect on high-pressure phase transformations in nanostructured TiO_2 ceramics." In: *Scripta Materialia* 124 (2016), pp. 59–62. DOI: 10.1016/j.scriptamat.2016.06.022 (cit. on p. 100).

[13] K. S. Kormout, R. Pippan, and A. Bachmaier. "Deformation-Induced Supersaturation in Immiscible Material Systems during High-Pressure Torsion." In: *Advanced Engineering Materials* 19.4 (2016), p. 1600675. DOI: 10.1002/adem.201600675 (cit. on p. 100).

[14] A. Bachmaier et al. "Supersaturation in Ag–Ni alloy by two-step high-pressure torsion processing." In: *Philosophical Magazine Letters* 94.1 (2014), pp. 9–17. DOI: 10.1080/09500839.2013.852284 (cit. on p. 100).

[15] A. R. Yavari et al. "Nanostructured bulk $Al_{90}Fe_5Nd_5$ prepared by cold consolidation of gas atomised powder using severe plastic deformation." In: *Scripta Materialia* 46.10 (2002), pp. 711–716. DOI: 10.1016/s1359-6462(02)00057-x (cit. on p. 100).

[16] J. Sort et al. "Cold-consolidation of ball-milled Fe-based amorphous ribbons by high pressure torsion." In: *Scripta Materialia* 50.9 (2004), pp. 1221–1225. DOI: 10.1016/j.scriptamat.2004.02.004 (cit. on p. 100).

[17] Á. Révész et al. "Deformation induced crystallization in an amorphous $Cu_{60}Zr_{20}Ti_{20}$ alloy by high pressure torsion." In: *Materials Science and Engineering: A* 460-461 (2007), pp. 459–463. DOI: 10.1016/j.msea.2007.01.081 (cit. on p. 100).

[18] J. B. Fogagnolo et al. "Consolidation of easy glass former $Zr_{55}Cu_{30}Al_{10}Ni_5$ alloy ribbons by severe plastic deformation." In: *Journal of Metastable and Nanocrystalline Materials* 20-21 (2004), pp. 253–256. DOI: 10.4028/www.scientific.net/JMNM.20-21.253 (cit. on p. 100).

[19] A. A. Kündig et al. "Metallic glass/polymer composites by co-processing at similar viscosities." In: *Scripta Materialia* 56.4 (2007), pp. 289–292. DOI: 10.1016/j.scriptamat.2006.10.019 (cit. on p. 100).

[20] Y. F. Sun et al. "Fabrication of ZrAlNiCu bulk metallic glass composites containing pure copper particles by high-pressure torsion." In: *Journal of Alloys and Compounds* 492.1-2 (2010), pp. 149–152. DOI: 10.1016/j.jallcom.2009.11.135 (cit. on p. 100).

[21] Y. F. Sun et al. "Fabrication of CuZr(Al) bulk metallic glasses by high pressure torsion." In: *Intermetallics* 17.4 (2009), pp. 256–261. DOI: 10.1016/j.intermet.2008.07.023 (cit. on p. 100).

[22] K. Edalati, Y. Yokoyama, and Z. Horita. "High-Pressure Torsion of Machining Chips and Bulk Discs of Amorphous $Zr_{50}Cu_{30}Al_{10}Ni_{10}$." In: *Materials Transactions* 51.1 (2010), pp. 23–26. DOI: 10.2320/matertrans.mb200914 (cit. on p. 100).

[23] X. Sauvage et al. "Structure and properties of a nanoscaled composition modulated metallic glass." In: *Journal of Materials Science* 49.16 (2014), pp. 5640–5645. DOI: 10.1007/s10853-014-8279-z (cit. on p. 100).

[24] H. Asgharzadeh et al. "Consolidation of Cu-based amorphous alloy powders by high-pressure torsion." In: *Journal of Materials Science* 50.8 (2015), pp. 3164–3174. DOI: 10.1007/s10853-015-8877-4 (cit. on p. 100).

[25] J. Qiang and K. Tsuchiya. "Concurrent solid-state amorphization and structural rejuvenation in Zr-Cu-Al alloy by high-pressure torsion." In: *Materials Letters* 204 (2017), pp. 138–140. DOI: 10.1016/j.matlet.2017.06.032 (cit. on p. 100).

[26] L. Krämer et al. "Production of Bulk Metallic Glasses by Severe Plastic Deformation." In: *Metals* 5.2 (2015), p. 720. DOI: 10.3390/met5020720 (cit. on p. 100).

[27] L. Krämer, Y. Champion, and R. Pippan. "From powders to bulk metallic glass composites." In: *Scientific Reports* 7.1 (2017). DOI: 10.1038/s41598-017-06424-4 (cit. on p. 100).

[28] Y. B. Wang et al. "Introducing a strain-hardening capability to improve the ductility of bulk metallic glasses via severe plastic deformation." In: *Acta Materialia* 60.1 (2012), pp. 253–260. DOI: 10.1016/j.actamat.2011.09.026 (cit. on p. 100).

[29] X. D. Wang et al. "Atomic-level structural modifications induced by severe plastic shear deformation in bulk metallic glasses." In: *Scripta Materialia* 64.1 (2011), pp. 81–84. DOI: 10.1016/j.scriptamat.2010.09.015 (cit. on p. 100).

[30] F. Meng et al. "Reversible transition of deformation mode by structural rejuvenation and relaxation in bulk metallic glass." In: *Applied Physics Letters* 101.12 (2012), p. 121914. DOI: 10.1063/1.4753998 (cit. on p. 100).

[31] S.-h. Joo et al. "Work-Hardening Induced Tensile Ductility of Bulk Metallic Glasses via High-Pressure Torsion." In: *Scientific reports* 5 (2015), p. 9660. DOI: 10.1038/srep09660 (cit. on p. 100).

[32] J. Das et al. ""Work-Hardenable" Ductile Bulk Metallic Glass." In: *Physical Review Letters* 94.20 (2005). DOI: 10.1103/physrevlett.94.205501 (cit. on p. 100).

[33] J. Bünz et al. "Low Temperature Heat Capacity of a Severely Deformed Metallic Glass." In: *Physical Review Letters* 112.13 (2014). DOI: 10.1103/physrevlett.112.135501 (cit. on p. 100).

[34] W. C. Oliver and G. M. Pharr. "An improved technique for determining hardness and elastic modulus using load and displacement sensing indentation experiments." In: *Journal of Materials Research* 7.06 (1992), pp. 1564–1583. DOI: 10.1557/jmr.1992.1564 (cit. on p. 101).

[35] B. O'Connell. *Oval Profile Plot*. 2017. URL: https://imagej.nih.gov/ij/plugins/oval-profile.html (visited on 08/18/2017) (cit. on p. 102).

[36] Y. P. Deng et al. "A combinatorial thin film sputtering approach for synthesizing and characterizing ternary ZrCuAl metallic glasses." In: *Intermetallics* 15.9 (2007), pp. 1208–1216. DOI: 10.1016/j.intermet.2007.02.011 (cit. on p. 107).

[37] I. W. Donald and H. A. Davies. "The influence of transition metal substitutions on the formation, stability and hardness of some Fe- and Ni-based metallic glasses." In: *Philosophical Magazine A* 42.3 (1980), pp. 277–293. DOI: 10.1080/01418618008239359 (cit. on p. 107).

D. Activation volume and energy of bulk metallic glasses determined by nanoindentation

Lisa Krämer [1], Verena Maier-Kiener[2], Yannick Champion [3], Baran Sarac[1] and Reinhard Pippan [1]

[1] Erich Schmid Institute of materials science, Austrian Academy of Science, Leoben, Austria
[2] Department Physical Metallurgy and Materials Testing, Montanuniversität Leoben, Austria
[3] Univ. Grenoble Alpes, CNRS, Grenoble INP, SIMaP, F-38000 Grenoble France

Key words: bulk metallic glasses; activation volume; activation energy; nanoindentation strain rate jump tests; high pressure torsion; thermal cycling

Abstract. Nanoindentation strain-rate jump testing was used to determine activation volumes and energies of various metallic glasses and composites. Three different single phase metallic glasses and three composites (two with amorphous/crystalline Cu and one with an amorphous/amorphous structure) were investigated. The state of the materials was additionally changed by varying the testing temperature between room temperature and 430 °C, by performing high pressure torsion and by thermal cycling. The results show that testing temperature is the main parameter controlling activation volume and energy, whereas material modifications by high pressure torsion and thermal cycling do not significantly affect them.

D.1. Introduction

Bulk metallic glasses (BMG) have no long-range order due to their amorphous structure, but it has been shown numerously that their short-range order is of great importance. By changing the short-range order and therefore the state of the metallic glass, intrinsic properties such as e.g. hardness or toughness can be changed [1, 2]. The state of BMGs can be changed by varying the composition, casting conditions or additional annealing and rejuvenating treatments [3–6]. Rejuvenation of BMGs can be achieved by thermal cycling or deformation [3, 7]. One of the most effective techniques for achieving the latter is high-pressure torsion (HPT). A disc-like specimen is placed between two anvils which are rotated against each other under high pressure of more than three times the yield stress of the material, for details see [8, 9]. Due to its nearly hydrostatic pressure, enormous equivalent shear strains higher than 20,000 can be applied. Even materials which are brittle and fail catastrophically under standard deformation conditions can be deformed with HPT. This makes the technique interesting for optimizing BMGs and producing bulk metallic glass composites (BMGCs) [10–12]. To quantify the influence of changing the short-range order and free volume, different techniques such as transmission X-ray diffraction during cyclic heating [13] or creep testing [14], positron annihilation spectroscopy [15] and DSC [16] have been used. Nanoindentation is commonly used to determine activation volume and energy of crystalline materials by using different strain rates for testing. Maier *et al.* suggested using different strain rates during indentation and therefore, the testing time could be shortened significantly, but this technique also allows probing of selected regions with different strain rates, which can be important for heterogeneous materials [17]. Therefore, strain rate sensitivity and consequently the activation volume can be determined by means of only a single indent [18]. During nanoindentation of BMGs, a serrated flow behavior often occurs, and Wright *et al.* concluded that each serration was the onset of a shear band [19]. These serrations or pop-ins depend on strain rate and temperature, but they are similar in frequency and size for different BMGs if the testing was conducted at the same homologous temperature (T/T_g, where T is the testing and T_g is the glass transition temperature)[20–23]. Annealing of BMGs decreases the free volume and increases Young's modulus and hardness, but no significant effect on the serration behavior during nanoindentation is detectable [24]. Not only the strain rate, but also the tip geometry [25] and residual stresses [26,

27] influence the number and size of the serrations. Different methods have attempted to evaluate the serration behavior and try to link it to the deformation behavior of the BMGs, such as the examination of the first pop-in for different strain rates using a cooperative shear model [28], the evaluation of the first pop-in depending on a critical strain by using a spherical indenter [29] or the use of a mean field model to link the slip avalanches to annealing temperatures [30]. In literature, activation volumes for BMGs were also obtained by evaluating the depth variation during a constant load experiment by nanoindentation [31], nanoindenter cantilever bending and mandrel bend relaxation techniques [32], pseudo-creep and compression testing with different strain rates at elevated temperatures [33], and three point bending tests at different temperatures[34].
The aim of this study was to elucidate whether small-scaled strain rate jump tests by nanoindentation can be used reliably to calculate activation energy and volume for plastic deformation in BMGs. Considering the amorphous structure, a different approach than for crystalline materials is proposed. The influence of composition was investigated by means of three different bulk metallic glasses, as well as the influence of a second phase by testing three different BMGCs (two with crystalline Cu and one with another MG as the second phase). Two specimens were additionally subjected to HPT and two to thermal cycling. The main questions that will be addressed are: How do the activation energy and volume differ for different compositions and fabrication methods? How does a second phase influence these two properties? How do the properties vary with the testing temperature? And have HPT-deformation and thermal cycling an influence on activation volume and energy?

D.2. Experimental

Experimental Three Zr-based and one Ni-based MGs were investigated. ZrBe-MG ($Zr_{35}Ti_{30}Cu_{7.5}Be_{27.5}$) was rod cast with 10 mm diameter [35–37]. Zr-MG ($Zr_{57}Cu_{20}Al_{10}Ni_8Ti_5$) and Ni-MG ($Ni_{53}Nb_{20}Ti_{10}Zn_8Co_6Cu_3$) samples were produced from amorphous powders (high pressure gas atomization [38]) with subsequent consolidation and deformation by HPT to achieve bulk samples. By this method, composites containing the Zr-MG and Ni-MG or Zr-MG and crystalline Cu can also be fabricated. This process and the evolution of their microstructures are described in detail in previous papers [10–12]. For this

study, samples with between 30-50 turns of deformation by HPT were used. The single-phased BMGs generated from powders require a minimal strain to ensure fully consolidated samples[12]. For the amorphous/crystalline and amorphous/amorphous composites, the applied strain is even more important for the microstructural evolution. The shear strain and pressure cause consolidation and a lamellar structure of the different phases, which refines as the applied strain is increased. This increase in strain can be realized by either increasing the number of turns in the HPT-process or by investigated the samples at a larger radius. At large strains, mixing of the two phases occurs, which leads at very high applied shear stains to saturation resulting in a single-phased amorphous material for Zr-MG 20wt% Cu and Ni-MG 30wt% Zr-MG. The saturation microstructure of Zr-MG 80wt% Cu contains nanocrystalline supersaturated solid solution Cu in which elongated Zr-MG bands are embedded. Since we are interested in the effect of composites on the activation volume and energy for this study, the testing area was chosen where the phase spacing was smaller than the imprints of the nanoindentation, but where the two phases are not fully mixed. Furthermore, it was tried for each sample to minimize the variation of the radius at which the indents were performed to probe comparable microstructures. In Figure D.1, representative scanning electron microscopy (SEM) micrographs of the microstructure of the three composites (Zr-MG 20wt% Cu, Zr-MG 80wt% Cu, and Ni-MG 30wt% Zr-MG) are shown. Due to the oxidation of the surface, the fine microstructure is not clearly visible after high temperature testing.
One ZrBe-MG specimen was deformed by HPT for 20 turns to investigate the influence of predeformation.
One Zr MG and one Ni-MG sample were thermally cycled by cooling with liquid nitrogen for one minute and then heating with a hot-air gun to room temperature for one minute.
Differential Scanning Calorimetry (DSC) was conducted for 15 mg pieces of Zr-MG and ZrBe-MG using a heating and cooling rate of $10\,\mathrm{K\,s^{-1}}$ (Mettler Toledo DSC3+). The results show a glass transition temperature of 405 °C and 290 °C, respectively. For Ni-MG literature indicates a T_g of approximately 571 °C, which is significantly higher than the maximum nanoindentation testing temperature [39].

For micromechanical investigations, the surface was ground and polished. The nanoindentation testing was limited to regions of the same applied strain for HPT-deformed samples, thus at the same radius of the deformed disks. The

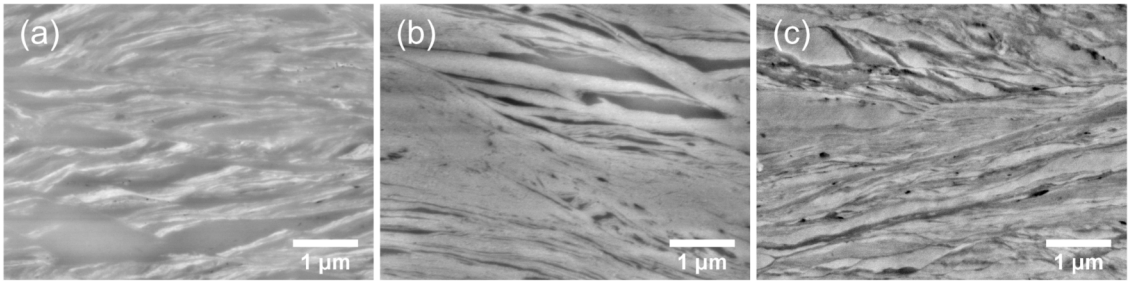

Figure D.1.: SEM micrographs of representative microstructure of the three tested composites. (a) Zr-MG 20wt% Cu, (b) Zr-MG 80wt% Cu and (c) Ni-MG 30wt% Zr-MG. HPT-deformation causes a gradual refinement along the radius and therefore, a variation of the tested microstructure is not preventable. The side length of a the Berkovich indents is approximately 15 µm.

as-cast sample was probed in the central region to avoid influences from the cast surface. For all depth sensing hardness testing experiments, a platform nanoindenter G200 (Keysight Tec, USA) equipped with CSM (continuous stiffness measurement) Young's modulus as well as a Laser Heating stage (Surface Tec, Hückelhoven, Germany) was used. Latter one allows the independent heating of the indentation tip and the sample, which ensures a fine adjustment of both temperatures to precisely adjust the exact contact temperature. Thus, possible thermal drift can be further minimized even at elevated temperatures [40]. The testing temperatures were varied between room temperature and 430 °C and the intervals were chosen according to the transition in mechanical properties respectively for each specimen. Moreover, at elevated temperatures tip and sample were independently but continuously jetted with forming gas in order to minimize any oxidation reactions on the surface. For room temperature tests, the system was equipped with a diamond Berkovich tip (Synton-MPD, Switzerland), while for elevated temperature testing a sapphire Berkovich tip (Synton-MPD, Switzerland/ Surface Tec, Hückelhoven) was used in order to minimize chemical reactions between tip and sample at higher temperatures [41]. All indentations were generally conducted under strain rate controlled conditions and with abrupt, repetitive changes in the applied strain rate ($\dot{\epsilon} = h/\dot{h} = P/2\dot{P}$) [42] to a maximal indentation depth of 2500 nm. For this study the strain rate was changed after every 500 nm of the indentation depth with different profiles for room temperature[17]: 0.025 – 0.0025 – 0.025 – 0.0005 – 0.025 s^{-1} and for elevated temperatures [43]: 0.025 – 0.005 – 0.025 – 0.0025 – 0.025 s^{-1}. Hardness and Young's modulus were measured continuously over indentation depth with a CSM unit, where a sinusoidal load signal is superimposed to the load

displacement data and the data were corrected according to Pharr *et al.*[44]. All data were evaluated according to the method of Oliver and Pharr [45] using a Poisson ratio of 0.37 to calculate the Young's modulus and the averaged data were calculated from the third strain rate regime between indentation depths from 1050 nm to 1450 nm for a strain rate of $0.025\,s^{-1}$.
One minor problem occurring during testing was a slight break out at the very end of the high temperature sapphire Berkovich indenter just before testing the ZrBe-MG. Thereby, the tip calibration became inaccurate for the testing series at elevated temperature of this material. This influence is clearly seen for the Young's modulus as a function of the indentation depth especially at smaller indentation depth and lower temperatures. Nevertheless, the data from larger indentation depths were used qualitatively, as the overall trend of the measured and calculated properties is similar to the other tested materials.

D.3. Results

D.3.1. Evaluation of the strain rate jump tests

Nanoindentation was conducted on above described different BMGs and BMGCs samples. Changes in deformation mechanism were investigated by changing the testing temperatures and the history of the samples using HPT or thermal cycling. To estimate activation volume and activation energy, an equation proposed by Spaepen [46], was used. This equation links the plastic flow rate with a net jump frequency of flow defects under the influence of stress

$$\dot{\gamma} = n\gamma_0 v_0 k_a \sinh\left(\frac{\tau\gamma_0 v_0}{kT}\right) \exp\left(-\frac{\Delta G}{kT}\right) \tag{D.1}$$

where n is the concentration of flow defects, γ_0 the shear strain produced by rearranging of a flow defect, v_0 is the volume of a flow defect, k_a the jump frequency, τ the shear stress, k the Boltzmann constant and ΔG the activation energy. The advantage of this equation is its generality, as the flow defects can be single atoms, dislocations in crystalline metals or shear transformation zones in metallic glasses. The flow defects vibrate due to thermal energy and at higher temperature ΔG can be overcome (exponential part of Equation 1), which leads to local shearing. At lower temperature, an additional energy for moving flow

defects is necessary. Mechanical stress on the flow defects are represented as a hyperbolic energy term. This hyperbolic part leads to a favored jump direction for the flow defects and therefore to a higher numbers of jumps in one direction than in another. Langer [47] pointed out that this equation neglects several aspects such as anisotropy and heterogeneity of the material, but we assume it is valid for an estimation of dominating deformation processes in metallic glasses. By applying different strain rates, it is possible to simplify Equation 1 to

$$\frac{\dot{\gamma}'}{\dot{\gamma}} = \frac{n'\gamma_0' \sinh\left(\frac{\tau'\gamma_0' v_0}{kT}\right)}{n\gamma_0 \sinh\left(\frac{\tau\gamma_0 v_0}{kT}\right)} \tag{D.2}$$

where the variables with and without prime are measured for two different strain rates. Therefore, strain rate jump tests were conducted at different temperatures. In Figure D.2 measurements of Zr-MG at two different temperatures are shown. Hardness (H), Young's modulus (E), and load are plotted as a function of indentation depth. Blue, dashed lines mark the different strain rates and the respective values are at the top of the figure. In the upper two subplots, hardness and Young's modulus are plotted. The Young's modulus remains constant over the whole indentation depth and the change in the strain rate causes different scattering of the data. At 400 °C, the Young's modulus is slightly decreased compared to 100 °C, but the effect of temperature on hardness is more distinct. Increasing the temperature from 100 °C to 400 °C, leads to a strong decrease in hardness. Additionally, the hardness becomes dependent on the strain rate. This strain rate sensitivity can be deduced from the load-indentation depth curves, where a change in the strain rate causes a change in the slope of the curve. At lower temperature, the BMG shows serrations in the load curve and corresponding boosts and drops in hardness. At 400 °C the curves for the load and the hardness are significantly smoother.

The size and number of the serrations decrease with increasing temperature. For further evaluation, the shear strain of one flow unit is calculated from $\gamma_0 = d_s/h$, where the definition of d_s and h are given in Figure D.2. Yang *et al.* showed that the serration size depends linearly on the indentation depth [48]. Therefore, d_s was not measured at small indentation depths, as the resolution of the instruments is probably not high enough for distinctive shear bands. Also the distance between two serrations (in Figure D.2 the distance between two neighboring red dots) depends directly on the indentation depth. In c and f,

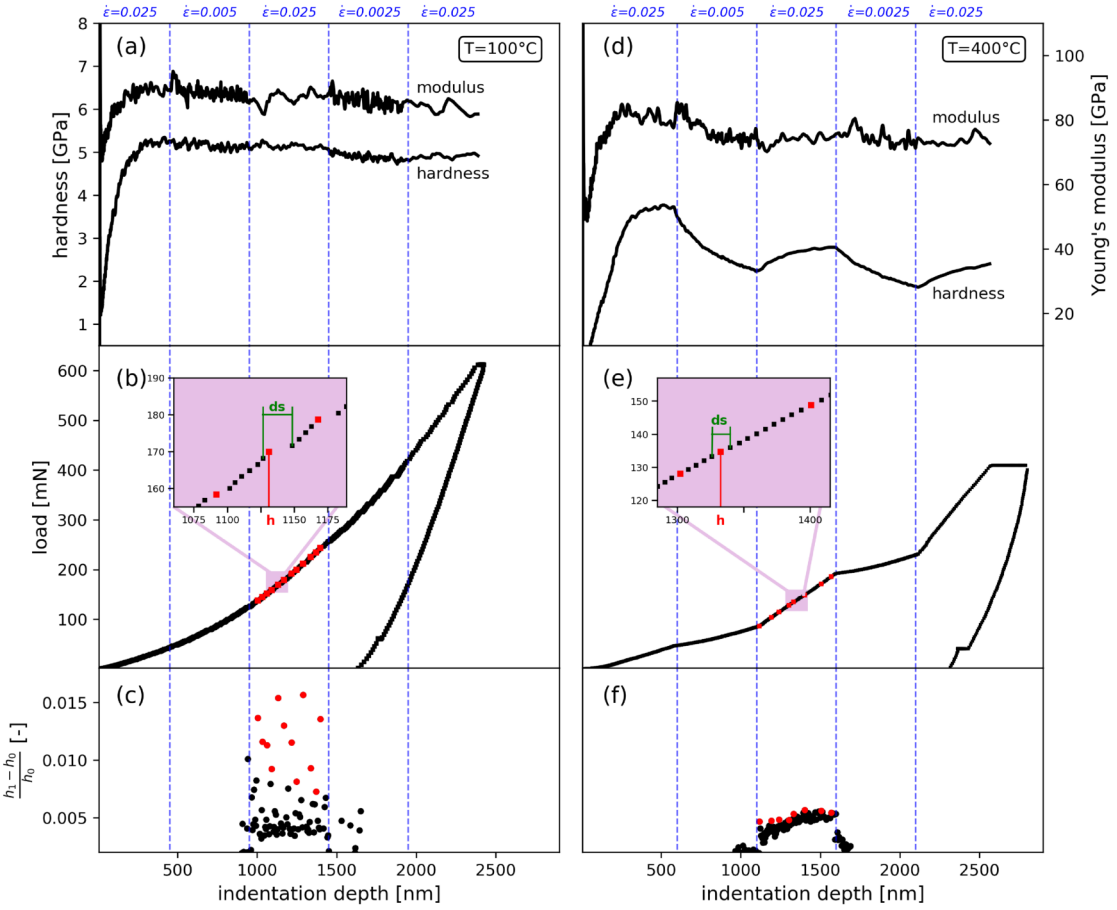

Figure D.2.: (a and d) Hardness, Young's modulus and (b and e) load as a function of indentation depth for two representative strain rate jump test for Zr-MG at two different temperatures (100 °C on the left and 400 °C on the right). One indent was conducted with three different strain rates (0.025 s^{-1}, 0.005 s^{-1} and 0.0025 s^{-1}) over the course of 5 segments, which illustrate the temperature dependent hardness and serration behavior. The determination of serration size and serration position can be found in (c and f) and the two inlets.

the distance of two neighboring data points divided by the indentation depth is plotted as a function of the indentation depth. Most of the data points have similar distances to their neighboring ones, but obviously each serration increases the distance. Therefore, data points showing extrema in the neighboring distance are used to determine d_s. Additionally, the linear dependence of the serration size on the indentation depth is used to calculate the concentration of serrations as the distribution of serrations follows a geometric progression with

$$h_n = h_0(1 + \overline{q})^n \tag{D.3}$$

$$\overline{q} = \frac{1}{n}\sum_{i=1}^{m}\frac{h_i - h_{i-1}}{h_i} \tag{D.4}$$

$\overline{q}$ can be estimated from Figure D.2, and to obtain a concentration, n for $h = \sqrt[3]{3/24.5}m^3$ is calculated. h is the height of a pyramid formed as Berkovich indenter with a volume of $1\,\mathrm{m}^3$.
For solving Equation 2, only the shear stress is missing. Tabor already estimated that the hardness correlates to the strength by a factor of 3 [49]. To take into account the change from a more elastic to a more plastic behavior, a method recently refined by Leitner *et al.* was used [50]. The fraction of plastic deformation can be estimated from the nanoindentation test carried out in CSM mode and is used to calculate the constraint factor, c^*, which varies between 1 and 2.91. The constraint factor depends on the testing temperature and was used to estimate τ from the measured hardness for all strain rates.

$$\tau = \frac{H}{c\sqrt{3}} \tag{D.5}$$

To verify this approach, the activation volume calculated for a Cu sample was tested via the method proposed here and was compared to the accepted method with strain rate sensitivity [51]. The calculated activations volumes are $294 \pm 21\,\mathrm{b}^3$ and $324 \pm 50\,\mathrm{b}^3$ ($b = 0.2555\,\mathrm{nm}$, burgers vector for Cu), respectively. For calculating the activation energy only the jump frequency of the atoms is missing. This can be estimated by approximating each atom as a harmonic oscillator with an energy of $E = 3kT$ and taking the maximal displacement Δx at each temperature via the thermal expansion of the materials ($\Delta x = \alpha r \Delta T$, with r as the atomic

radius). The frequency k_a is then calculated with the atomic mass, m, by

$$k_a = \sqrt{\frac{6k}{mT}} * \frac{1}{2\pi\alpha r} \tag{D.6}$$

The calculated frequencies are just an estimation, because only the main elements of the glasses were taken into the account for atomic mass and radius, and additionally, the thermal expansion changes drastically as soon as T_g is approached [52–54]. However, the calculated values are in the range of $10^{13}\,\mathrm{s}^{-1}$ as expected and show a falling tendency with temperature.

D.3.2. Influences of the temperature

Three to four indentations were performed at each testing temperature and mean values were used for calculation. For some materials more than one sample was tested to validate the repeatability of the data evaluation and once more, only their mean value was used furthermore. In Figure D.3, the concentration of the flow units (a-c) and their shear strain (d-f) are plotted for all three strain rates as a function of temperature. For smaller strain rates, the concentration of flow units is higher, but the local shearing is less (d_s/h). At temperatures approaching the glass transition temperature, the concentration of flow units for small strain rates decreases and approaches the value of the highest strain rate. On the contrary, d_s/h decreases for higher strain rates as the temperature comes into the range of glass transition.

In Figure D.4 d-f, hardness and Young's modulus are plotted versus the testing temperature. The Young's modulus of Ni-MG and the composite Ni-MG 30wt% Zr-MG (c) stay nearly constant even at high temperatures. Moreover, only a slight softening is observed. The softening of Zr-MG (b) and ZrBe-MG (a) is more pronounced especially for the latter, because the testing temperature exceeds their T_g. The Young's modulus decreases slightly with increasing testing temperature for both Zr-based MGs and again it is more pronounced for ZrBe-MG. For the composite Zr-MG 20wt% Cu, values and behavior of hardness and Young's modulus are nearly identical to the ones of the single phase Zr-MG. Zr-MG 80wt% Cu shows the drop in hardness and Young's modulus already at 200 °C. Activation volume and activation energy are plotted in Figure D.4 a-c. The

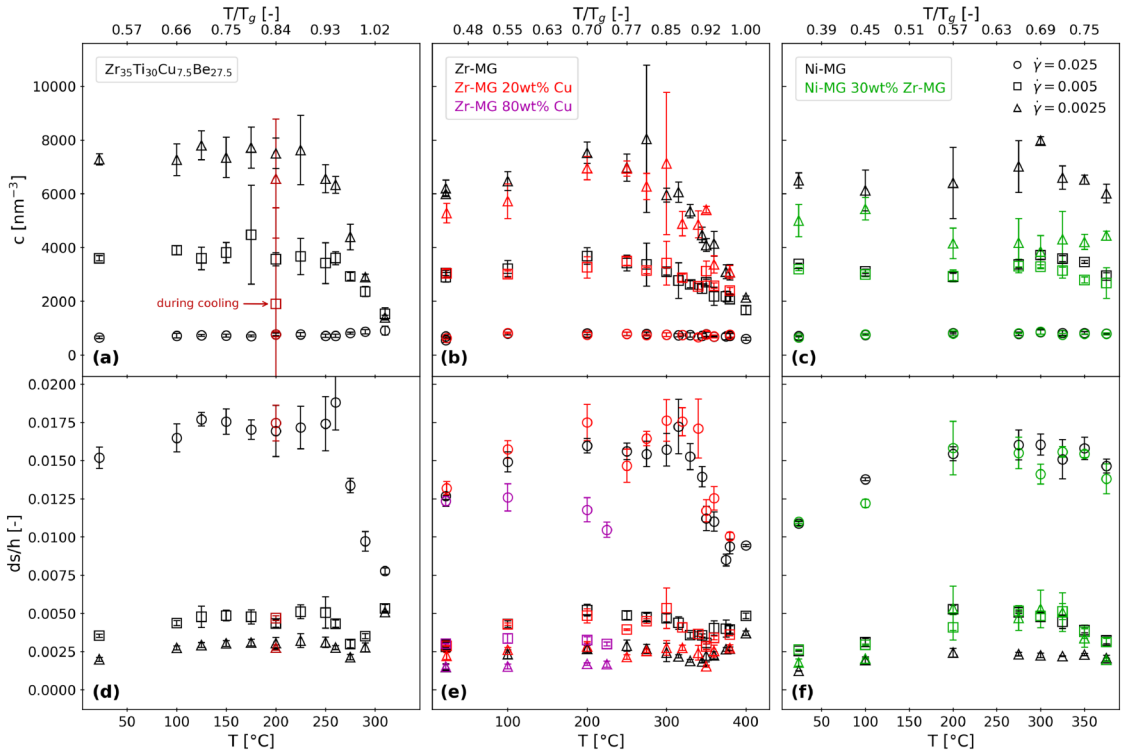

Figure D.3.: Concentration and normalized size of serrations as a function of the indentation temperature. The concentration and shear strain of the flow units depends on the strain rate. Higher strain rates lead to less activated flow units, and higher shear strains per unit. For lower strain rates the situation is reversed.

activation volume for all tested materials stays constant as a function of the temperature until T_g is approached. Then the activation volume increases drastically and for ZrBe-MG (a) an increases of 20 times for a temperature increase of 20 °C is observed. For Zr-MG and Zr-MG 20wt% Cu (b), the curve looks similar as ZrBe-MG, but the change is more moderate. Zr-MG 80wt% Cu already shows an decrease in hardness at temperatures above 200 °C, but as the samples were heavily oxidized, no measurements at higher temperatures could be conducted. Ni-MG and Ni-MG 30wt% Zr-MG (c) show no increase in the activation volume and their activation energy increases steadily with temperature. It should be noticed that Ni-MG has a higher $T_g = 573\,°C$ [55] than the highest possible testing temperature. Their activation energy increases steadily with temperature. ZrBe-MG shows lower ΔG at T_g than Zr-MG, and ΔG of Ni-MG is already higher even though the homologous temperature is lower. The activation energy of the composites matches the respective single phased BMGs.

D.3.3. The influence of the applied strain during HPT

ZrBe-MG was deformed via HPT for 15 rotations. By testing at different radii, the material with varying applied strains was probed. In Table 1, Young's modulus, hardness, activation volume, and activation energy of ZrBe-MG at room temperature for three different applied strains are listed. Young's modulus and hardness are slightly increased, but the activation volume and energy show no clear trend. Therefore, it must be concluded that no significant changes are detectable.

Table D.1.: Young's modulus, hardness, activation volume and activation Energy of ZrBe MG subjected to HPT. No distinctive changes due to the applied shear strain is visible and even the variation of the activation volumes remain very small, especially compared to the changes at higher temperature.

applied shear strain	$E[GPa]$	$H[GPa]$	$v_0[nm^3]$	$\Delta G[kJ/mol]$
0	102.6 ± 1.4	6.07 ± 0.09	0.21 ± 0.03	60 ± 1
125	110.1 ± 1.5	6.15 ± 0.06	0.27 ± 0.02	58.6 ± 0.4
500	109.3 ± 1.5	6.19 ± 0.2	0.11 ± 0.02	62.6 ± 0.9

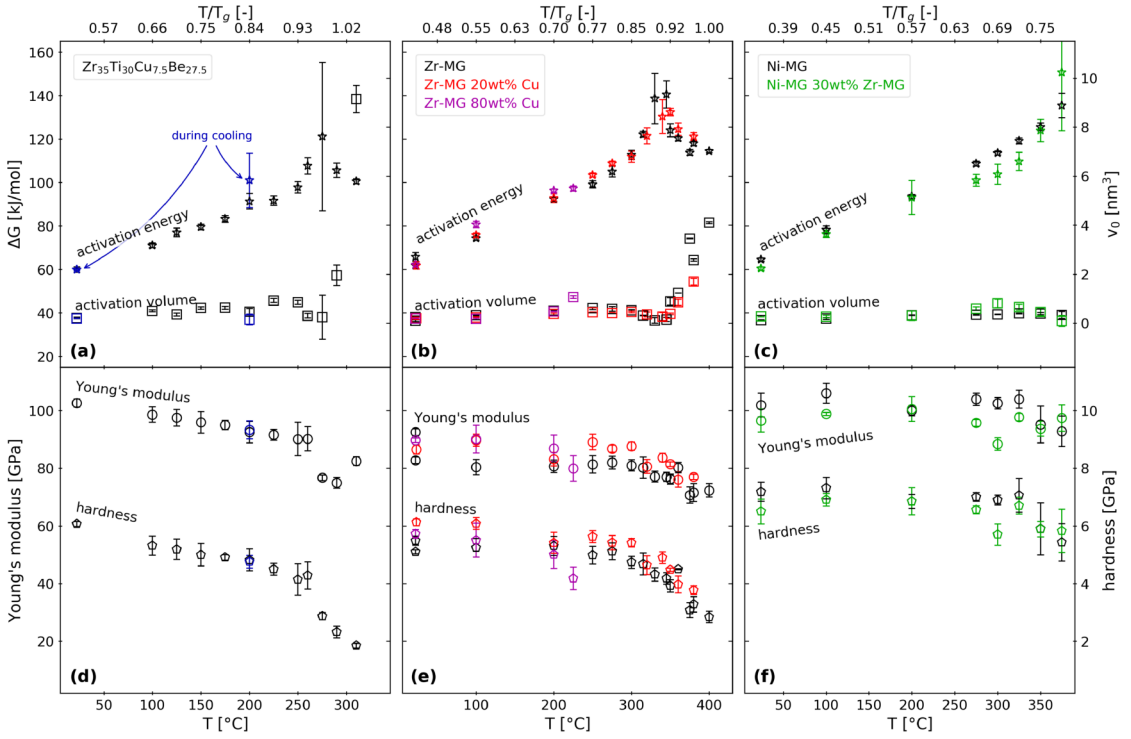

Figure D.4.: Activation energy, volume, Young's modulus and hardness are plotted as function of temperature for three different BMGs and three different BMGCs. The respective homologous temperature is indicated on the top x-axis. Hardness and Young's modulus decrease with increasing temperature, more steeply at T approaching T_g. The activation stays nearly constant up to T_g and then shows a strong increase. The activation energy increases until T_g is reached and subsequently drops.

D.3.4. Influence of thermal cycling

In Figure D.5, hardness, Young's modulus and activation volume of thermally cycled specimens are shown. A variation depending on the number of cycles can be seen, but the changes are small and no clear trend is evident. Ni-MG shows a minimum in hardness at 2 cycles, no change in the Young's modulus and a more random behavior for the activation volume. Zr-MG shows a minimum in hardness at 10 cycles, a minimum in Young's modulus for 5 cycles and two plateaus with the transition between 5 and 10 cycles for the activation volume.

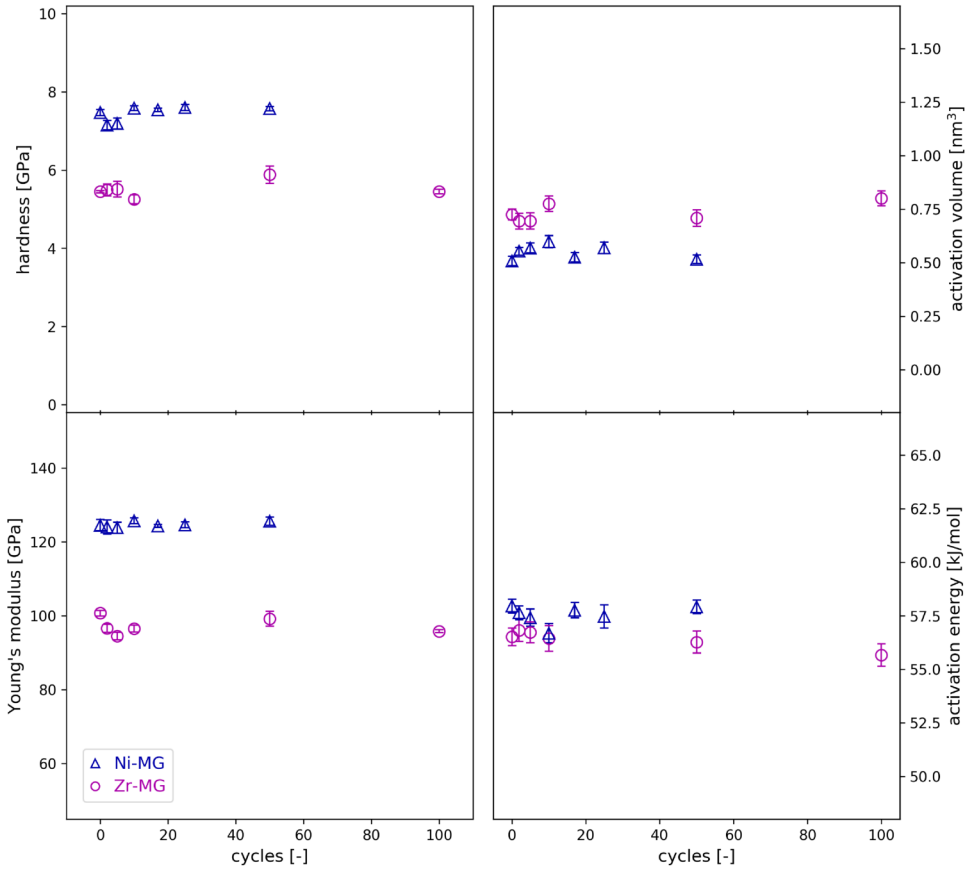

Figure D.5.: Young's modulus, hardness, activation energy, and activation volume as functions of the number of thermal cycles. Zr-MG and Ni-MG sample were thermally cycled between room temperature and liquid nitrogen. No distinctive influences from the number of cycles is detectable.

D.4. Discussion

Three different BMGs with different glass transition temperatures (ZrBe-MG: 290 °C, Zr-MG: 403 °C and Ni-MG: 573 °C) and three BMGCs were investigated at different temperatures. Temperature strongly influences hardness, Young's modulus, and activation energy for all materials. A pronounced effect on the activation volume can be see for materials, which have a lower T_g than the maximal testing temperature. This could not be observed for Ni-MG and Ni-MG 30wt% Zr-MG, because the testing temperature does not exceed T_g. For all other materials a pronounced change of the properties correlating with a change in the slope of the curve for all measured and calculated properties can be observed at T_g. Hardness and Young's modulus decrease stronger at temperature higher T_g. The activation volume increases slowly when approaching T_g, but at higher temperatures v_0 increases with a very high rate. In [34, 56–59] similar values of several atomic volumes for the activation volumes at room temperature are shown. The activation energy shows also an increase for temperature below T_g, but decreases and levels off exceeding this temperature. The increase of activation energy was already shown in former studies by means of DSC measurements with different heating rates [60–62] and dilatometer experiments combined with synchrotron measurements[13]. Changes in the activation energy mean a change in the deformation behavior. Considering the flow units in metallic glasses as shear transformation zones (STZ), diffusion processes are likely to govern shear related deformation. At low temperatures, the activation volumes are small and so few atoms are sufficient. It is probable that mainly smaller atoms will contribute, which have a higher diffusivity and therefore, the activation energy needed will be lower. Increasing the activation volume forces more atoms to participate and larger atoms with lower diffusivity will therefore increase the activation energy. Above the glass transition temperature, the diffusion mechanism changes from diffusion in a solid to diffusion in a viscous-liquid [63, 64]. The consequence is an increase in activation volume and decrease in activation energy as seen in Figure D.4. Looking at the homologous temperature, all materials behave similarly. The absolute values differ, as varying composition leads to a change in diffusion constants, but the number of participating atoms governs the main behavior from a strict solid diffusion to liquid diffusion at temperatures higher than T_g. Two of the BMGCs (Zr-MG 20wt% Cu and Ni-MG 30wt% Zr-MG) show nearly identical values to the respective BMG. Since very fine microstructures were tested where

the minor phases already is partly dissolved [10, 11], the properties of the major phase dominate. A shift of T_g is probable, because the composition is changed, but it is maybe too small to effectively change the behavior at the investigated temperatures. Furthermore, the technique used mainly tests the initiation of the deformation. Influences from phase boundaries should be investigated by other techniques, such as compression tests. The specimen with the highest percentage of Cu (Zr-MG 80wt% Cu) and a coarser microstructure does show lower transition temperatures, but heavy oxidization during high temperature testing prevents a clear conclusion. In summary, the fabrication method does not influence the deformation behavior of the BMGs. BMG fabricated via HPT and cast ones show nearly the same activation volumes and energies at room temperature. To investigate rejuvenated MGs, HPT-deformation (Table 1) and thermal cycling (Figure D.5) was used, but no clear influence on activation energy and volume is detectable. In the literature, effects such as reduction in hardness and increase in the free volume are shown for some compositions. One explanation that nanoindentation does not show a difference for rejuvenated samples, is a heterogeneous distribution of free volume for instance. The small testing volume of nanoindentation (one indent probes only approximately 1 µm^3 to 100 µm^3) can make the detection difficult compared to methods which probe the whole specimens or larger volumes.

D.5. Conclusion

Three different BMGs (ZrBe-MG, Zr-MG and Ni-MG) and three composites (Zr-MG 20wt% Cu, Zr-MG 80wt% Cu and Ni-MG 30wt% Zr-MG) were investigated by nanoindentation strain rate jump testing. In order to obtain different material states (as-casted, HPT-deformed, additional thermal cycling), the BMGs were subjected to high pressure torsion as well as thermal cycling. Additional nanoindentation tests were conducted at higher testing temperature up to 430 °C. The main findings can be summarized by 5 points:

1. Nanoindentation strain rate jump tests can be used for estimating the activation volume and activation energy of BMGs.
2. The temperature has a great influence on the mechanical properties, especially when T_g is approached. All materials show a decrease in hardness

and Young's modulus with increasing temperature and a drop in hardness when T_g is reached. The activation volume is stable at temperatures well below T_g and a strong increase is observed for temperatures near and higher than T_g. The activation energy increases up to Tg, but decreases again at higher temperatures. This is caused by a change in the diffusion mechanism. Below T_g solid diffusion with increasing number of participating atoms occurs and as T_g is exceeded, it changes to liquid diffusion.

3. The fabrication route does not significantly influence the activation volume and energy. The three BMGs behave similarly and onset temperatures of property changes accordingly to the respective T_g. Two of the composites (Zr-MG 20wt% Cu and Ni-MG 30wt% Zr-MG) behave like their main component, but Zr-MG 80wt% Cu seems to show a derivation of its behavior with an earlier onset of softening and increasing of activation volume. Due to strong oxidization, it is not possible to draw a definite conclusion for this case.
4. High pressure torsion causes no significant changes in hardness, Young's modulus and activation volume.
5. Thermal cycling weakly influences hardness and Young's modulus, but no significant change of the activation volume has been detected.

In conclusion, the activation volume and energy of different BMGs is mainly influenced by temperature and the selected composition, whereas thermal cycling or high-pressure torsion show no significant influence.

Acknowledgments

We want to thank Alexander Leitner for the fruitful discussions and help in determining the constraint factors, and Jan Schroers and Liquidmetal® Technologies to supply us the ZrBe-BMG. The European Research Council under ERC Grant Agreement No. 3401 85 USMS has provided funding for this work. The financial support by the Austrian Federal Government (837900) within the framework of the COMET Funding Program (MPPE, A7.19) is highly appreciated.

D.6. References

[1] P. Murali and U. Ramamurty. "Embrittlement of a bulk metallic glass due to sub-T_g annealing." In: *Acta Materialia* 53.5 (2005), pp. 1467–1478. DOI: 10.1016/j.actamat.2004.11.040 (cit. on p. 118).

[2] Y. Q. Cheng and E. Ma. "Intrinsic shear strength of metallic glass." In: *Acta Materialia* 59.4 (2011), pp. 1800–1807. DOI: 10.1016/j.actamat.2010.11.046 (cit. on p. 118).

[3] D. V. Louzguine-Luzgin et al. "Influence of cyclic loading on the onset of failure in a Zr-based bulk metallic glass." In: *Journal of Materials Science* 49.19 (2014), pp. 6716–6721. DOI: 10.1007/s10853-014-8276-2 (cit. on p. 118).

[4] S. V. Ketov et al. "Rejuvenation of metallic glasses by non-affine thermal strain." In: *Nature* 524.7564 (2015), pp. 200–203. DOI: 10.1038/nature14674 (cit. on p. 118).

[5] F. Meng et al. "Reversible transition of deformation mode by structural rejuvenation and relaxation in bulk metallic glass." In: *Applied Physics Letters* 101.12 (2012), p. 121914. DOI: 10.1063/1.4753998 (cit. on p. 118).

[6] X. D. Wang et al. "Atomic-level structural modifications induced by severe plastic shear deformation in bulk metallic glasses." In: *Scripta Materialia* 64.1 (2011), pp. 81–84. DOI: 10.1016/j.scriptamat.2010.09.015 (cit. on p. 118).

[7] J. Pan et al. "Extreme rejuvenation and softening in a bulk metallic glass." In: *Nature Communications* 9.1 (2018). DOI: 10.1038/s41467-018-02943-4 (cit. on p. 118).

[8] A. Hohenwarter et al. "Technical parameters affecting grain refinement by high pressure torsion." In: *International Journal of Materials Research* 100.12 (2009), pp. 1653–1661. DOI: 10.3139/146.110224 (cit. on p. 118).

[9] A. Vorhauer and R. Pippan. "On the homogeneity of deformation by high pressure torsion." In: *Scripta Materialia* 51.9 (2004), pp. 921–925. DOI: 10.1016/j.scriptamat.2004.04.025 (cit. on p. 118).

[10] L. Krämer, Y. Champion, and R. Pippan. "From powders to bulk metallic glass composites." In: *Scientific Reports* 7.1 (2017). DOI: 10.1038/s41598-017-06424-4 (cit. on pp. 118, 119, 132).

[11] L. Krämer et al. "Bulk metallic dual phase glasses by severe plastic deformation." In: *Intermetallics* 94 (2018), pp. 172–178. DOI: 10.1016/j.intermet.2017.12.005 (cit. on pp. 118, 119, 132).

[12] L. Krämer et al. "Production of Bulk Metallic Glasses by Severe Plastic Deformation." In: *Metals* 5.2 (2015), p. 720. DOI: 10.3390/met5020720 (cit. on pp. 118–120).

[13] A. R. Yavari et al. "Excess free volume in metallic glasses measured by X-ray diffraction." In: *Acta Materialia* 53.6 (2005), pp. 1611–1619. DOI: 10.1016/j.actamat.2004.12.011 (cit. on pp. 118, 131).

[14] N. Mattern et al. "Structural evolution of Cu–Zr metallic glasses under tension." In: *Acta Materialia* 57.14 (2009), pp. 4133–4139. DOI: 10.1016/j.actamat.2009.05.011 (cit. on p. 118).

[15] K. M. Flores et al. "Characterization of Free Volume in a Bulk Metallic Glass Using Positron Annihilation Spectroscopy." In: *Journal of Materials Research* 17.05 (2002), pp. 1153–1161. DOI: 10.1557/jmr.2002.0171 (cit. on p. 118).

[16] Q. P. Cao et al. "Free-volume evolution and its temperature dependence during rolling of Cu60Zr20Ti20 bulk metallic glass." In: *Applied Physics Letters* 87.10 (2005), p. 101901. DOI: 10.1063/1.2037858 (cit. on p. 118).

[17] V. Maier et al. "Nanoindentation strain-rate jump tests for determining the local strain-rate sensitivity in nanocrystalline Ni and ultrafine-grained Al." In: *Journal of Materials Research* 26.11 (2011), pp. 1421–1430. DOI: 10.1557/jmr.2011.156 (cit. on pp. 118, 121).

[18] J. M. Wheeler et al. "Activation parameters for deformation of ultrafine-grained aluminium as determined by indentation strain rate jumps at elevated temperature." In: *Materials Science and Engineering: A* 585 (2013), pp. 108–113. DOI: 10.1016/j.msea.2013.07.033 (cit. on p. 118).

[19] W. J. Wright, R. Saha, and W. D. Nix. "Deformation Mechanisms of the $Zr_{40}Ti_{14}Ni_{10}Cu_{12}Be_{24}$ Bulk Metallic Glass." In: *MATERIALS TRANSACTIONS* 42.4 (2001), pp. 642–649. DOI: 10.2320/matertrans.42.642 (cit. on p. 118).

[20] C. A. Schuh and T. G. Nieh. "A nanoindentation study of serrated flow in bulk metallic glasses." In: *Acta Materialia* 51.1 (2003), pp. 87–99. DOI: 10.1016/s1359-6454(02)00303-8 (cit. on p. 118).

[21] C. A. Schuh, A. C. Lund, and T. G. Nieh. "New regime of homogeneous flow in the deformation map of metallic glasses: elevated temperature nanoindentation experiments and mechanistic modeling." In: *Acta Materialia* 52.20 (2004), pp. 5879–5891. DOI: 10.1016/j.actamat.2004.09.005 (cit. on p. 118).

[22] L. Cheng et al. "Serrated flow behaviors of a Zr-based bulk metallic glass by nanoindentation." In: *Journal of Applied Physics* 115.8 (2014), p. 084907. DOI: 10.1063/1.4866874 (cit. on p. 118).

[23] W. Liang et al. "Plastic deformation behaviors of Ni- and Zr-based bulk metallic glasses subjected to nanoindentation." In: *Materials Characterization* 86 (2013), pp. 290–295. DOI: 10.1016/j.matchar.2013.10.014 (cit. on p. 118).

[24] C. Schuh, T. Hufnagel, and U. Ramamurty. "Mechanical behavior of amorphous alloys." In: *Acta Materialia* 55.12 (2007), pp. 4067–4109. DOI: 10.1016/j.actamat.2007.01.052 (cit. on p. 118).

[25] T. Burgess, K. J. Laws, and M. Ferry. "Effect of loading rate on the serrated flow of a bulk metallic glass during nanoindentation." In: *Acta Materialia* 56.17 (2008), pp. 4829–4835. DOI: 10.1016/j.actamat.2008.05.039 (cit. on p. 118).

[26] F. Haag et al. "Influences of residual stresses on the serrated flow in bulk metallic glass under elastostatic four-point bending – A nanoindentation and atomic force microscopy study." In: *Acta Materialia* 70 (2014), pp. 188–197. DOI: 10.1016/j.actamat.2014.01.053 (cit. on p. 118).

[27] H. Huang et al. "Effects of pre-compression deformation on nanoindentation response of $Zr_{65}Cu_{15}Al_{10}Ni_{10}$ bulk metallic glass." In: *Journal of Alloys and Compounds* 674 (2016), pp. 223–228. DOI: 10.1016/j.jallcom.2016.03.057 (cit. on p. 118).

[28] R. Limbach et al. "Serrated flow of CuZr-based bulk metallic glasses probed by nanoindentation: Role of the activation barrier, size and distribution of shear transformation zones." In: *Journal of Non-Crystalline Solids* 459 (2017), pp. 130–141. DOI: 10.1016/j.jnoncrysol.2017.01.015 (cit. on p. 119).

[29] I.-C. Choi et al. "Estimation of the shear transformation zone size in a bulk metallic glass through statistical analysis of the first pop-in stresses during

spherical nanoindentation." In: *Scripta Materialia* 66.11 (2012), pp. 923–926. DOI: 10.1016/j.scriptamat.2012.02.032 (cit. on p. 119).

[30] J. P. Coleman et al. "Effect of annealing on nanoindentation slips in a bulk metallic glass." In: *Physical Review B* 96.13 (2017). DOI: 10.1103/physrevb.96.134117 (cit. on p. 119).

[31] N. Thurieau et al. "Activation volume in heterogeneous deformation of $Mg_{65}Cu_{12.5}Ni_{12.5}(Ce_{75}La_{25})_{10}$ metallic glass." In: *Journal of Applied Physics* 118.20 (2015), p. 204302. DOI: 10.1063/1.4936220 (cit. on p. 119).

[32] J. D. Ju et al. "An atomically quantized hierarchy of shear transformation zones in a metallic glass." In: *Journal of Applied Physics* 109.5 (2011), p. 053522. DOI: 10.1063/1.3552300 (cit. on p. 119).

[33] M. Bletry et al. "Homogeneous deformation of bulk metallic glasses in the super-cooled liquid state." In: *Materials Science and Engineering: A* 387-389 (2004), pp. 1005–1011. DOI: 10.1016/j.msea.2004.02.085 (cit. on p. 119).

[34] F. Jiang et al. "Shear transformation zone volume determining ductile–brittle transition of bulk metallic glasses." In: *Acta Materialia* 59.5 (2011), pp. 2057–2068. DOI: 10.1016/j.actamat.2010.12.006 (cit. on pp. 119, 131).

[35] G. Duan et al. "Bulk Metallic Glass with Benchmark Thermoplastic Processability." In: *Advanced Materials* 19.23 (2007), pp. 4272–4275. DOI: 10.1002/adma.200700969 (cit. on p. 119).

[36] B. Sarac et al. "Honeycomb Structures of Bulk Metallic Glasses." In: *Advanced Functional Materials* 22.15 (2012), pp. 3161–3169. DOI: 10.1002/adfm.201200539 (cit. on p. 119).

[37] B. Sarac and J. Schroers. "Designing tensile ductility in metallic glasses." In: *Nature Communications* 4 (2013). DOI: 10.1038/ncomms3158 (cit. on p. 119).

[38] L. Perrière and Y. Champion. "Phases distribution dependent strength in metallic glass – aluminium composites prepared by spark plasma sintering." In: *Materials Science & Engineering A* 548 (2012), pp. 112–117. DOI: 10.1016/j.msea.2012.03.100 (cit. on p. 119).

[39] X. Wang et al. "Production of Bulk Glassy Alloy Parts by a Levitation Melting-Forging Method." In: *Materials Transactions* 47.8 (2006), pp. 2072–2075. DOI: 10.2320/matertrans.47.2072 (cit. on p. 120).

[40] N. M. Everitt, M. I. Davies, and J. F. Smith. "High temperature nanoindentation – the importance of isothermal contact." In: *Philosophical Magazine* 91.7-9 (2011), pp. 1221–1244. DOI: 10.1080/14786435.2010.496745 (cit. on p. 121).

[41] J. M. Wheeler and J. Michler. "Invited Article: Indenter materials for high temperature nanoindentation." In: *Review of Scientific Instruments* 84.10 (2013), p. 101301. DOI: 10.1063/1.4824710 (cit. on p. 121).

[42] B. N. Lucas and W. C. Oliver. "Indentation power-law creep of high-purity indium." In: *Metallurgical and Materials Transactions A* 30.3 (1999), pp. 601–610. DOI: 10.1007/s11661-999-0051-7 (cit. on p. 121).

[43] V. Maier et al. "Thermally activated deformation processes in body-centered cubic Cr – How microstructure influences strain-rate sensitivity." In: *Scripta Materialia* 106 (2015), pp. 42–45. DOI: 10.1016/j.scriptamat.2015.05.001 (cit. on p. 121).

[44] G. M. Pharr, J. H. Strader, and W. C. Oliver. "Critical issues in making small-depth mechanical property measurements by nanoindentation with continuous stiffness measurement." In: *Journal of Materials Research* 24.03 (2009), pp. 653–666. DOI: 10.1557/jmr.2009.0096 (cit. on p. 122).

[45] W. C. Oliver and G. M. Pharr. "An improved technique for determining hardness and elastic modulus using load and displacement sensing indentation experiments." In: *Journal of Materials Research* 7.06 (1992), pp. 1564–1583. DOI: 10.1557/jmr.1992.1564 (cit. on p. 122).

[46] F. Spaepen. *Defects in amorphous metals*. Technical Report 16. Office of naval research, 1982 (cit. on p. 122).

[47] J. S. Langer. "Shear-transformation-zone theory of plastic deformation near the glass transition." In: *Physical Review E* 77.2 (2008). DOI: 10.1103/physreve.77.021502 (cit. on p. 123).

[48] B. Yang and T. Nieh. "Effect of the nanoindentation rate on the shear band formation in an Au-based bulk metallic glass." In: *Acta Materialia* 55.1 (2007), pp. 295–300. DOI: 10.1016/j.actamat.2006.08.028 (cit. on p. 123).

[49] D. Tabor. "The hardness of solids." In: *Reviews of Physics in Technology* 1.3 (1970), pp. 145–179. DOI: 10.1088/0034-6683/1/3/i01 (cit. on p. 125).

[50] A. Leitner, V. Maier-Kiener, and D. Kiener. "Essential refinements of spherical nanoindentation protocols for the reliable determination of mechanical flow curves." In: *Materials & Design* 146 (2018), pp. 69–80. DOI: 10.1016/j.matdes.2018.03.003 (cit. on p. 125).

[51] W. Blum. "Discussion: Activation volumes of plastic deformation of crystals." In: *Scripta Materialia* 146 (2018), pp. 27–30. DOI: 10.1016/j.scriptamat.2017.10.029 (cit. on p. 125).

[52] M. Q. Jiang et al. "Thermal expansion accompanying the glass-liquid transition and crystallization." In: *AIP Advances* 5.12 (2015), p. 127133. DOI: 10.1063/1.4939216 (cit. on p. 126).

[53] E. Pineda et al. "Structural study of conventional and bulk metallic glasses during annealing." In: *Journal of Alloys and Compounds* 483.1-2 (2009), pp. 578–581. DOI: 10.1016/j.jallcom.2008.07.194 (cit. on p. 126).

[54] A. R. Yavari et al. "Change in Thermal Expansion Coefficient of Bulk Metallic Glasses T_g Measured by Real-Time Diffraction Using High-Energy Synchrotron Light." In: *Journal of Metastable and Nanocrystalline Materials* 15-16 (2003), pp. 105–110. DOI: 10.4028/www.scientific.net/jmnm.15-16.105 (cit. on p. 126).

[55] A. P. Wang, T. Zhang, and J. Q. Wang. "Ni-based fully amorphous metallic coating with high corrosion resistance." In: *Philosophical Magazine Letters* 86.1 (2006), pp. 5–11. DOI: 10.1080/09500830500479718 (cit. on p. 128).

[56] Z. Q. Chen et al. "Clarification on shear transformation zone size and its correlation with plasticity for Zr-based bulk metallic glass in different structural states." In: *Materials Science and Engineering: A* 677 (2016), pp. 349–355. DOI: 10.1016/j.msea.2016.09.054 (cit. on p. 131).

[57] F. Spaepen. "Homogeneous flow of metallic glasses: A free volume perspective." In: *Scripta Materialia* 54.3 (2006), pp. 363–367. DOI: 10.1016/j.scriptamat.2005.09.046 (cit. on p. 131).

[58] P. de Hey, J. Sietsma, and A. van den Beukel. "Structural disordering in amorphous $Pd_{40}Ni_{40}P_{20}$ induced by high temperature deformation." In: *Acta Materialia* 46.16 (1998), pp. 5873–5882. DOI: 10.1016/s1359-6454(98)00234-1 (cit. on p. 131).

[59] P. Schall, D. A. Weitz, and F. Spaepen. "Structural Rearrangements That Govern Flow in Colloidal Glasses." In: *Science* 318.5858 (2007), pp. 1895–1899. DOI: 10.1126/science.1149308 (cit. on p. 131).

[60] A. Cai et al. "A Series of Zr-Based Bulk Metallic Glasses with Room Temperature Plasticity." In: *Materials* 9.6 (2016), p. 408. DOI: 10.3390/ma9060408 (cit. on p. 131).

[61] S.-X. Wang, S.-G. Quan, and C. Dong. "Kinetic of glass transition of $Zr_{57.2}Al_{21.4}Ni_{21.4}$ bulk metallic glass." In: *Thermochimica Acta* 532 (2012), pp. 92–95. DOI: 10.1016/j.tca.2010.12.005 (cit. on p. 131).

[62] K. Knorr et al. "Self-diffusion in the amorphous and supercooled liquid state of the bulk metallic glass Zr46.75Ti8.25Cu7.5Ni10Be27.5." In: *Journal of Non-Crystalline Solids* 250-252 (1999), pp. 669–673. DOI: 10.1016/s0022-3093(99)00157-x (cit. on p. 131).

[63] U. Geyer et al. "Atomic Diffusion in the Supercooled Liquid and Glassy States of the $Zr_{41.2}Ti_{13.8}Cu_{12.5}Ni_{10}Be_{22.5}$ Alloy." In: *Physical Review Letters* 75.12 (1995), pp. 2364–2367. DOI: 10.1103/physrevlett.75.2364 (cit. on p. 131).

[64] X.-P. Tang et al. "Diffusion mechanisms in metallic supercooled liquids and glasses." In: *Nature* 402.6758 (1999), pp. 160–162. DOI: 10.1038/45996 (cit. on p. 131).

E. Micropillar compression testing of bulk metallic glass composites

Lisa Krämer [1], Marlene Kapp[1], Markus Alfreider[2] and Reinhard Pippan [1]

[1] Erich Schmid Institute of materials science, Austrian Academy of Science, Leoben, Austria
[2] Department of Materials Physics, Montanuniversität Leoben, Leoben, Austria

Abstract. Bulk metallic glasses and bulk metallic glass composites containing either two amorphous or an amorphous and a crystalline phase were fabricated via high pressure torsion. Mechanical properties were investigated by means of micropillar compression tests conducted in-situ in a scanning electron microscope (SEM). The deformation properties are strongly influenced by the microstructure, orientation, and the type of the second phase. The deformation behavior is investigated via SEM sequences recorded during testing and additional micrographs afterward. Thereby, plastic deformation before the formation of shear bands and stopping of shear bands have been observed. Even though most pillars fail due to nucleation of a dominate single shear band, also the formation of multiple shear bands a kink band is observed, which increases the ductility enormously.

E.1. Introduction

Bulk metallic glasses (BMGs) have attracted enormous interest over the last decades. On the one hand, their amorphous structure leads to interesting physical and mechanical properties, on the other hand their lack of ductility limits their possible applications. An often performed approach to adjust mechanical properties is adding a second phase. A common practice is the partial crystallization of

a BMG by an additional annealing step or a lower cooling rate [1–6]. The increase of the ductility is mostly determined by the proportion of the crystalline phase, but also a fine, homogeneous distribution is beneficial [7, 8]. Similar results are achieved by adding crystalline fibers, particles or springs during casting [9–13]. The volume fraction of the second phase is one of the most important factors affecting the ductility [11, 14]. To adjust mechanical properties, the second phase can also be amorphous as was shown by fabricating an amorphous/amorphous composite via phase separation [15, 16]. Another option to produce bulk metallic glass composites (BMGCs) is severe plastic deformation, relatively realizing by high pressure torsion (HPT). In this process powders can be used as starting material, which enables a high flexibility in the combination of materials and their respective ratios. Thus, amorphous/crystalline and amorphous/amorphous BMGCs can be fabricated. An additional advantage is the adjustability of the phase sizes by changing the applied strain via the number of rotations. The obtained microstructures can be varied from coarse to fine lamellae and even mixing of the phases is possible [17–22]. Sputtering can also be used to produce nanocrystalline/amorphous multilayers [23–25]. One of the best studied systems contains nanocrystalline Cu and an amorphous CuZr-phase [26]. The thickness of the layers can be changed individually and thereby changes in mechanical properties, such as an increase in ductility and strength, can be investigated [24, 27]. Critical thicknesses for the nucleation of shear bands (SB) in the amorphous layers ($t_{cr} < 20\,\text{nm}$) [28, 29] and for an effective stopping of the SB in the crystalline layer ($t_{cr} > 100\,\text{nm}$) [30] were found by various mechanical experiments. Furthermore, the stress state can be changed by varying the thickness-ratio of the two layers. However, to the authors' knowledge no studies address the influence of the lamellae orientation of this multilayers system, even though a strong dependence can be expected. Micropillar compression tests on nanolamellar pearlite and on nanocrystalline steel showed a change of the deformation behavior from a shear band for lamellae perpendicular to the loading direction, to a dislocation movement parallel to the interfaces (confined layer slip) for inclined lamellae (approximately 45°) and a kink band formation for loading parallel to the lamellae [31].

This study addresses the attention to the effect of orientation of amorphous/amorphous and amorphous/crystalline lamellar structures. The orientation of the lamellae is varied in respect to the loading direction and the lamellae thickness are changed. The lamellar composites are generated via HPT powder consolidation

and deformation.

E.2. Experimental

Two single-phased BMGs (Ni-MG and Zr-MG) and four different BMGCs (Zr-MG 20wt% Cu, Zr-MG 40wt% Cu, Zr-MG 60wt% Cu and Ni-MG 30wt% Zr-MG) were produced starting from powders using HPT for consolidation and deformation to achieve dense bulk samples. This process and the resulting microstructures are described in detail in previous papers[21, 22]. In summary, all composites show an elongation of the powder particles during consolidation, which then evolves to a lamellar microstructure during further HPT deformation. Higher applied shear strain leads to refinement of both phases and even mixing of the two phases is observed. At very high strains a new homogeneous MG phase is generated. In this study, however, only the lamellar composites will be investigated. The obtained microstructure depend on the powder size, the composition and the applied shear strain. The shear strain γ in a HPT deformed sample is given by $\gamma = \frac{2\pi Nr}{t}$, where r is the radius, t is the thickness of the sample and N is the number of turns. For a given sample thickness the strain and therefore the microstructure can be changed either by changing N or r. The amount of deformation during the HPT-process increases gradually with the radius leading to finer microstructures at the edge compared to the center of the specimens. Due to local inhomogeneities in the deformation of the two phases the lamellae spacing and orientation are not as uniform as for the sputtered films. Pillars were positioned at different radii r (Figure E.1 a) to vary the lamellae thickness and in different direction related to the HPT-disc to obtain different lamellar loading orientation. For testing in tangential direction (see Figure E.1 a and c), one half or a quarter of a HPT-disk was ground and polished to a wedge with approximately an opening angle of 10° and a Hitachi E-3500 cross section polisher was used to remove the very thin edge at the front of the wedge. Additionally, pillars in axial direction were produced (see Figure E.1 a and b) by cutting a thin slice with a wire saw, which was ground and polished to a thickness of 100 µm and further partially thinned by the cross section polisher to 30 µm, aiming to reduce the needed time for focused ion beam (FIB) milling. A Zeiss LEO 1540 XB dual beam focused ion beam workstation was used for the final fabrication step. Three different currents (10 nA, 2 nA and 200 pA) were used, whereby the lowest

one to reduces the influence of the ion damage and ensure smooth surfaces. Additionally, the pillars were overtilted by 1.2° to 1.4° for the last cutting step to diminish the taper.

All pillars were approximately $(5 \times 5 \times 10)\,\mu m^3$ in size leading to an aspect ratio of 2 to prevent buckling. A Zeiss LEO1525 SEM was used to investigate the actual microstructure and the precise dimensions of the pillars before testing and to study the deformation and failure behavior in detail after testing. The microcompression tests were conducted in-situ using an ASMEC UNAT micro indenter equipped with diamond flat punch tips (diameter of 15 µm to 20 µm) inside a Zeiss LEO982 SEM. An initial constant strain rate of $10^{-3}\,s^{-1}$ was used and all measurements were done in displacement controlled mode. SEM-micrograph sequences were recorded in-situ to link the mechanical data to the deformation behavior and were also used to measure the drift by comparing the images before loading and after unloading. By measuring the change in length of the pillar over the whole sequence it was possible to calculate the applied strain. The compliance of the set-up was determined by additional loading of the lamellae. Corrected stress-strain curves were calculated using the measured compliance and drift. In Figure E.2 a and b, an uncorrected and a corrected stress-strain curve compared to the calculated strain from the SEM image sequence are shown, respectively. All experimental data shown hereafter is corrected as described.

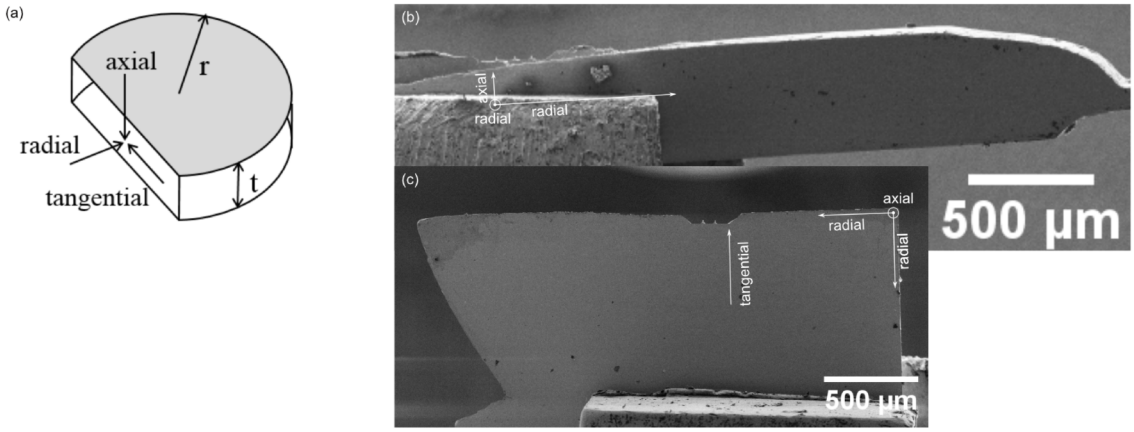

Figure E.1.: (a) Schematic view of a HPT disk indicating the testing directions (axial and tangential) and SEM micrographs of pillars tested axial (b) and tangential (c).

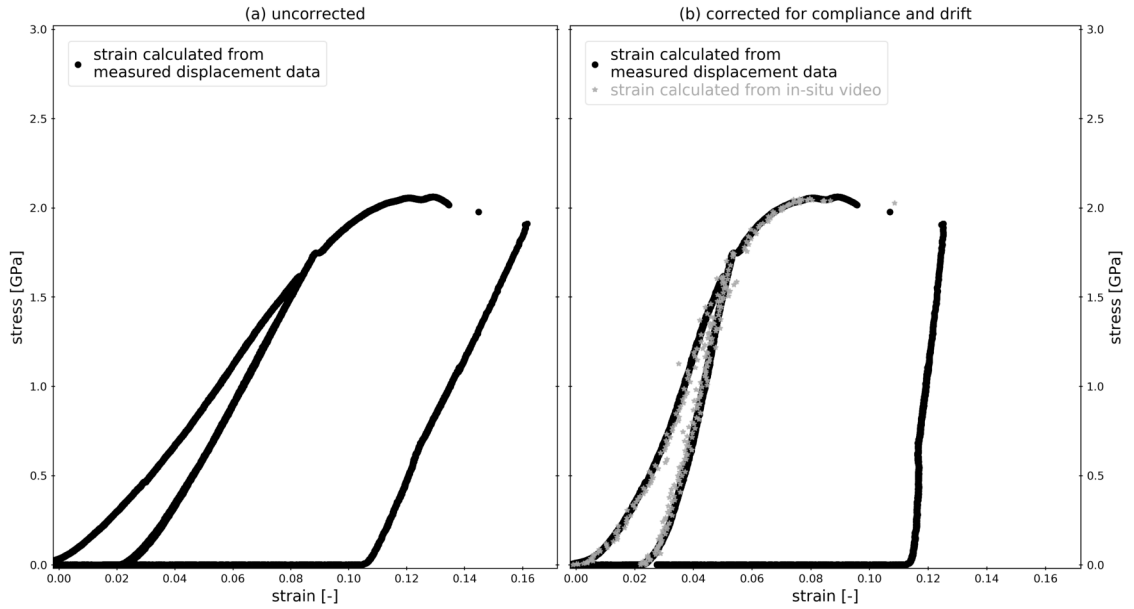

Figure E.2.: Uncorrected (a) and corrected (b) stress-strain curves of micropillar compression tests. The corrected data takes the compliance of the set-up and the drift during the test into account. Strain data calculated from the image sequence agree with the corrected data (b).

E.3. Results

E.3.1. Single-phase metallic glasses

Stress-strain curves of two single phase BMGs generated from MG powders are shown in Figure E.3. Ni-MG (Figure E.3 a) shows small periodic spikes and one is marked with a circle and pointed out by an arrow. These are artifacts and occurring randomly in some measurements. For instance, the measured pillars of Zr-MG (Figure E.3 b) do not show such spikes. They are caused by the testing set-up and do not reflect a material behavior. Therefore, these artefacts are ignored. Another effect can be seen at the beginning of the deformation, where most curves show a low slope caused by a contact problem due to tapered top surface. Both materials show a linear elastic behavior as soon as a full contact between indenter and pillar is reached, which is followed by a step-like deformation ending for three specimens in failure. SEM micrographs taken after testing show in both cases SBs with a similar orientation as the last fatal one. Ni-MG show a stronger branching of the shear bands compared to Zr-MG, which by the number of strain bursts in the stress-strain data. The two BMGs also show a different maximum strength level. Ni-MG fails at approximately 2.8 GPa, whereas Zr-MG fails already at 2.12 GPa.

E.3.2. Bulk metallic glass composites

In Figure E.4, SEM micrographs of the pillars before the compression tests are shown. The top surface of the pillar and two side surface of the pillar from a frontal view can be found in the upper and in the lower row, respectively. Three different compositions of Zr-MG Xwt% Cu (X=20, 40, 60) and one of Ni-MG Ywt% Zr-MG (Y=30) were investigated. The difference in microstructure including phase fractions, lamellae thickness and orientation can be seen for each individual pillar. For Zr-MG 20wt% Cu, four different pillars in tangential direction are shown with microstructures ranging from coarse (d) to fine (a). The pillar with the highest applied shear strain during the HPT-process ($\gamma \approx 900$) contains only one phase as the high deformation leads to a mixing of the initial materials. The lamellae of the other three pillars are mainly oriented parallel to the loading direction, but a slight inclination can be observed especially for

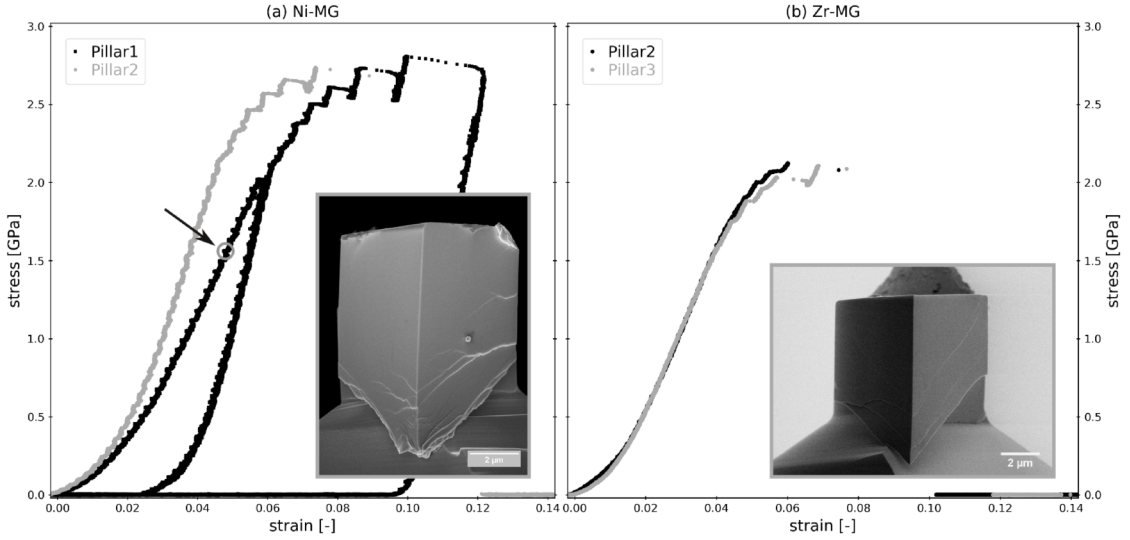

Figure E.3.: Stress-strain curves of single-phased BMGs. (a) Ni-MG shows high strength and ductility in the form of SBs. (b) Zr-MG has a lower strength and ductility. SEM micrographs (inlets) show more branching of the SBs for Ni-MG than for Zr-MG.

$\gamma \approx 60$. All four Zr-MG 40wt% Cu pillars have fine microstructures, but their orientations are different. In (b) the lamellae are oriented parallel to the loading direction while the pillars are prepared in tangential direction. Contrarily in (e), the pillars are prepared in axial direction leading to a lamellae orientation perpendicular to the loading direction. The material with the highest amount of Cu (Zr-MG 60wt% Cu) is shown in c. Both pillars show a very homogeneous lamellar structure, which is inclined with respect to the loading direction. In f the amorphous/amorphous composite Ni-MG 30wt% Zr-MG is depicted. The pillars are prepared from regions with very different applied HPT shear strain, which results in different lamellae spacing. The first pillar has a very coarse microstructure with lamellae thicknesses in the range of micrometers, whereas the second one shows fine lamellae with thicknesses well below 100 nm. The lamellae of both pillars are aligned parallel to loading direction, which is hard to visualize for the second pillar ($\gamma \approx 1200$) due to its fine microstructure.

The different microstructures affect the mechanical properties as shown in the stress-strain curves in Figure E.5. The graphs of the individual materials are arranged as shown in Figure E.4, which enables a one to one comparison of the stress-strain curves to the corresponding microstructure. SBs and therefore the uneven deformation makes it difficult to measure the ductility reasonably. As for the single phase BMGs seen in Figure E.3, step-like stress-strain curves

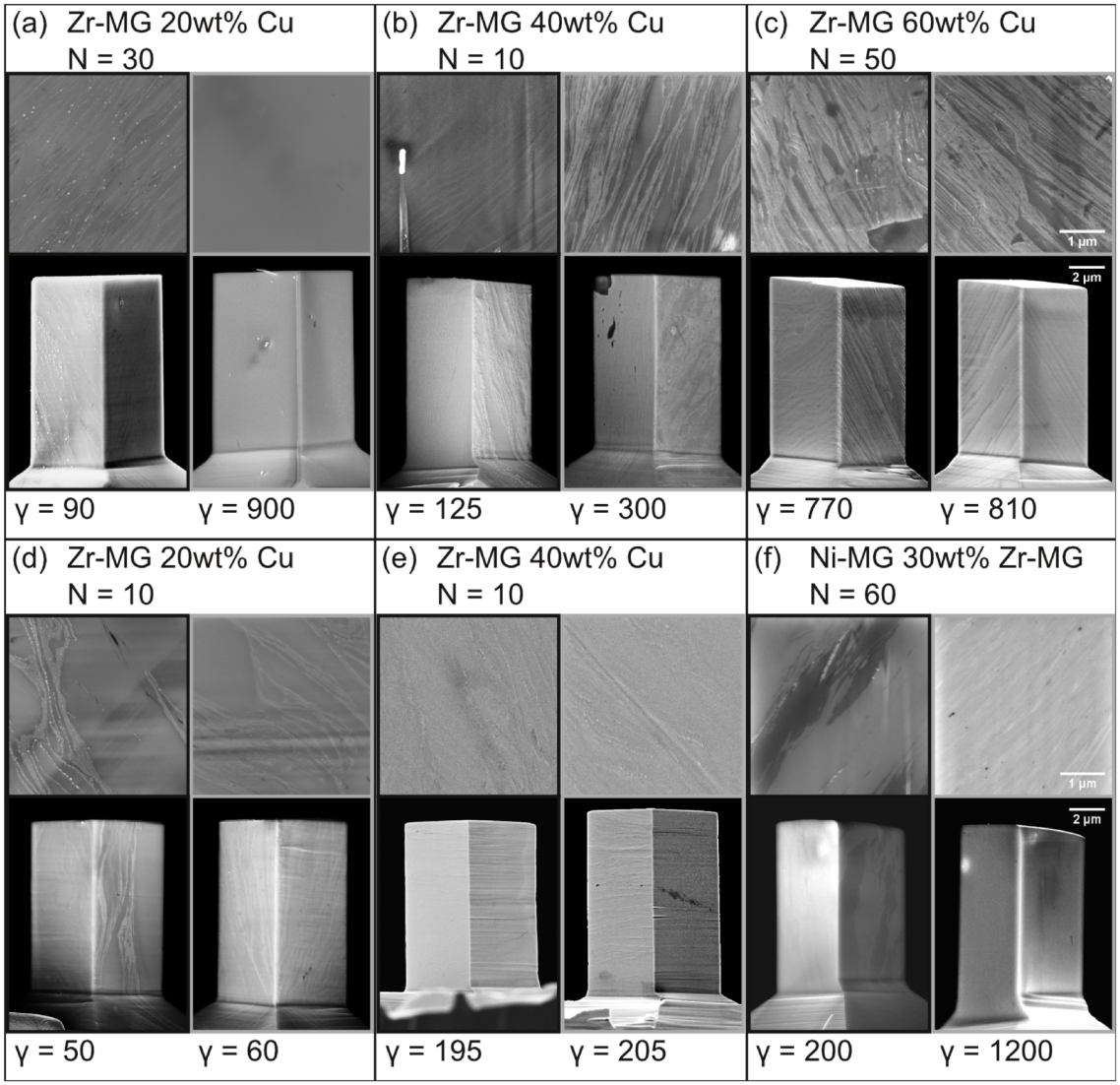

Figure E.4.: SEM micrographs of the top and side view of untested micropillars are shown and the respective composition is indicated. The approximated applied strain during the HPT-process is added and all pillars were prepared in tangential direction, but the ones in (e), which are in axial direction leading to a lamellae orientation perpendicular to the loading direction.

caused by SBs are observed. The formation of a SB does not automatically lead to a failure, because upper part of the pillars is geometrical supported of this set-up. However, such SBs would have caused failure in tensile tests. Therefore, the first strain jump beyond a plastic strain of $\epsilon \approx 0.001$ is declared as failure strain. Moreover, the misalignment caused by tapered pillars impede a correct measurements of plastic strain and these values should be considered with caution. The determined values are nevertheless listed in table 1.

In Figure E.5 a, the differences in the microstructures of the two Zr-MG 20wt% Cu pillars are reflected in the mechanical properties. Mixing of the two phases leads to an increase of strength, but simultaneously to a decrease in ductility. On the other hand, pillars with the same composition but with much coarser microstructure (Figure E.5 d) show lower strength and ductility. Increasing the fraction of Cu from 20 wt% to 40 wt% enhances the ductility (see Figure E.5 b). Similar to (Figure E.5 a), decreasing the lamellae thickness by higher applied shear strain leads also to an increase in strength, but the pillar still show minor ductility as the two phases are not fully mixed yet. This material was also tested in axial direction (Figure E.5 e), but as the microstructure is similar, also ductility and strength are comparable to the results in (Figure E.5 b). The stress-strain curves of Zr-MG 60wt% Cu Cu in (Figure E.5 c) show higher ductility with similar strength compared to Zr-MG 40wt% Cu. The different deformation behavior of the two pillars in (Figure E.5 c) is evident. One deforms with the typical step-like behavior, while the other shows a very smooth plastic deformation. The last composite tested was Ni-MG 30wt% Zr-MG (Figure E.5 f). The strength depends on the amount of applied shear strain during the HPT-process and a finer microstructure leads again to higher strengths. Interestingly, both pillars show a similar ductility.

Nearly all experiments resulted in the formation of at least one fatal SB along which the whole pillar slipped off. The fatal SB is investigated in more detail by the SEM micrographs in Figure E.6. The tested pillars are shown from two sides to give a full image of their failure behavior. It is striking that the orientation of the microstructure is not relevant for most pillars (a, b, e, f). The shear bands are oriented between 45° to 65° to the loading direction and no clear trend caused by the composition, lamellae thickness or orientation is detectable. In some cases more than one SB was activated and in (a) and (e) they are rotate by 90°. If

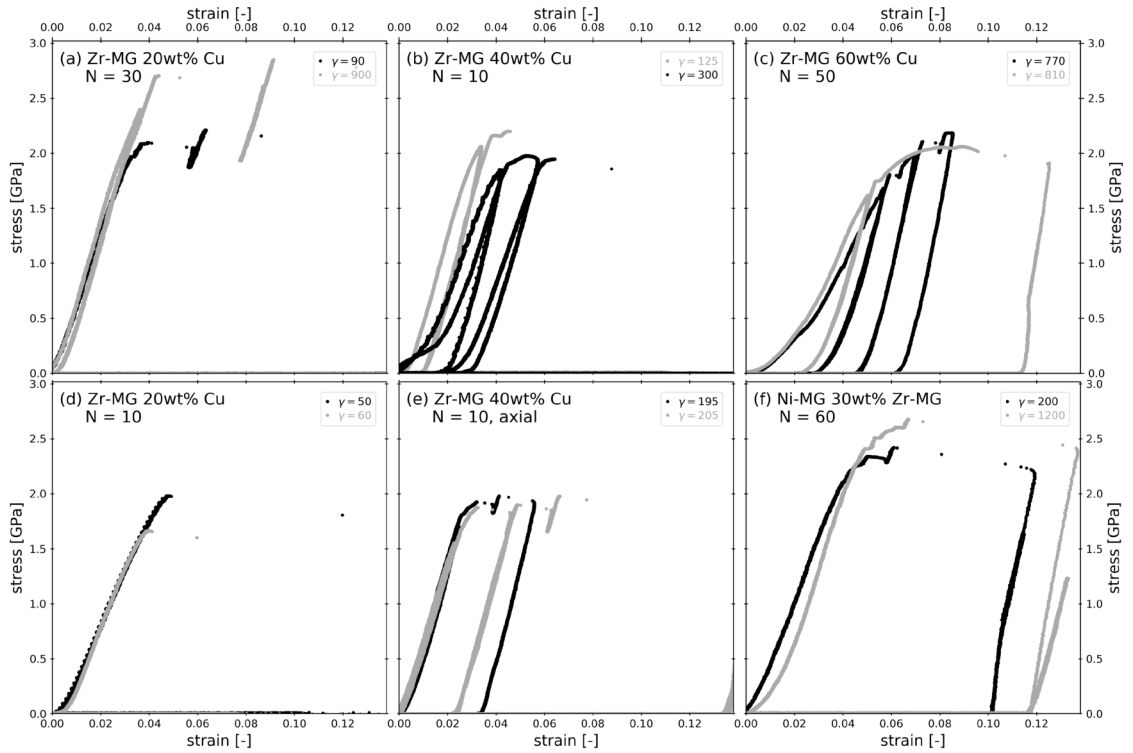

Figure E.5.: Illustration of the selected stress-strain curves of the investigated micropillars. The arrangement of the curves is identical to the arrangement of micrographs in Figure E.4 to ensure same consistent positioning and the curves. The applied strain during the HPT-process are indicated. Some tests were performed in several steps.

Table E.1.: Young's modulus, hardness, activation volume and activation Energy of ZrBe MG subjected to HPT. No distinctive changes due to the applied shear strain is visible and even the variation of the activation volumes remain very small, especially compared to the changes at higher temperature.

		$\gamma[-]$	$\sigma[GPa]$	$\epsilon[-]$
Ni-MG	tangential		2.74	
			2.75	
Zr-MG	tangential		2.13	
			2.04	
Zr-MG 20wt% Cu	tangential	50	1.97	0.005
		60	1.67	0.006
		90	2.1	0.007
		900	2.62	0.003
Zr-MG 20wt% Cu	tangential	125	1.98	0.021
		300	2.2	0.019
	axial	195	1.93	0.01
		205	1.88	0.009
Zr-MG 60wt% Cu	tangential	770	1.8	X
		810	2.06	~ 0.44
Ni-MG 30wt% Zr-MG	tangential	200	2.42	0.017
		1200	2.68	0.018

lamellae are favorable oriented as for Zr-MG 60wt% Cu, $\gamma \approx 770$, and Zr-MG 20wt% Cu, $\gamma \approx 90$, the SBs run along them. This explains the lower strength for Zr-MG 20wt% Cu, $\gamma \approx 60$, seen in Figure E.6 d. The deformation behavior of Zr-MG 60wt% Cu in c is interesting. One pillar shows the formation of a typical SB ($\gamma \approx 770$), but a kink band is formed in the other one ($\gamma \approx 810$). This kink band is expressed in a broad area, which has a lighter color in the micrograph, and in it the lamellar structure is more inclined to the initial lamellae orientation.

However, investigating only the failed pillars does not explain the measured ductility for some pillars. Zr-MG 40wt% Cu shows ductility in the stress-strain curves (Figure E.5 b), but in Figure E.6 b only one dominant shear band with only minor branching is detectable. By looking at the image sequence recorded during testing, small deformations in the Cu lamellae are detectable. For better clarification, selected images are added in Figure E.7 a-d and arrows indicate deformed lamellae. In Figure E.7 c stopping of a SB at a Cu lamellae can be seen. The same SB is reactivated and leads to failure (d). Initially, a similar behavior is also detectable for Zr-MG 60wt% Cu. Figures E.7 7e-g show the evolution of

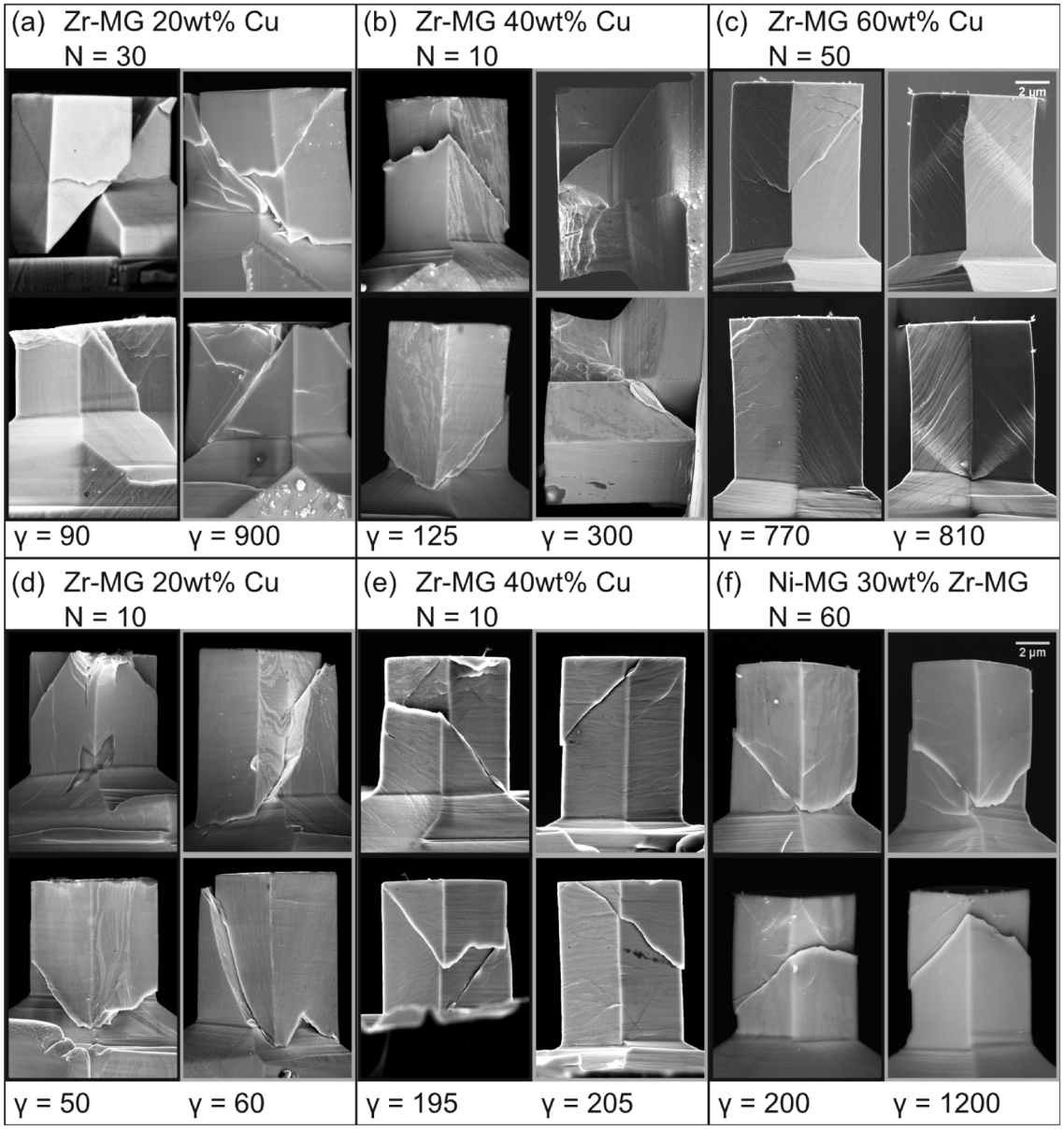

Figure E.6.: SEM micrographs of the tested pillars. Each pillar is shown from both sides. Interestingly, the failure of nearly all pillar proceeds by the formation of a SB, which orientation independent on the microstructure. Only if the orientation is very favorable, the SB runs along it (i.e. d, $\gamma \approx 60$) and in one pillar (c, $\gamma \approx 810$) a kink band is formed.

deformation of Cu lamellae (indicated with arrows), but instead of a fatal SB, a kink band perpendicular to the lamellae is formed.

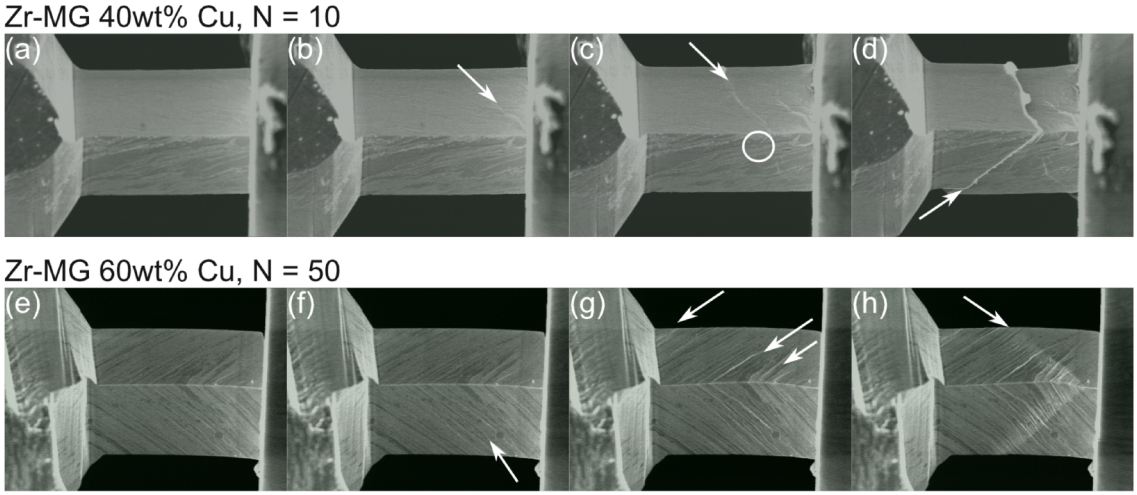

Figure E.7.: SEM micrographs of two different composites, which are recorded during testing. (a and e) show the undeformed pillars and the following micrographs show subsequent deformation steps. The arrows indicate new deformations and the stopping of a SB is marked with a circle in (c). The last two (d and h) are recorded during unloading.

E.4. Discussion

Mechanical properties of BMGCs are investigated by means of micropillar compression testing. Changes in the second phase as its type, thickness and orientation strongly influences the mechanical properties. Zr MG composites with two different materials – crystalline Cu and Ni-MG – as second phase were fabricated. Cu has a much lower hardness compared to the MGs and is known for its ductility, while Ni-MG shows higher strengths and ductility due to SB branching than Zr-MG. Figure E.4 f shows two Ni-MG 30wt% Zr-MG micropillars with different structural sizes. Zr-MG 20wt% Cu micropillars with comparable coarse and fine microstructure can be found in Figures E.4 d and b, respectively. In both cases finer lamellae lead to higher strength. Hardness measurements as a function of the applied strain were conducted in earlier studies [21, 22] showing a more pronounced increase of hardness for Zr-MG + Cu and Zr-MG + Ni-MG at saturation caused by mixing of the two phases and formation of a new amorphous phase. The saturation hardness of first composites are higher than the hardness of Cu and Zr-MG, while the hardness of the latter ones lies between

the hardness of the single-phase MGs. Therefore, the increase in strength can be explained for both cases by mixing of the two phases. Comparing the ductility of Ni-MG 30wt% Zr-MG and Zr-MG 20wt% Cu shows similar values for the coarse microstructures, but the refined Zr-MG 20wt% Cu evinces a nearly brittle behavior, while Ni-MG 30wt% Zr-MG shows no significant difference. For Ni-MG 30wt% Zr-MG, formation and stopping of multiple SBs can be observed, while in the case of Zr-MG 20wt% Cu, the first appeared SB transverse the entire pillar width and leads to failure. Literature indicates a critical thickness value of 20 nm for the amorphous phase to nucleate SBs [Nieh2008], which is not fulfilled in both cases and cannot explain the difference in ductility. Therefore, the propagation of the SBs must be influenced differently. A reasonable explanation is given by the difference in hardness of the two additional phases. The SB will nucleate for both compositions in Zr-MG as its strength is lower than for Ni-MG and even if a SB is formed in Cu, the stress is probably too low to proceed into Zr-MG. Vice versa, a SB nucleated in Zr-MG will not have any difficulties to extend into the Cu and thereby the first one will likely lead to failure. However, the SB will have difficulties to proceed into Ni-MG as its strength is higher and therefore several SBs will be formed which are showing branching and stopping before failure occurs.

Increasing the layer thickness of Cu will influence the ductility [29, 30]. During the HPT-process, co-deformation of the two phases occurs and thereby an individual changing of the thickness of one phase is not possible. Instead the fraction of the two phases are changed and composites with 20, 40, 60wt% of Cu are investigated. Thereby, different microstructure depending on the applied strain during the HPT-process and the compositions are obtained. For Zr-MG 20wt% Cu, microstructures with thick MG and very fine Cu lamellae can be found for low applied strains and by creasing the applied deformation a refinement of the MG lamellae plus a mixing of the two phases occurs. Zr-MG 40wt% Cu Cu shows a more equal thickness of the two phases, but Zr-MG has still broader lamellae. Increasing the Cu-fraction, a more homogenous microstructure is obtained and the thickness of Cu-lamellae exceed the one of the amorphous phase. This increase of the Cu amount and its lamellae thickness affects the deformation in two ways. Firstly, if pillars contain higher amounts of the softer and more ductile Cu, it can undertake more deformation before SBs are formed. And secondly, the propagation of SBs can be hindered. However, different effects must be taken into account for the second point. On one hand decreasing the lamellae thickness of

Cu increases its strength, but the amount of strain and energy it can absorb will decrease. On the other hand, the number of interfaces and transitions between the two phases can also influence the propagation of SBs.
The last main point discussed is the influence of the orientation of the lamellar structure. Lamellae parallel, perpendicular and inclined to the loading direction are investigated. For most cases the fatal SB is independent off the orientation, but interfaces in a favorable direction facilitate its propagation. Figures E.4-E.6 d show two pillars with similar microstructure but for $\gamma \approx 60$, a Cu lamella inclined to the loading direction can be seen. This single inclined interface leads to a decrease in strength as the SB uses the weak interface to run along. The pillars of Zr-MG 60wt% Cu Cu with inclined lamellae (Figures E.4-E.6 c) show the same behavior and several SBs are activated before failure. But while one forms a fatal SB oriented like the lamellae, the other one, which has a nearly interchangeable microstructure, forms a kink band perpendicular to the lamellae. Two things are astonishing about the occurrence of a kink band in this pillar. Firstly, keeping the orientation of the lamellae in mind, a formation of a SB parallel to the lamellar structure looks more presumable and deformation of the Cu in this direction can be seen at the beginning of the test (Figures E.7 e-h). Normally metallic lamellar composites show a formation of a kink band only for a parallel orientation [31] and while layered rocks can form kink bands also for other orientations in geology [32, 33], this occurs only under non-uniaxial stress conditions. However, compression testing of single crystals showed a change of the glide system during testing due to pile-ups of dislocations causing a high back-stress [34]. A similar explanation is possible, when the deformation of the Cu lamellae causes a rotation of the pillar which is constrained by the flat punch indenter leading to stress concentrations at the opposite side. This could lead to the formation of the kink band even though forming of SBs along the lamellae orientation seems more plausible at first glance. Nevertheless, misalignment of the pillar caused by a tapered top surface enhances the multi-axiality of the stress and can explain the difference between the two pillars even though their microstructure and lamellae orientation are very similar.

E.5. Conclusion

Micro compression tests on BMGCs fabricated via HPT revealed a strong influence of the microstructure. Different composites were produced with amorphous/amorphous and amorphous/crystalline phases and for the latter, the fraction were varied from 20 to 60wt% of Cu. Furthermore, the lamellar structure was changed from coarse (1 µm to 2 µm) to fine (<50 nm) by changing the applied strain during the HPT-process. At very high deformations mixing of the phases occurs. The investigation showed three main points:

1. Adding an amorphous or crystalline phase changes the propagation of SBs as hardness and structure are very different. The additional amorphous phase forces a stronger branching of the SBs compared to composites including Cu with a comparable microstructure.
2. Refinement of the lamellar structure of the amorphous/crystalline composites increases their strength and reduces the ductility. This can be explained by mixing of the two phases, which leads to formation of a new harder MG. Reducing the lamellae thickness of the amorphous/amorphous composites increases the strength too, but the ductility is not significantly influenced.
3. Most pillars fail finally by formation of a fatal SB, which is orientated independent to the orientation of the lamellae. Only if lamellae are oriented favorably in relation of the highest shear stress, the SB proceeds along it and thereby reduces the strength as well as the ductility of the pillar. Deformation a priori to the fatal SB is mainly carried out in the Cu phase for amorphous/crystalline composites, whereby a higher fraction of Cu increases the ductility significantly. This plastic deformation can cause a change of the deformation behavior to a kink band by changing the stress distribution in the tested pillar.

E.6. References

[1] J. L. Cheng et al. “Correlation of the microstructure and mechanical properties of Zr-based in-situ bulk metallic glass matrix composites.” In: *Intermetallics* 18.12 (2010), pp. 2425–2430. DOI: 10.1016/j.intermet.2010.08.040 (cit. on p. 142).

[2] C. C. Hays, C. P. Kim, and W. L. Johnson. "Microstructure controlled shear band pattern formation and enhanced plasticity of bulk metallic glasses containing in situ formed ductile phase dendrite dispersions." In: *Physical Review Letters* 84.13 (2000), pp. 2901–2904. DOI: 10.1103/PhysRevLett.84.2901 (cit. on p. 142).

[3] M. Heilmaier. "Deformation behavior of Zr-based metallic glasses." In: *Journal of Materials Processing Technology* 117.3 (2001), pp. 374–380. DOI: 10.1016/S0924-0136(01)00782-8 (cit. on p. 142).

[4] J. C. Qiao and J. M. Pelletier. "Crystallization kinetics in $Cu_{46}Zr_{45}Al_7Y_2$ bulk metallic glass by differential scanning calorimetry (DSC)." In: *Journal of Non-Crystalline Solids* 357.14 (2011). STRUCTURE OF NON-CRYSTALLINE MATERIALS 11 Proceedings of the 11th Conference on the Structure of Non-Crystalline Materials (NCM11) Paris, France June 28- July 2, 2010, pp. 2590–2594. DOI: 10.1016/j.jnoncrysol.2010.12.071 (cit. on p. 142).

[5] Y. Wu et al. "Formation of Cu-Zr-Al bulk metallic glass composites with improved tensile properties." In: *Acta Materialia* 59.8 (2011), pp. 2928–2936. DOI: 10.1016/j.actamat.2011.01.029 (cit. on p. 142).

[6] Y. Wu et al. "Designing Bulk Metallic Glass Composites with Enhanced Formability and Plasticity." In: *Journal of Materials Science & Technology* 30.6 (2014), pp. 566–575. DOI: 10.1016/j.jmst.2014.03.028 (cit. on p. 142).

[7] J. G. Lee et al. "Mechanical property and fracture behavior of strip cast Zr-base BMG alloy containing crystalline phase." In: *Intermetallics* 12.10-11 SPEC. ISS. (2004), pp. 1125–1131. DOI: 10.1016/j.intermet.2004.04.022 (cit. on p. 142).

[8] S. Pauly et al. "Microstructural heterogeneities governing the deformation of Cu47.5Zr47.5Al5 bulk metallic glass composites." In: *Acta Materialia* 57.18 (2009), pp. 5445–5453. DOI: 10.1016/j.actamat.2009.07.042 (cit. on p. 142).

[9] S. T. Deng et al. "Metallic glass fiber-reinforced Zr-based bulk metallic glass." In: *Scripta Materialia* 64.1 (2011), pp. 85–88. DOI: 10.1016/j.scriptamat.2010.09.014 (cit. on p. 142).

[10] H. Shakur Shahabi et al. "Metallic glass–steel composite with improved compressive plasticity." In: *Materials & Design* 59 (2014), pp. 241–245. DOI: 10.1016/j.matdes.2014.03.007 (cit. on p. 142).

[11] R. D. Conner, R. B. Dandliker, and W. L. Johnson. "Mechanical properties of tungsten and steel fiber reinforced Zr41.25Ti13.75Cu12.5Ni10Be22.5 metallic glass matrix composites." In: *Acta Materialia* 46.17 (1998), pp. 6089–6102. DOI: 10.1016/S1359-6454(98)00275-4 (cit. on p. 142).

[12] T. Liu et al. "Synthesis and mechanical properties of TiC-reinforced Cu-based bulk metallic glass composites." In: *Scripta Materialia* 60.2 (2009), pp. 84–87. DOI: 10.1016/j.scriptamat.2008.09.004 (cit. on p. 142).

[13] H. Choi-Yim et al. "Synthesis and characterization of particulate reinforced $Zr_{57}Nb_5Al_{10}Cu_{15.4}Ni_{12.6}$ bulk metallic glass composites." In: *Acta Materialia* 47.8 (1999), pp. 2455–2462. DOI: 10.1016/s1359-6454(99)00103-2 (cit. on p. 142).

[14] Y. Jiang et al. "Modeling of Metallic Glass Matrix Composites Under Compression: Microstructure Effect on Shear Band Evolution." In: *Metallurgical and Materials Transactions A* 49.1 (2017), pp. 417–424. DOI: 10.1007/s11661-017-4412-3 (cit. on p. 142).

[15] J. Eckert et al. "Mechanical properties of bulk metallic glasses and composites." In: *Journal of Materials Research* 22.02 (2007), pp. 285–301. DOI: 10.1557/jmr.2007.0050 (cit. on p. 142).

[16] X. H. Du et al. "New criterion of glass forming ability for bulk metallic glasses." In: *Journal of Applied Physics* 101.8 (2007), p. 086108. DOI: 10.1063/1.2718286 (cit. on p. 142).

[17] A. A. Kündig et al. "Metallic glass/polymer composites by co-processing at similar viscosities." In: *Scripta Materialia* 56.4 (2007), pp. 289–292. DOI: 10.1016/j.scriptamat.2006.10.019 (cit. on p. 142).

[18] X. Sauvage et al. "Structure and properties of a nanoscaled composition modulated metallic glass." In: *Journal of Materials Science* 49.16 (2014), pp. 5640–5645. DOI: 10.1007/s10853-014-8279-z (cit. on p. 142).

[19] J. Qiang and K. Tsuchiya. "Concurrent solid-state amorphization and structural rejuvenation in Zr-Cu-Al alloy by high-pressure torsion." In: *Materials Letters* 204 (2017), pp. 138–140. DOI: 10.1016/j.matlet.2017.06.032 (cit. on p. 142).

[20] Y. F. Sun et al. "Fabrication of ZrAlNiCu bulk metallic glass composites containing pure copper particles by high-pressure torsion." In: *Journal of Alloys and Compounds* 492.1-2 (2010), pp. 149–152. DOI: 10.1016/j.jallcom.2009.11.135 (cit. on p. 142).

[21] L. Krämer, Y. Champion, and R. Pippan. "From powders to bulk metallic glass composites." In: *Scientific Reports* 7.1 (2017). DOI: 10.1038/s41598-017-06424-4 (cit. on pp. 142, 143, 153).

[22] L. Krämer et al. "Bulk metallic dual phase glasses by severe plastic deformation." In: *Intermetallics* 94 (2018), pp. 172–178. DOI: 10.1016/j.intermet.2017.12.005 (cit. on pp. 142, 143, 153).

[23] A. Donohue et al. "Suppression of the shear band instability during plastic flow of nanometer-scale confined metallic glasses." In: *Applied Physics Letters* 91.24 (2007), p. 241905. DOI: 10.1063/1.2821227 (cit. on p. 142).

[24] J.-Y. Kim et al. "Suppression of Catastrophic Failure in Metallic Glass-Polyisoprene Nanolaminate Containing Nanopillars." In: *Advanced Functional Materials* 22.9 (2012), pp. 1972–1980. DOI: 10.1002/adfm.201103050 (cit. on p. 142).

[25] M. C. Liu et al. "Superplastic-like deformation in metallic amorphous/crystalline nanolayered micropillars." In: *Intermetallics* 30 (2012), pp. 30–34. DOI: 10.1016/j.intermet.2012.03.037 (cit. on p. 142).

[26] Y. M. Wang, A. V. Hamza, and T. W. Barbee. "Incipient plasticity in metallic glass modulated nanolaminates." In: *Applied Physics Letters* 91.6 (2007), p. 061924. DOI: 10.1063/1.2768939 (cit. on p. 142).

[27] J. Y. Zhang, G. Liu, and J. Sun. "Crystallization-aided extraordinary plastic deformation in nanolayered crystalline Cu/amorphous Cu-Zr micropillars." In: *Scientific Reports* 3.1 (2013). DOI: 10.1038/srep02324 (cit. on p. 142).

[28] T. G. Nieh and J. Wadsworth. "Bypassing shear band nucleation and ductilization of an amorphous–crystalline nanolaminate in tension." In: *Intermetallics* 16.9 (2008), pp. 1156–1159. DOI: 10.1016/j.intermet.2008.06.018 (cit. on p. 142).

[29] Y. Cui et al. "Plastic Deformation Modes of CuZr/Cu Multilayers." In: *Scientific Reports* 6.1 (2016). DOI: 10.1038/srep23306 (cit. on pp. 142, 154).

[30] W. Guo et al. "Intrinsic and extrinsic size effects in the deformation of amorphous CuZr/nanocrystalline Cu nanolaminates." In: *Acta Materialia* 80 (2014), pp. 94–106. DOI: 10.1016/j.actamat.2014.07.027 (cit. on pp. 142, 154).

[31] M. W. Kapp et al. "Anisotropic deformation characteristics of an ultrafine- and nanolamellar pearlitic steel." In: *Acta Materialia* 106 (2016), pp. 239–248. DOI: 10.1016/j.actamat.2015.12.037 (cit. on pp. 142, 155).

[32] S. Misra, S. Ellis, and N. Mandal. "Fault damage zones in mechanically layered rocks: The effects of planar anisotropy." In: *Journal of Geophysical Research: Solid Earth* 120.8 (2015), pp. 5432–5452. DOI: 10.1002/2014jb011780 (cit. on p. 155).

[33] G. W. Hunt, T. J. Dodwell, and J. Hammond. "On the nucleation and growth of kink and shear bands." In: *Philosophical Transactions of the Royal Society A: Mathematical, Physical and Engineering Sciences* 371.1993 (2013), pp. 20120431–20120431. DOI: 10.1098/rsta.2012.0431 (cit. on p. 155).

[34] D. Kiener, C. Motz, and G. Dehm. "Dislocation-induced crystal rotations in micro-compressed single crystal copper columns." In: *Journal of Materials Science* 43.7 (2008), pp. 2503–2506. DOI: 10.1007/s10853-008-2531-3 (cit. on p. 155).